UNIVERSITY OF CAPE TOWN
IYUNIVESITHI YASEKAPA • UNIVERSITEIT VAN KAAPSTAD

Implementation Of Viscoelastic Hopkinson Bars

Richard Curry

Thesis presented in partial fulfilment of the requirements
of the degree MSc(Engineering)

Blast Impact and Survivability Research Centre
Department of Mechanical Engineering
University of Cape Town
February 2011

Declaration

I hereby grant the University of Cape Town free license to reproduce for the purpose of research either the whole or any portion of the contents in any manner whatsoever of the above dissertation.

I know the meaning of plagiarism and declare that all the work in this document, save for that which is properly acknowledged, is my own. I also declare that this material has not been submitted for any purpose or examination to any other Department or University.

Signed on the 7th of February 2011

.....

Richard Curry

Abstract

The properties of soft, viscoelastic materials at high strain rates are important in furthering our understanding of their role during blast or impact events. When wanting to test these soft or low impedance materials using a split Hopkinson pressure bar setup one experiences poor signal to noise ratios and impedance mismatching when using metallic bars. One way of overcoming these difficulties is to use polymeric Hopkinson bars [1]. Implementing polymeric Hopkinson bars requires characterisation of the viscoelastic properties of the material used. In this dissertation, Polycarbonate, Polymethyl Methacrylate and Nylon are considered for use as Hopkinson bars. Conventional Hopkinson bar analysis cannot be used on the polymeric bars due to the viscoelastic nature of the bar material. As stress waves propagate along the length of the bars, viscoelastic effects result in dispersion and attenuation. The main topic of this dissertation is to account for this viscoelastic material effect. This is achieved by characterising the viscoelastic behaviour of the material, allowing for the bars effect on a stress wave to be accounted for. The different methods for characterisation of the viscoelastic properties of each bar are explored in the literature and ultimately characterised using Bacons' method [2]. All three bar materials are successfully calibrated and a magnesium bar is used to verify a force balance at the bar ends indicating the correct implementation. Finally the three bar materials can be compared and an appropriate choice of bar material is made for the application of testing low impedance materials.

Acknowledgements

It is a pleasure to recognize those who made this thesis possible.

First and foremost I would like to thank my supervisor, Trevor Cloete, for his support, advice and encouragement. The leap into the project was worth every moment.

My sincere thanks go to Professor Gerald Nurick for his help in organising funding, for his advice, and for creating such a unique work environment.

Mr Reuben Govender for his unique insights into Fourier analysis and the realms of the frequency domain, without your help I may still be lost there. The effort you put in was always above and beyond what was expected.

Mr Ernesto Ismail, for your help in vibration principles and being an ear to bend when I needed it.

My thanks go to the Mechanical Engineering workshop staff especially Glen Newins, Charles Nicholas, Horst Emrich and Len Watkins for having the patience to manufacture the polymer bars and strikers.

Finally to my office mates and friends who always made time for a laugh and a cup of coffee, without your support I would never have made it.

Contents

Declaration **I**

Abstract **I**

Acknowledgements **IV**

Nomenclature **XVII**

1 Introduction **1**

2 Literature Review **3**

2.1 The Hopkinson Bar . . . 3

2.1.1 Hopkinson Bar Theory . . . 4

2.2 Fourier and the FFT . . . 12

2.2.1 Fourier transform . . . 12

2.2.2 The Discrete Fourier Transform (DFT) . . . 13

2.2.3 The Fast Fourier Transform (FFT) . . . 15

2.3 Characterising A Viscoelastic Material . . . 17

2.4 Viscoelastic Wave Propagation . . . 18

2.4.1 Blanc . . . 19

2.4.2 Wang *et al* . . . 21

2.4.3 Zhao and Gary . . . 22

2.4.4 Bacon . . . 25

2.4.5 Salisbury . . . 27

2.4.6 Liu and Subhash . . . 27

2.5 Polymeric Hopkinson Bars . . . 28

2.5.1 NYLON Bars . . . 28

2.5.2 Polycarbonate Bars . . . 29

2.5.3 Polymethyl Methacrylate Bars . . . 32

3 Polymeric Material Response 37

3.1 Determination ofViscoelastic Properties . . . 38
3.1.1 The Maxwell Model . . . 39
3.1.2 Kelvin-Voigt model . . . 39
3.1.3 Standard Linear Solid model . . . 40
3.1.4 Shim model . . . 41
3.2 Quasistatic Material Tests . . . 43
3.3 Implementation . . . 45

4 Experimental Methodology 49

4.1 Strain Gauging and Data Capture . . . 49
4.2 Tap tests . . . 51
4.3 Experimental Bar Layout . . . 55
4.4 Calibration tests . . . 57
4.4.1 Wave speed calibration . . . 57
4.4.2 Gauge station calibration . . . 59

5 Data Processing 67

5.1 Theory . . . 67
5.2 Deriving the Propagation coefficient . . . 69
5.2.1 Magnitude . . . 73
5.2.2 Attenuation Co-efficient . . . 74
5.2.3 Phase angle . . . 75
5.2.4 Wave number . . . 77
5.2.5 Phase velocity . . . 77
5.2.6 Propagation coefficient . . . 78
5.3 Shifting pulses in polymer bars . . . 79

6 Results 81

6.1 Configuration 1 - Polymer bars . . . 82
6.1.1 NYLON . . . 82
6.1.2 PMMA . . . 85
6.1.3 PC single gauge station . . . 88
6.1.4 PC double gauge station . . . 92

6.2 Calibration factors for polymer gauge stations 94
6.3 Configuration 2 - Polymer -> Magnesium 95
6.4 Configuration 3 - Magnesium ->Polymer 97

7 Discussion **101**

8 Conclusions and Recommendations **105**

Bibliography **107**

Appendices

A Strain gauge amp design

B MATLAB code for SHIM model

C MATLAB code for deriving a propagation co-efficient

D MATLAB code for shifting signals

List of Figures

2.1 The Split Hopkinson Pressure Bar (SHPB) setup [3] 4
2.2 Impact between dissimilar bars 6
2.3 High speed images of a RTV630 rubber specimen deforming 10
2.4 The Phase velocity solution to six Pochammer Chree modes 11
2.5 The complex plane 13
2.6 A typical amplitude spectrum from a Fourier transform 15
2.7 The behaviour of a Maxwell model [4]. 18
2.8 Behaviour of a Kelvin-Voigt model [4]. 18
2.9 The experimental setup used by Blanc [5] 20
2.10 Schematic showing the spring dashpot representation of equation 2.27 . . 21
2.11 Rheological model using the spring dashpot representation 22
2.12 A comparison between the 1D and 3D viscoelastic assumptions 23
2.13 Phase velocity and attenuation co-efficients of Zhao and Gary 3D approach 23
2.14 A rheological model for PMMA [6] 24
2.15 Comparison of the input and output forces of the bar end 24
2.16 Phase velocity and attenuation co-efficient for experimental results 26
2.17 Comparison of Liu's multi gauge station setup 28
2.18 The modified Split Hopkinson Bar setup by Shim [7] using NYLON bars. 29
2.19 The Split Hopkinson Pressure Bar setup used by Shim [8] using PC bars. 30
2.20 Wave form at the two gauge stations reported by Shim 30
2.21 Modified Hopkinson pressure bar used by Martin 31
2.22 Rheological model used by Yunoshev 31
2.23 Schematic of Sawas experimental setup [9]. 32
2.24 Stress Strain data for styrofoam obtained by Sawas [9]. 33
2.25 High speed images from tests performed on foams 34
2.26 Typical fracture of polymeric foam seen by Subhash 35

2.27 The two SHPB systems used by Subhash 35

3.1 The Maxwell model 39
3.2 The Kelvin-Voigt model 40
3.3 The Standard Linear Solid model 40
3.4 The Shim model 41
3.5 Quasistatic testing of PC 44
3.6 Quasistatic testing of NYLON 44
3.7 Quasistatic testing of PMMA 45
3.8 Shim model replicating PMMA behaviour. 46
3.9 Shim model replicating PC behaviour. 47
3.10 Shim model replicating NYLON behaviour. 47

4.1 The schematic of the strain gauge stations [10] 50
4.2 A typical Polymeric Hopkinson bar signal from a gauge station 52
4.3 The tap tests on the three materials 54
4.4 The different experimental configurations 55
4.5 Wave speed calibration on the magnesium bar 58
4.6 The shifted incident and reflected pulses coinciding 59
4.7 Attempted wave speed calculation of nylon using conventional approach . 60
4.8 The gauge station layout on the PC bar 64
4.9 The raw data from the double gauge stations on the PC bar 65
4.10 Quasistatic calibration of PC bar gauge stations 66
4.11 The corrected data from the double gauge stations on the PC bar 66

5.1 Flow chart of deriving the propagation coefficient 70
5.2 The raw signal output from PC bar impacted with 400 mm PC striker . 72
5.3 The raw signal output from PC bar impacted with 400 mm PC striker . 73
5.4 The modulus in the frequency domain 74
5.5 The attenuation coefficient for PC in the frequency domain. 75
5.6 The phase angle in the frequency domain 76
5.7 The Unwrapped phase angle 76
5.8 The wavenumber for PC in the frequency domain. 77
5.9 The phase velocity for PC in the frequency domain. 78
5.10 The incident and reflected pulses shifted back to the free interface. 80

6.1 A cloud of data showing the spread in Attenuation coefficient for NYLON. 82
6.2 A cloud of data showing the spread in Wave number for NYLON. 83
6.3 A cloud of data showing the spread in Phase velocity for NYLON. 84
6.4 A shifted NYLON signal 85
6.5 A cloud of data showing the spread in Attenuation coefficient for PMMA. 86
6.6 A cloud of data showing the spread in Wave number for PMMA. 87
6.7 A cloud of data showing the spread in Phase velocity for PMMA. 87
6.8 A shifted PMMA signal 88
6.9 cloud of data for Attenuation coefficient with PC single gauge 89
6.10 A cloud of data showing the spread in Wave number for PC single gauge. 89
6.11 A cloud of data showing the spread in Phase velocity for PC single gauge. 90
6.12 A shifted PC signal 91
6.13 The appearance of Pochammer Chree oscillations on the PC bar. 91
6.14 Cloud of data for Attenuation coefficient with PC double gauge 93
6.15 A cloud of data showing the spread in Wave number for PC double gauge. 93
6.16 A cloud of data showing the spread in Phase velocity for PC double gauge. 94
6.17 The forces at the bar interface between NYLON and magnesium. 96
6.18 The forces at the bar interface between PMMA and magnesium. 96
6.19 The forces at the bar interface between PC and magnesium. 97
6.20 The forces at the bar interface between magnesium and NYLON. 98
6.21 The forces at the bar interface between magnesium and PMMA. 98
6.22 The forces at the bar interface between magnesium and PC. 99

List of Tables

3.1 The results of the quasistatic compression tests. 43

4.1 The properties of the Hopkinson bars used 50
4.2 The different strikers used during the tests 55
4.3 Test Matrix for Configuration 1. 56
4.4 Test matrix for Configuration 2. 56
4.5 Test matrix for Configuration 3 56
4.6 The clibration results for the magnesium bar gauge station 63
4.7 Uncorrected calibration results for the gauge stations 63

6.1 The calibration factors for the strain gauges using the corrected waves. . 95

Nomenclature

Roman

A	Cross-sectional area
C	Wave propagation speed
E	Young's modulus
F	Force
k	Wave number
L	Length
m	Mass
r	Modulus
T	Temperature
t	Time
u	Displacement
v	Velocity

Greek

α	Attenuation coefficient
$\dot{\epsilon}$	Equivalent strain rate
$\dot{\sigma}$	Equivalent stress rate

ϵ Equivalent strain

η Damping coefficient

γ Propagation coefficient

ω Frequency

ρ Density

σ Equivalent stress

Θ Phase angle

Subscripts

i incident

$melt$ melting

r reflected

s specimen

t transmitted

$trans$ transition

Abbreviations

BISRU Blast Impact and Survivability Research Unit

CFT Continuous Fourier transform

DFT Discrete Fourier transform

FFT Fast Fourier transform

IFFT Inverse Fast Fourier transform

PC Polycarbonate

PMMA Polymethyl Methacrylate

SHPB Split Hopkinson Pressure Bar

Chapter 1

Introduction

Material characterisation at high strain rates is concerned with measuring the change in mechanical properties, such as yield strength, work hardening, and ductility, which can deviate from quasi-static results at higher strain rates. Strain rate, $\dot{\varepsilon}$, is defined as the rate of change of strain with respect to time, t. The changes in these properties at high strain rates has become more important as improvments have been made to high speed machining operations, ballistic and impact events where the changes in these properties can have adverse effects. Dynamic material characterisation forms the corner stone in developing accurate computational models. Without these material properties it would not be possible to use computational models to perform analyses such as simulated car crashes, dynamic structural loadings and defence applications.

Mechanical properties are normally determined by performing standard loading tests such as compression, tension, or torsion [11] [12]. Conventional testing can be used to achieve nominally constant loading rates for limited plastic strains and thereby a constant engineering strain rate. Quasi-static and low range dynamic tests are often performed on servo hydraulic or screw driven machines used to measure the stress-strain response of materials up to strain rates as high as $\mathbf{1}s^{-1}$. There are also purpose built machines that can achieve strain rates as high as $\mathbf{200}s^{-1}$. Typically if higher strain rates are desired impact driven stress wave propagation is used to load specimens.

The main technique in the range of $\mathbf{500}s^{-1} - \mathbf{5 \times 10^3}$ is the Split-Hopkinson Pressure Bar (SHPB), which is capable of achieving high uniform uni-axial stress loading of a specimen in compression at nominally constant strain rates of the order of $\mathbf{10^3}s^{-1}$. Hopkinson bar techniques have also been developed to probe the high-rate response of materials in tensile and torsion-loading stress states. In each instance, specimen stress

is inferred using elastic elements in series with the specimen of interest. Stress waves are generated via an impact event, and the elastic elements used are long bars such that the duration of the loading pulse is less than the wave transit time in the bar. In each of the Hopkinson bar techniques, the dynamic stress-strain response of materials at strain rates up to $\mathbf{5 \times 10^3 s^{-1}}$ in compression, and somewhat lower in tension or torsion, and true strains of 0.3 can be readily achieved in a single test.

The most widely used techniques normally implement metallic Hopkinson bars, can have a material impedance in the region of 40 MPa s/m . These metallic bars experience difficulties when testing materials which have a significantly lower impedance then the bar being used to test them, meaning that testing of soft materials with an impedance of 2 MPa s/m is not possible. One solution to over coming this problem has been to simply use a bar material which has an impedance closer to that of the material being tested. As a result polymers have been used as Hopkinson bars as they have an impedance in the region of 4 MPa s/m.

This dissertation deals with the implementation of polymeric Hopkinson bars which will enable testing of soft materials on a Split Hopkinson Pressure Bar setup.

Chapter 2

Literature Review

The purpose of this chapter is to explore work presented in the published literature dealing with the implementation of the Split Hopkinson Pressure Bar technique (SHPB) using viscoelastic materials and other experimental uses of different viscoelastic bars. To start with, the foundation work and principals of the Hopkinson bar are presented. Thereafter the use of Fourier transforms and the different methods proposed by authors for dealing with the viscoelastic properties of the polymer bars is explored. Finally the different published uses and configurations of the polymer bars are discussed.

2.1 The Hopkinson Bar

The split-Hopkinson pressure bar technique is named after Bertram Hopkinson [13] who, in 1914 used induced-wave propagation in a long elastic metallic bar to measure the pressures produced during blast and impact events. Based on this pioneering work, the experimental technique of using elastic stress-wave propagation in long rods to study dynamic material properties has come to be named the Hopkinson pressure bar. Later work by Davies [14, 15] and Kolsky [16] used two Hopkinson pressure bars in series, with the sample sandwiched in between, to measure the dynamic stress-strain response of materials. This technique thereafter has been referred to as either the Split Hopkinson pressure bar or Kolsky bar. As shown in Figure 2.1, tests are conducted by inducing a stress wave $\boldsymbol{\sigma_i}$ in the incident bar which propagates past strain gauge station 1 where it is measured, down the length of the bar to the interface at the end where the specimen is located. When the stress wave reaches the interface, a portion of the stress wave is transferred through to the specimen. The remainder is reflected back in the opposite

direction, called the reflected stress wave σ_r, which is again measured by gauge station 1. By comparing these two strain signals (σ_i and σ_r) from gauge station 1 it is possible to determine what the stress load applied to the one side of the specimen was together with the displacement of the face.

The stress wave transferred to the specimen propagates through the specimen and reaches the interface of the transmitter bar. As the stress wave reaches the transmitter bar, a portion of the stress wave will be transferred to the transmitter bar, called the transmitted stress σ_t, and the remainder will reflect off the interface. The transmitted stress then propagates down the length of the bar to gauge station 2 where it is detected. By knowing what stress went into the specimen and knowing what comes out, the response of the specimen can be evaluated.

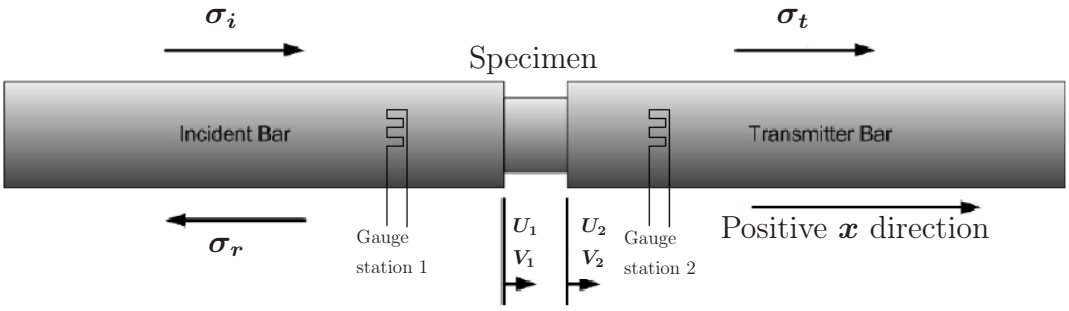

Figure 2.1: The Split Hopkinson Pressure Bar (SHPB) setup [3]

2.1.1 Hopkinson Bar Theory

One Dimentional Wave theory

A thorough description of the SHPB and the background theory is provided by Gray [1] and therefore will not be repeated here. However, the salient points will be highlighted.

The geometry of Hopkinson bars allows 1D wave theory to be used, from elementary wave theory the wave equation can be shown to be

$$\frac{\partial^2 u}{\partial x^2} = \frac{1}{C_0^2}\frac{\partial^2 u}{\partial t^2} \tag{2.1}$$

where $C_0 = \sqrt{\frac{E}{\rho}}$ is the fundamental wave velocity, u is the displacement and t is the time. The general solution to the wave equation can be written as

$$u = f(x - C_0 t) + g(x - C_0 t) = u_i + u_r \tag{2.2}$$

where f and g give the form of the wave traveling in the positive and negative direction respectively.

By definition the 1D strain is given by

$$\varepsilon = \frac{\partial u}{\partial x} \tag{2.3}$$

Thus Equation 2.2 can be written as

$$\varepsilon = f\prime + g\prime = \varepsilon_i + \varepsilon_r \tag{2.4}$$

Finally, differentiating Equation 2.1 with respect to time and using Equation 2.4 the velocity of the incident bar can be written as

$$\dot{u_1} = C_0(-f\prime + g\prime) = C_0(-\varepsilon_i + \varepsilon_r) \tag{2.5}$$

and for the transmitter bar

$$\dot{u_2} = -C_0 \varepsilon_t \tag{2.6}$$

Equations 2.5 and 2.6 are valid at all points of the bars including the bar ends or specimen interfaces which are going to be the points of interest. If the instantaneous length of the specimen L_s is know then the strain rate in the specimen can be calculated from

$$\dot{\varepsilon} = \frac{(\dot{u_1} - \dot{u_2})}{L_s} \tag{2.7}$$

combining equations 2.5, 2.6 and 2.7 it is possible to write the more practical form

$$\dot{\varepsilon} = \frac{C_0}{L_s}(-\varepsilon_i + \varepsilon_r + \varepsilon_t) \tag{2.8}$$

Finally using the bar area A and the Young's modulus E the forces on the bar ends can be written as

$$\begin{aligned} F_1 &= A_1 E_1(\varepsilon_i + \varepsilon_r) \\ F_2 &= A_2 E_2(\varepsilon_t) \end{aligned} \tag{2.9}$$

After an initial "ring up"[1] period the specimen is in equilibrium and is regarded as deforming uniformly. In which case the forces on the two faces should be in equilibrium

[1]The term ring up is described in more detain in the section dealing with specimen equilibrium.

$F_1 = F_2$. From the forces on the bar ends it is possible to infer stress levels in the specimen with

$$\sigma_s = \frac{F_1 + F_2}{2A_s} \tag{2.10}$$

where A_s is the area of the specimen.

Impact of Dissimilar Bars

In the preceding explanations, the assumption has been made that the material properties and geometry of both the input and transmitter bars have been the same. To illustrate the differences that arise, a more general case of the impact of two bars of different material and geometry, adapted from Spotts [17], is presented.

The layout of the two bars can be seen in Figure 2.2. The areas and densities of the two bars are A_1, A_2 and ρ_1, ρ_2 respectively.

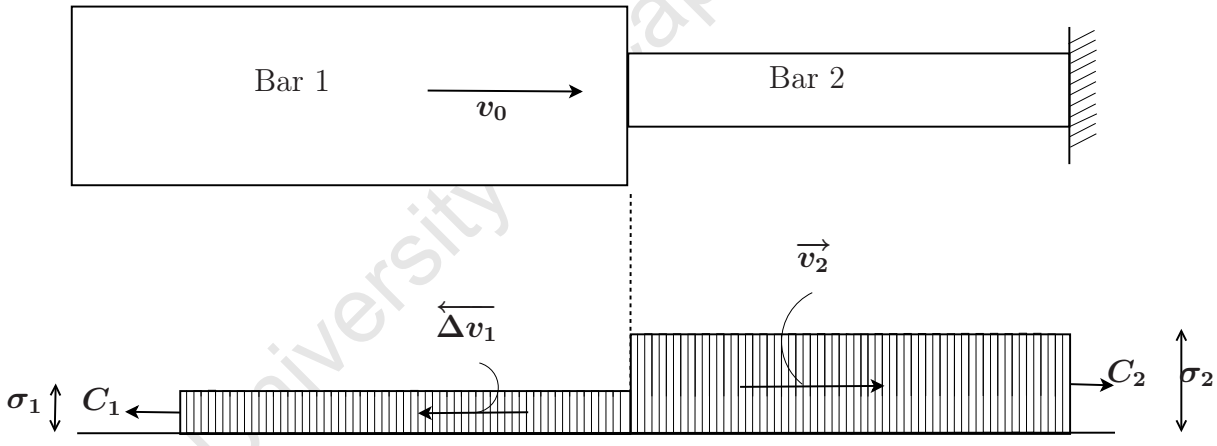

Figure 2.2: Impact between dissimilar bars

In the generic case, applying the impulse momentum equation to the compressed region seen in Figure 2.2 yields

$$\sigma_2 = C\rho\overrightarrow{v_2} \tag{2.11}$$

Where C is the wave speed and $\overrightarrow{v_2}$ is the particle velocity in Bar 2 travelling to the right.

Applying a force balance across the interface of the bars yields

$$\sigma_1 A_1 = \sigma_2 A_2 \tag{2.12}$$

which can written as :

$$\begin{aligned} \rho_1 C_1 \Delta \overleftarrow{v_1} A_1 &= \rho_2 C_2 \overrightarrow{v_2} A_2 \\ \therefore \overrightarrow{v_2} &= \Delta \overleftarrow{v_1} \frac{\rho_1 C_1 A_1}{\rho_2 C_2 A_2} \end{aligned} \tag{2.13}$$

The velocity $\Delta \overleftarrow{v_1}$ of the compressive wave moving to the left is sufficient to reduce the initial particle velocity $\overrightarrow{v_0}$ of Bar 1 to the velocity $\overrightarrow{v_2}$ of the interface. Resulting in the following

$$\begin{aligned} \overrightarrow{v_0} - \overleftarrow{\Delta v_1} &= \overrightarrow{v_2} \\ &\textit{or} \\ v_0 &= v_1 + v_2 \\ &= v_1 + v_1 \frac{\rho_1 C_1 A_1}{\rho_2 C_2 A_2} \\ &= v_1 \left(1 + \frac{\rho_1 C_1 A_1}{\rho_2 C_2 A_2} \right) \end{aligned} \tag{2.14}$$

rearranging for v_1 yields

$$\begin{aligned} v_1 &= v_0 \left(\frac{1}{1 + \frac{\rho_1 C_1 A_1}{\rho_2 C_2 A_2}} \right) \\ &= v_0 \left(\frac{\rho_2 C_2 A_2}{\rho_1 C_1 A_1 + \rho_2 C_2 A_2} \right) \end{aligned} \tag{2.15}$$

Bar 2 velocity can now be found using $v_2 = v_0 - v_1$ and substituting in Equation 2.15

$$\begin{aligned} v_2 &= v_0 - v_0 \left(\frac{\rho_2 C_2 A_2}{\rho_1 C_1 A_1 + \rho_2 C_2 A_2} \right) \\ &= v_0 \left(1 - \frac{\rho_2 C_2 A_2}{\rho_1 C_1 A_1 + \rho_2 C_2 A_2} \right) \\ &= v_0 \left(\frac{\rho_1 C_1 A_1}{\rho_1 C_1 A_1 + \rho_2 C_2 A_2} \right) \\ &= v_0 \left(\frac{\frac{\rho_1 C_1 A_1}{\rho_2 C_2 A_2}}{1 + \frac{\rho_1 C_1 A_1}{\rho_2 C_2 A_2}} \right) \end{aligned} \tag{2.16}$$

The stress in Bar 1 can now be calculated using equation 2.11 and Equation 2.15 while the stress in Bar 2 can be calculated using Equations 2.11 and 2.16

$$\begin{aligned} \sigma_1 &= \frac{v_0 C_1 \rho_1}{1 + \left(\frac{A_1 C_1 \rho_1}{A_2 C_2 \rho_2} \right)} \\ \sigma_2 &= \frac{v_0 C_2 \rho_2}{1 + \left(\frac{A_2 C_2 \rho_2}{A_1 C_1 \rho_1} \right)} \end{aligned} \tag{2.17}$$

When this result is interrogated some interesting relations become apparent. One term relates the material properties of both bars, namely

$$\left(\frac{A_1 C_1 \rho_1}{A_2 C_2 \rho_2}\right)$$

which can be further deconstructed into

- area ratio $\frac{A_1}{A_2}$
- impedance ratio $\frac{C_1 \rho_1}{C_2 \rho_2}$.

By simply inspecting these terms it becomes possible to gain insight into the expected response of any two bars used in a Split Hopkinson bar setup.

When discussing the impedance it can be defined in two ways namely the acoustic material impedance ρC and the bar impedance $\rho C A$.

The bars are often made of a high strength steel with a high elastic limit $\sigma_s > 1GPa$ and an acoustic material impedance of $\rho_0 C_0$ of approximately 40 MPa s/m. This is done as the specimen of test material must have a lower strength and lower acoustic wave impedance $\rho_s C_s$, allowing it to deform plastically while the bars are still in the elastic state. However if the wave impedance of the specimen $\rho_s C_s A_s$ is much lower than that of the bars, the signal of the transmitted pulse will become too small so that it is unable to be detected accurately. In such a case it makes more sense that a bar material with a lower acoustic impedance, such as polymers, should be used instead of high strength steel. This ultimately results in a lower impedance mismatch between the specimen and the bars meaning that a larger stress wave is transmitted to the output bar.

Hopkinson bars with an impedance of 10MPa s/m have been used by Wang *et al* [18] in the testing of solid polymers with reported success. However testing of materials with an impedance in the region of 0.1 MPa s/m would prove difficult.

Chen [19] attempted to overcome this problem when testing low impedance materials. Chen implemented a hollow aluminium output tube in place of conventional solid Hopkinson bars and instrumented a solid input bar with quartz crystals which are significantly more sensitive then conventional strain gauges which are normally used. Chen *et al* [20] later used this method on soft rubber specimens reporting good results.

Specimen equlibrium

Assuming that a transmitted signal with high signal-to-noise ratio is obtained and accurately describes the conditions at the specimen interface, dynamic equlibrium of stress in specimen presents another major obstacle in obtaining reliable stress-strain data from a conventional SHPB experiment. Equations 2.1 and 2.2 are based on the assumption of dynamic stress equilibrium in the specimen allowing the use of wave superposition, which is not satisfied automatically when the specimen material has a very low material impedance. Dynamic stress equilibrium can be achieved quickly in a metallic or ceramic specimen due to relatively high wave speeds in those specimens. However, the stress state in a soft specimen may not be in equilibrium over the entire loading duration in a SHPB experiment as the wave speeds in such materials are often slow. In a SHPB experiment, it takes several stress wave reflections within the specimen for stress wave to "ring up" to a state of dynamic stress quasi equilibrium. The non-equilibrated stresses in specimen during a SHPB experiment may lead to a drastic non-uniform deformation in specimen, which invalidates the experimental results for material property characterization [21].

Song and Chen [22] provide a well motivated argument on this subject showing high speed camera footage of soft materials such as rubber and foams being tested. One such example is shown in Figure 2.3 where a rubber specimen can be seen very clearly deforming from one side as the stress wave propagates through the specimen. The drastic non-uniform deformation in specimen demonstrates that the conventional SHPB experiment may not produce valid dynamic properties of the rubber material.

Dispersion Correction in Metallic Bars

One dimensional wave theory is per definition limited by the assumption that there is no disturbance other than in the direction of wave propagation and that the wave does not change shape in the direction of propagation due to axial or radial dispersion. 3D effects are important as pointed out by Pochammer [23] and Chree [24] who independently arrived at the same solution for the equation governing transmission of waves along an infinite bar. This result showed that the propagation velocity or phase velocity $\boldsymbol{C_p}$ of a disturbance consisting of a single continuous sinusoidal wave is not just a function of the material as assumed by one dimensional theory, but is also a function of the wave length $\boldsymbol{\lambda}$, or frequency $\boldsymbol{\omega}$. In addition, different modes of vibration may be excited by the same frequency and propagate at different phase velocities.

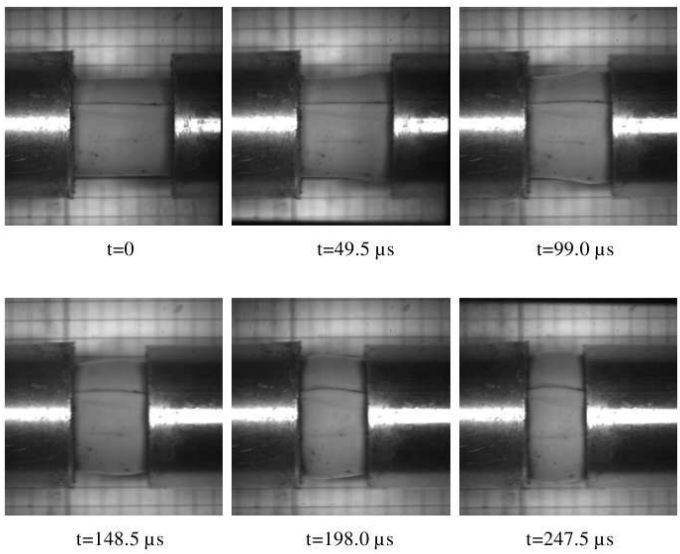

Figure 2.3: High speed images of a RTV630 rubber specimen deforming dynamically [22].

The form of the displacement solution is

$$\begin{aligned} U_z &= U(r)e^{i(\gamma z+pt)} \\ U_r &= W(r)e^{i(\gamma z+pt)} \end{aligned} \tag{2.18}$$

where $U(r)$ and $W(r)$ are time invariant functions which describe the variation in axial or radial displacement respectively as a function of radius.

Bancroft [25] and Davies [14] presented numerical solutions to the Pochammer-Chree equations. These showed a relationship between frequency ω and phase velocity C_p, and the variation of axial displacement across the radius of the bar. Davies showed the change in shape of a pulse as it propagates axially (dispersion) by representing a trapezoidal pulse with its Fourier series and phase shifting each term according to the phase velocity. As the deflection can be related to the stress in the bar, it was possible to obtain the stress history of a pulse in the bar. Davies also noted that the energy of a pulse consisting of different wavelengths will be transmitted at a different velocity to the phase velocity of the individual wavelengths. This velocity is termed the "group velocity" C_g and is characterised by the following equation as explained by Govender [26].

$$C_g = C_p - \lambda \frac{\partial C_p}{\partial \lambda}$$

Gorham [27], Follansbee and Frantz [28] present methods for the dispersion correction of arbitrary pulses in metal bars. Gorham's method requires transforming the captured strain signal in the time domain $\varepsilon(t)$, into the frequency components $\varepsilon(\omega)$ by means of the Fourier integral [29] presented in Equation 2.19 . An important link is that the origional work by Pochammer and Chree used a continuous sinusoidal wave, while Fourier allows a complex wave to be written as a sum of sinusoids. A full discussion of Fourier is conducted in Section 2.2.1.

$$f(t) \Leftrightarrow F(\omega) = \int_{-\infty}^{\infty} f(t) e^{i\omega t} dt \tag{2.19}$$

Dispersion may be described by the various frequency components of the pulse changing their relative phase. This is easily explained by looking at Figure 2.4 which relates the phase velocity C_p to the frequency ω.

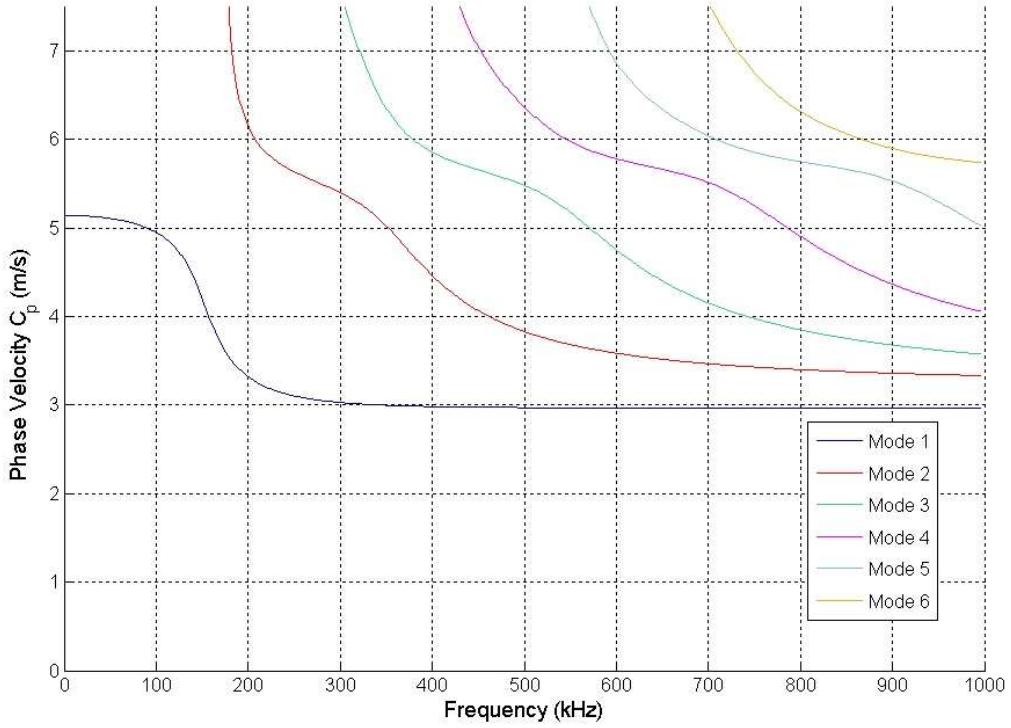

Figure 2.4: The Phase velocity solution to six Pochammer Chree modes by Govender [26]

2.2 Fourier and the FFT

Fourier analysis forms an integral part of Hopkinson bar dispersion analysis, however presenting a detailed introduction to Fourier analysis is beyond the scope of this dissertation. Instead the most salient points relevant to the techniques implemented here are presented. For a thorough explanation the reader is referred to Norman Morrison's book "An Introduction to Fourier Analysis" [29].

2.2.1 Fourier transform

Fourier analysis is primarily concerned with representing and analysing periodic phenomena, via Fourier series. Through the Fourier transform these insights can be extended to nonperiodic phenomena. In fact, one way of getting from Fourier series to the Fourier transform is to consider nonperiodic phenomena as a limiting case of periodic phenomena as the period tends to infinity. A discrete set of frequencies in the periodic case becomes a continuum of frequencies in the nonperiodic case, leading to the idea of a spectrum.

The Fourier transform of a function $\boldsymbol{f(t)}$ can be defined to be

$$\widetilde{\boldsymbol{F}}(\boldsymbol{s}) = \int_{-\infty}^{\infty} \boldsymbol{f(t)} \boldsymbol{e^{-2\pi ist}} \boldsymbol{dt} \tag{2.20}$$

where $\boldsymbol{f(t)}$ is defined for all real numbers $\boldsymbol{t}$. For any $\boldsymbol{s} \in \mathbb{R}$, integrating $\boldsymbol{f(t)}$ against $\boldsymbol{e^{-2\pi ist}}$ with respect to $\boldsymbol{t}$ produces a complex valued function of $\boldsymbol{s}$. If $\boldsymbol{t}$ has dimention time then to make $\boldsymbol{st}$ dimentionless, $\boldsymbol{s}$ must have dimention 1/time.

Similarly the inverse Fourier transform can be defined as

$$\boldsymbol{f(t)} = \int_{-\infty}^{\infty} \widetilde{\boldsymbol{F}}(\boldsymbol{s}) \boldsymbol{e^{2\pi ist}} \boldsymbol{ds} \tag{2.21}$$

Assuming that $\boldsymbol{t} = \boldsymbol{time}$ and knowing that $\boldsymbol{s} = \boldsymbol{1/time}$ we can make the substitution $\boldsymbol{\omega} = \frac{\boldsymbol{2\pi}}{\boldsymbol{s}}$ resulting in a more convenient form of the equation:

$$\widetilde{\boldsymbol{F}}(\boldsymbol{\omega}) = \int_{-\infty}^{\infty} \boldsymbol{f(t)} \boldsymbol{e^{-i\omega t}} \boldsymbol{dt} \tag{2.22}$$

This form is more convenient, as meaning can be interpreted in it taking a function in the time domain and transforming it into a frequency dependent function in the frequency domain.

It is important to remember that the frequency dependent function $\widetilde{\boldsymbol{F}}(\boldsymbol{\omega})$ is complex,

having both real and imaginary components. The complex number z can be expressed as:

$$z = x + iy \tag{2.23}$$

where $i = \sqrt{-1}$

If one thinks of the real numbers being represented on an x-axis and the imaginary numbers being represented on a perpendicular y-axis the complex number then resides as a point on a plane seen in Figure 2.5

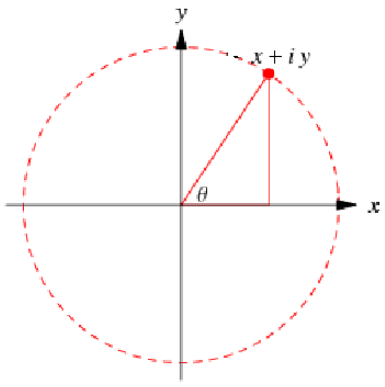

Figure 2.5: The complex plane

Eulers equation importantly relates a complex number to trignometric functions, described as:

$$z = |z|\left(\cos\theta + i\sin\theta\right) = |z|e^{i\theta} \tag{2.24}$$

where θ is know as the complex argument or phase and $|z|$ is known as the modulus or magnitude of the complex number, sometimes written as $r = |z| = \sqrt{x^2 + y^2}$

2.2.2 The Discrete Fourier Transform (DFT)

The Fourier transform deals exclusivly with continuous functions. In order to deal with any function defined at discrete intervals the DFT is used. This is an important step as it is not possible to implement a continuous Fourier transform numerically but a DFT can be implemented numerically.

The definition of the DFT is as follows:
For a sequence of complex numbers $\boldsymbol{f_k}$ the DFT $\boldsymbol{F_k}$ is

$$\boldsymbol{F_k} = \sum_{\boldsymbol{n=0}}^{\boldsymbol{N-1}} \boldsymbol{f_n} \boldsymbol{e}^{\frac{\boldsymbol{2\pi i k n}}{\boldsymbol{N}}} \tag{2.25}$$

and the Inverse is defined as

$$\boldsymbol{f_k} = \frac{\boldsymbol{1}}{\boldsymbol{N}} \sum_{\boldsymbol{n=0}}^{\boldsymbol{N-1}} \boldsymbol{F_n} \boldsymbol{e}^{\frac{\boldsymbol{2\pi i k n}}{\boldsymbol{N}}} \tag{2.26}$$

where $\boldsymbol{n = 0, 1, ..., N - 1}$

Discrete Fourier transforms are extremely useful because they reveal periodicity of input data as well as the relative strengths of any periodic components. There are a few subtleties in the interpretation of discrete Fourier transforms. In general, the discrete Fourier transform of a real sequence of numbers will be a sequence of complex numbers of the same length. This fact becomes important because in order to increase the resolution in the frequency domain, one needs to increase the data in the time domain. Because phenomena that are not repeating are being dealt with, it is possible to artificially increase the amount of data in the time domain by simply "padding" the end of the data with zeros [29]. This has no effect on the data in the time domain and simply increases the number of discrete points in the frequency domain thus increasing the resolution.

An important point to note is that each component of the DFT will split into "positive" and "negative" frequency components, which, depending on the term, can be "odd" or "even" functions through the frequency band. An example of this can be seen in Figure 2.6 where two simple sinusoid functions are combined and overlayed with random noise to hide the obvious periodicity. In Figure 2.6 the origional singnal is shown in the first pane and is generated as follows:

$$\boldsymbol{y(t) = 2.7 \sin(2\pi 50 t) + 5 \sin(2\pi 120 t)}$$

The second pane shows the signal with random noise overlayed while the final pane shows the magnitude or modulus of the Fourier transform of $\boldsymbol{y(t)}$. Note how the output is mirrored around the zero frequency.

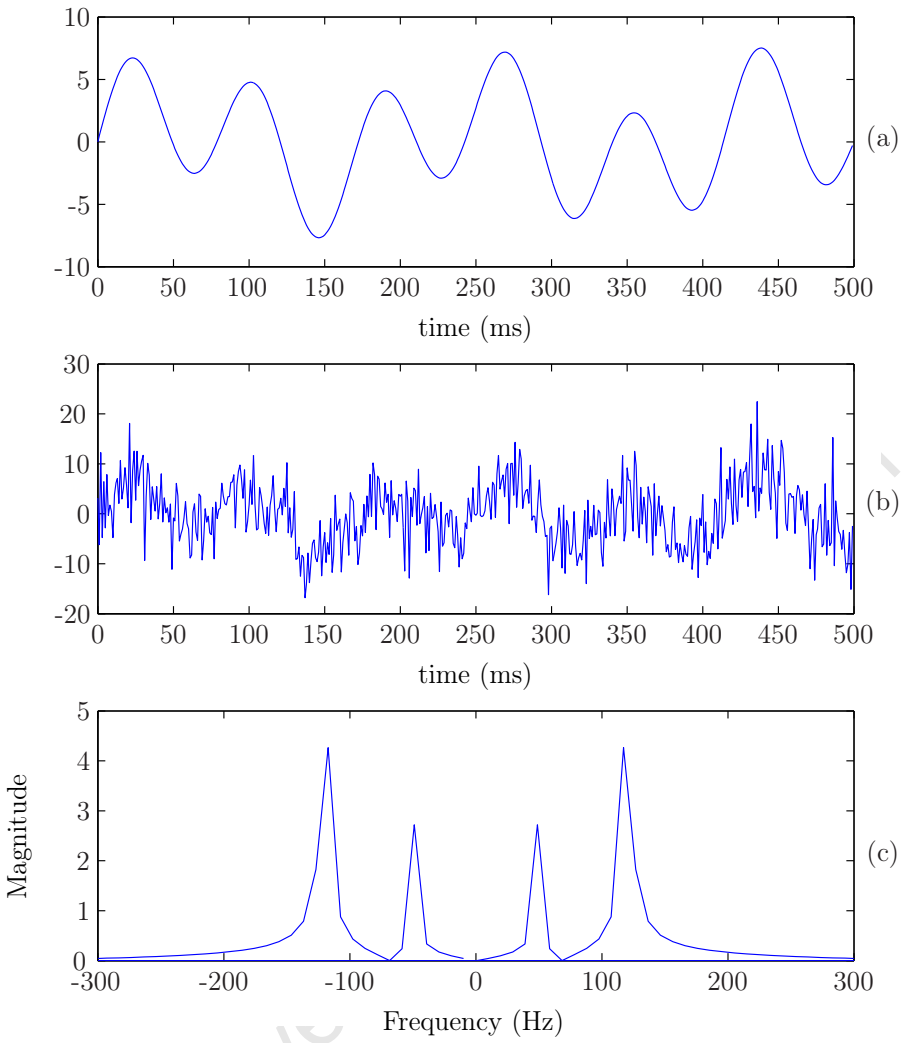

Figure 2.6: A typical amplitude spectrum from a Fourier transform showing (a) the origional signal (b) the origional signal with noise overlayed (c) the modulus of the FFT

2.2.3 The Fast Fourier Transform (FFT)

The discrete Fourier transform of a sequence of $\boldsymbol{N}$ points requires $O(\boldsymbol{N^2})$ arithmetic operations to compute if a straight forward implementation of its definition is carried out. For large $\boldsymbol{N}$, this can become prohibitive. In 1965, Cooley and Tukey rediscovered (it was previously used by Gauss and Runge) a very efficient way of calculating the discrete Fourier transform which involves $O(\boldsymbol{N \log N})$ operations. This is known as the fast Fourier transform (FFT) algorithm. Many variants of the FFT algorithm exist and

the one used here is that implemented by MATLAB which is the FFTW library [30, 31]. For a full explanation of the method implemented please see the technical documents for MATLAB which are accessible through their website [32].

2.3 Characterising A Viscoelastic Material

Viscoelasticity is of specific interest in this dissertation as it describes the polymeric Hopkinson bar materials of interest. Viscoelasticity is the property of materials that exhibit both viscous and elastic characteristics when undergoing deformation. The viscous component involves some form of damping or energy dissapation. Linear viscoelasticity is a subject which stretches in its influence and importance from the early years of rheology to the present day. The work of Maxwell, Boltzmann, Voigt, Kelvin and others fall within the area commonly referred to as linear vicoelasticity. It remains an important area of research and most modern characterisation studies involving viscoelastic materials will normally include interpretation of data arising from these models. The early 20th century saw the introduction of these 'mechanical' models which have proved popular in characterising linear viscoelastic materials. In these models, Hookean elastic deformation is represented by a spring and damping by a dashpot.

The Maxwell model is described by a spring and dashpot in series while the Kelvin-Voigt model is described by a spring and dashpot in parallel. The characterisation of more complex materials is accomplished by the combination of different models in different combinations. To some the introduction of the spring or dashpot analogy was unnecessary and obscured the straightforward notations of continuum mechanics [4].

Figure 2.7 shows the basic schematics of the Maxwell model and the expected stress response, while Figure 2.8 shows the expected response of a Kelvin-Voigt model.

Further analysis and investigation on this topic is conducted in Chapter 3 where the full derivation of the characterising equations for different models is presented together with the numerical implementation.

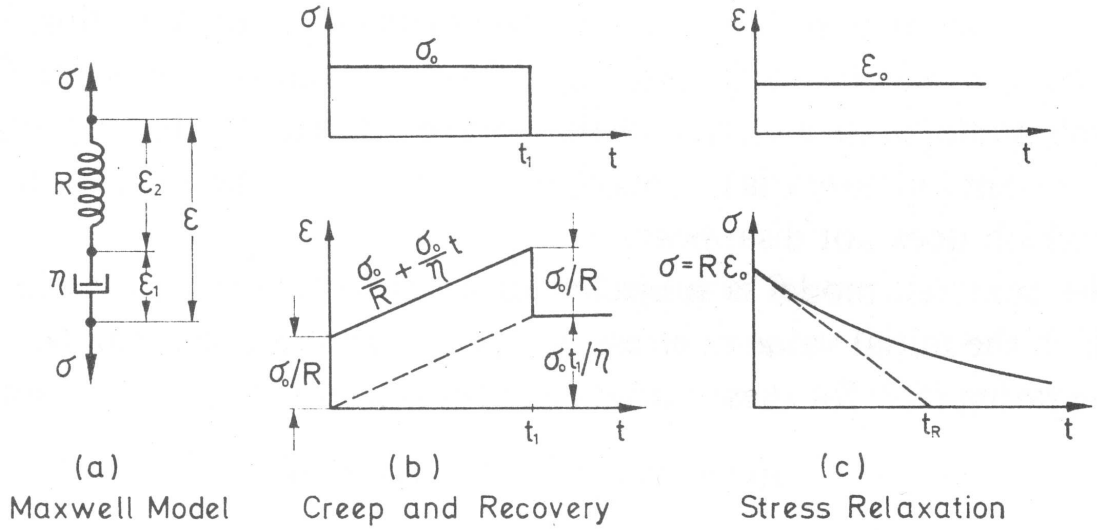

Figure 2.7: The behaviour of a Maxwell model [4].

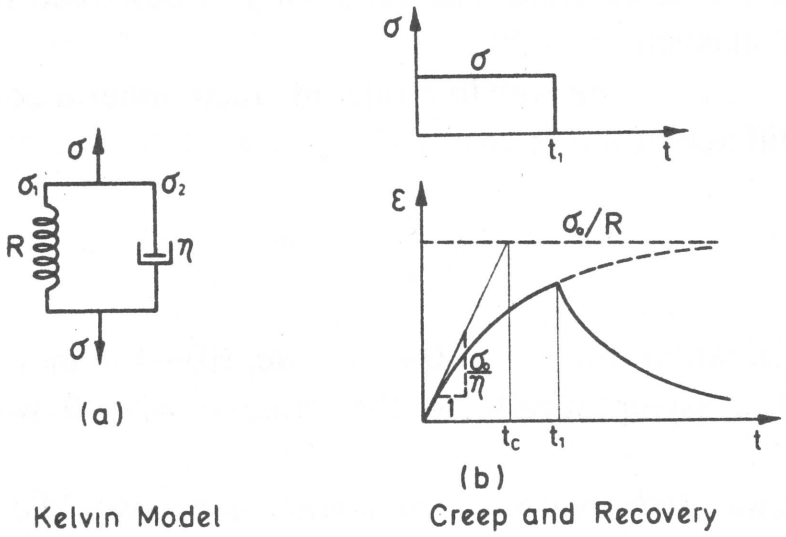

Figure 2.8: Behaviour of a Kelvin-Voigt model [4].

2.4 Viscoelastic Wave Propagation

Characterising viscoelastic wave propagation is important because unlike a metallic bar, where linear elastic assumptions are appropriate, viscoelastic materials have a marked damping effect on pulses. This is relevant in polymeric Hopkinson bars as the strains

measured at gauge stations are used to infer conditions at the specimen interface. If the strains measured at the gauge stations have been affected by the bar material behaviour then the equations used to infer specimen properties in Section 2.1.1 will not be a true indication of the conditions. The work done on dispersion correction in metallic bars deals with a similar idea, in that the pulse propagation down a bar is affected by geometric dispersion. In correcting for dispersion in metallic bars it is possible to more accurately define specimen response at the bar interface. This section presents the work conducted by different authors in chronological order to show the advancement of the techniques used fro viscoelastic wave propagation.

2.4.1 Blanc

Lundberg and Blanc (1998) [5] were among the first to implement an experimental technique which can be used to characterise the material properties of a viscoelastic polymer seen in Figure 2.9. In the paper the authors determine the mechanical properties of a linerly viscoelastic body from the body's response to impact. This is achieved by capturing the one-dimensional transient stress wave propagation at two points in a bar that is impacted on one end with a striker. The specific material properties they considered (characterised in the frequency domain) are the damping coefficient $\boldsymbol{\alpha(\omega)}$ and the wavenumber $\boldsymbol{k(\omega)}$ which are the real and imaginary parts respectively of the propagation coefficient $\boldsymbol{\gamma(\omega)}$. From this, the phase velocity $\boldsymbol{C}$ and the complex modulus $\boldsymbol{E = E' + E''}$ can be calculated. These functions of angular frequency $\boldsymbol{\omega}$ are interrelated in such a way that by the density of the material together with $\boldsymbol{\alpha}$ and $\boldsymbol{k}$, $\boldsymbol{\alpha}$ and $\boldsymbol{c}$ or $\boldsymbol{E'}$ and $\boldsymbol{E''}$ are known then the remaining functions can be determined. Blanc states that two different methodologies are discussed namely one using particle velocities which is dependent on wave superposition and another using particle strains which is independant of wave superposition. They conclude that both methods compliment each other in a frequency range of 20Hz - 20kHz.

It is important to note at this point that the complex modulus mentioned here is analagous to the youngs modulus. The difference is that the Youngs modulus is the function that relates stress to strain in the time domain while the complex modulus is the function that relates stress and strain in the frequency domain. [2]

In a follow up publication, Blanc (1993)[33] states that any homogeneous viscoelastic

[2]The terms related to the frequency domain are discussed in more detail in Section 2.2.1 which deals with Fourier analysis.

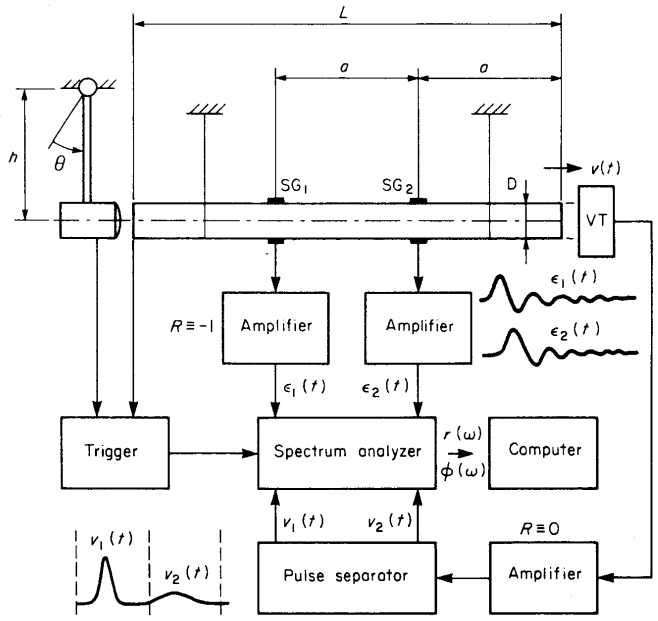

Figure 2.9: The experimental setup used by Blanc [5]

medium subjected to one dimensional tension or compression can be characterised in terms of the phase velocity $\boldsymbol{c(\omega)}$ and the attenuation co-efficient $\boldsymbol{\alpha(\omega)}$ of the longitudinal wave, from which it is possible to deduce the complex modulus. Here the jump from wavenumber $\boldsymbol{k(\omega)}$ to phase velocity is made by

$$\boldsymbol{k(\omega) = \frac{\omega}{C(\omega)}}$$

There are several possible ways of deriving these functions from a captured transient wave.

- One can attempt to integrate it exactly assuming a form of $\boldsymbol{c(\omega)}$ and $\boldsymbol{\alpha(\omega)}$. This approach is reported by Brodner and Kolsky (1958) [34] and further developed by Blanc and Champomier (1976) [35] for cases where only the wave front can be observed.

- Alternatly, a numerical solution for the wave propagation needs to be obtained, which has since been dealt with by a few authors [36, 37] and is discussed in Section 2.4.2 and 2.4.3.

2.4.2 WANG *et al*

Wang *et al* (1994) [36] make use of the nonlinear Zhu-Wang-Tang (ZWT) viscoelastic constitutive equation and characteristic wave propagation. If the wave propagation were not characterised, wave superposition could not be used to infer conditions at the bar ends due to the fact that wave superposition is based on 1D wave theory. This technique does not take geometric wave dispersion into account as pointed out in a response to a letter to the editor of the journal [38]. The form of the ZWT model is as follows [36]

$$\boldsymbol{\sigma = E_0\varepsilon + \alpha\varepsilon^2 + \beta\varepsilon^3 + E_1 \int_0^t \dot{\varepsilon}(\tau)^{\left(-\frac{t-\tau}{\theta_1}\right)} d\tau + E_2 \int_0^t \dot{\varepsilon}(\tau)^{\left(-\frac{t-\tau}{\theta_2}\right)} d\tau} \quad (2.27)$$

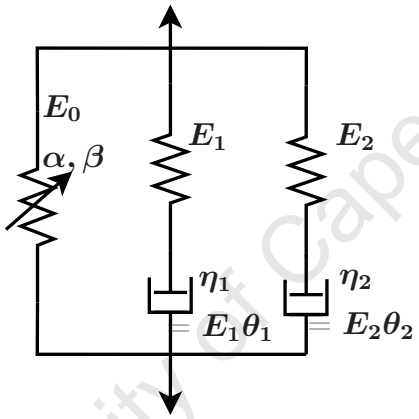

Figure 2.10: Schematic showing the spring dashpot representation of equation 2.27

The first three terms describe the nonlinear elastic response, and the $\boldsymbol{E_0}$, $\boldsymbol{\alpha}$ and $\boldsymbol{\beta}$ are the corresponding elastic constants. The first integral term describes the the viscoelastic response for low strain rates, $\boldsymbol{E_1}$ and $\boldsymbol{\theta_1}$ are the elastic constants and relaxation time of the corresponding Maxwell element [3] seen in Figure 2.10. The last integral term describes the viscoelastic response for high strain rates, $\boldsymbol{E_2}$ and $\boldsymbol{\theta_2}$ similarly being the elastic constant and relaxation time of the second Maxwell element.

By looking specifically at high strain rate events this model can be simplified as the first Maxwell element effectively acts elastically leaving us with $\boldsymbol{E_a = E_0 + E_1}$ and

$$\boldsymbol{\sigma = E_a\varepsilon + E_2 \int_0^t \dot{\varepsilon}(\tau)^{\left(-\frac{t-\tau}{\theta_2}\right)} d\tau} \quad (2.28)$$

[3] See Section 3.1.1 for a full description

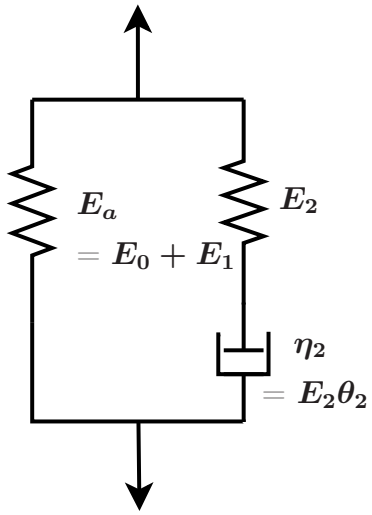

Figure 2.11: Rheological model showing the spring dashpot representation of equation 2.28

To use this model the nine different constants need to be solved for the material being used. One of the main differences between this method and others is that it cannot make use of a Fast Fourier Transform (FFT) because a nonlinear viscoelastic equation is used to describe the material. As a result the equation must be integrated analytically.

2.4.3 Zhao and Gary

Zhao and Gary [6, 37, 39, 40] use a 3D analytical solution for the longitudinal wave propagation which takes into account the geometric effects of the bar by not simply treating the the problem as a one dimensional problem. The difference between the 1D and 3D approaches can be seen in Figure 2.12.

The method is based on the Pochhammer [23] and Chree [24] frequency equation for propagation in an infinite rod studied numerically by Bancroft [25] and Davies [14] and generalised for a cylindrical infinite bar made of a linear viscoelastic material by Coquin [41]. This means that the constitutive law can be written in the frequency domain as follows:

$$\boldsymbol{\sigma}^*(\omega) = \boldsymbol{\lambda}^*(\omega)\boldsymbol{tr}(\varepsilon^*(\omega)) + \mathbf{2}\boldsymbol{\mu}^*(\omega)\varepsilon^*(\omega) \tag{2.29}$$

where $\boldsymbol{\sigma}^*(\omega)$, $\varepsilon^*(\omega)$, $\boldsymbol{\lambda}^*(\omega)$, $\boldsymbol{\mu}^*(\omega)$ are respectively the Stress tensor, the Strain tensor and the two material coefficients each of which are frequency dependent.

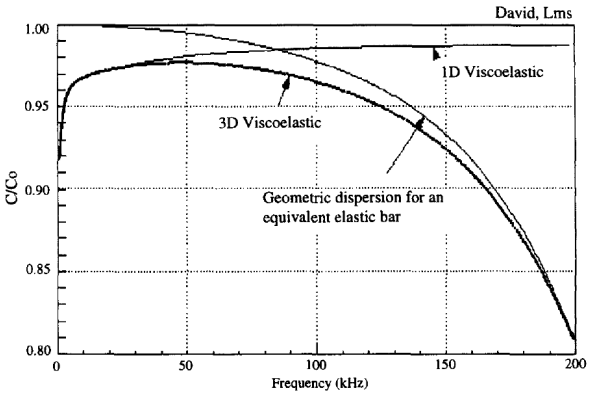

Figure 2.12: A comparison between the 1D and 3D viscoelastic assumptions contrasted with the geometric effects in a metallic bar [39].

They show that both the phase velocity and attenuation coefficient of the viscoelastic model are affected by the geometric effects dealt with by the new 3D methodology seen in Figure 2.13

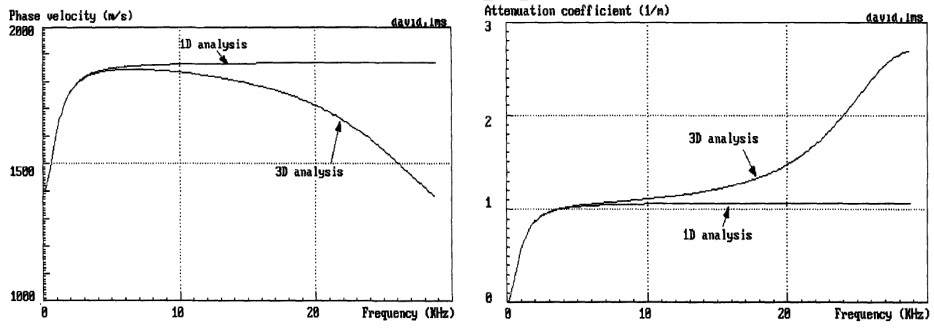

Figure 2.13: The phase velocity and attenuation co-efficients of the Zhao and Gary 3D analytical approach [6]

In order to use this method the bar material needs to be characterised and an example is presented briefly to illustrate this point. It is assumed that the functions $\boldsymbol{\lambda}^*(\boldsymbol{\omega})$ and $\boldsymbol{\mu}^*(\boldsymbol{\omega})$ have a pre-defined form with some parameters to be determined. If the material is assumed to have a form shown in Figure 2.14 then 9 parameters will need to be solved for in order to use this model successfully. It should be noted that this method is calibrated using a two gauge station measurement method for the separation of waves.

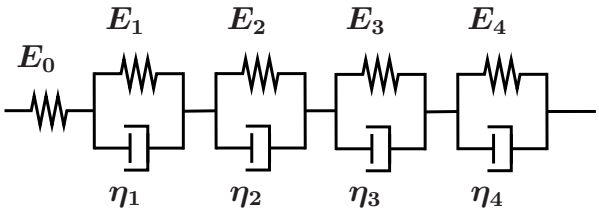

Figure 2.14: A rheological model for PMMA [6]

The resulting force balance at the bar interface is however very good as can be seen in Figure 2.15 for a test performed on 60mm diameter Nylon bar. It is interesting to note the high frequency oscillations which appear on the plateau of the signal. These oscillations are very similar to those studied by Pochammer and Chree. An explanation for these is the geometric dispersion associated with the large diameter bars which were used in the experimental setup by the author. It was shown by Govender [26], that as the bar diameter increases the influence of dispersion effects increases and Pochammer Chree oscillations will be seen.

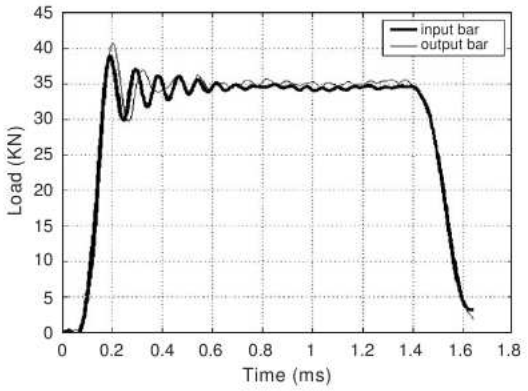

Figure 2.15: Comparison of the input and output forces of the bar ends using the Zhao 3D analytical correction [40] on Nylon bars

2.4.4 BACON

Bacon (1998) [2] presents an experimental method which characterises geometric and material viscosity effects on wave propagation. In this method the viscoelastic propagation coefficient, representative of the wave dispersion and attenuation, is evaluated experimentally. This negates the need for the Pochhammer and Chree frequency equation to be solved. The significant difference from other methods is that no specific model is explicitly assumed to explain the viscoelastic material behaviour. Instead a linear relationship between attenuation and dispersion in the frequency domain is assumed. The method is proposed for bars of any crossectional area and the material constants of the bar are not needed. Bacon presents the one dimensional equation of axial motion in the frequency domain as

$$\frac{\partial^2}{\partial x^2}\tilde{\sigma}(x,\omega) = -\rho\omega^2\tilde{\varepsilon}(x,\omega) \tag{2.30}$$

where $\tilde{\sigma}(x,\omega)$ and $\tilde{\varepsilon}(x,\omega)$ denote the Fourier transforms of stress and strain respectively. The angular frequency ω is related to the frequency f by $\omega = 2\pi f$. And the viscoelastic behaviour of the material can be described as follows:

$$\tilde{\sigma}(x,\omega) = E^*(\omega)\tilde{\varepsilon}(x,\omega) \tag{2.31}$$

where $E^*(\omega)$ is the complex Young's modulus of the material. Note that the form used by Bacon is not the same complex modulus mentioned by previous authors, but should rather be thought of as the function which relates stress and strain in the frequency domain. The propagation coefficient $\gamma = \gamma(\omega)$ is defined by

$$\gamma^2(\omega) = -\frac{\rho\omega^2}{E^*(\omega)} \tag{2.32}$$

From the above equations the one dimensional equation of motion for a viscoelastic bar becomes

$$\frac{\partial^2}{\partial x^2}\left(\frac{1}{-\gamma^2}\right)\tilde{\varepsilon}(x,\omega) = 0 \tag{2.33}$$

Bacon presents results that show good repeatability with this technique for various striker velocities and bar diameters. A narrow distribution can be seen in the experimental results in Figure 2.16 up to a frequency of 10 kHz shown in grey. Bacon plotted the dark line through the middle of the distribution and used that as the function describing the different parameters. Bacon defines phase velocity the same way that Zhao and Gary do, seen in Figure 2.13, but the attenuation coefficient is described

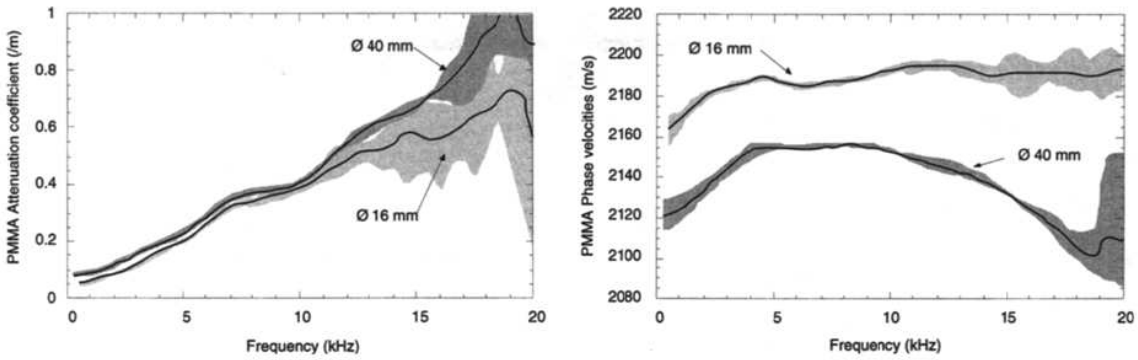

Figure 2.16: The phase velocity and attenuation co-efficient for a spread of experimental results [2]

differntly and above 10 kHz a much wider spread of data can be seen, the reason for which is not explained by the author.

2.4.5 Salisbury

Salisbury [42] presents an implementation of viscoelastic Hopkinson bars for dynamic material testing. Salisbury implements the experimental technique outlined by Bacon [2] and discussed in Section 2.4.4. Salisbury tests Polycarbonate, balistic gelatin and RTV silcone in order to validate the implementation. An automated numerical approach is developed using C++ to help simplify the process of correcting the signals obtained from viscoelastic bars. This is the main focus of Salibury's work and authors such as Ouellet [43] make use of Salisbury's code to perform data reduction in their own experimental studies.

2.4.6 Liu and Subhash

Liu and Subhash [44] present a novel iterative deconvolution integral in the time domain. This method defines an Impulse Response Function (IRF) $[\boldsymbol{H}]$ from two measured discrete strain signals $[\boldsymbol{X}]$ and $[\boldsymbol{Y}]$.
The definition of a convolution between two functions $\boldsymbol{f}$ and $\boldsymbol{g}$ can be defined by

$$(\boldsymbol{f} \otimes \boldsymbol{g})(\boldsymbol{t}) = \int_{-\infty}^{\infty} \boldsymbol{f}(\boldsymbol{\tau})\boldsymbol{g}(\boldsymbol{t}-\boldsymbol{\tau})\boldsymbol{d\tau} \tag{2.34}$$

and deconvolution can be thought of as the inversion of a convolution equation, so in the case of Liu

$$\begin{aligned} [\boldsymbol{X}] \otimes [\boldsymbol{H}] &= [\boldsymbol{Y}] \\ [\boldsymbol{H}] &= [\boldsymbol{Y}]/[\boldsymbol{X}] \end{aligned} \tag{2.35}$$

where "$\otimes$" stands for the convolution and "/" stands for the deconvolution.

This method is different to others seen as it leaves all measured components in the time domain, negating the need to use a FFT to determine the frequency dependant functions. This method is used successfully by the authors to predict wave behaviour in a bar seen in Figure 2.17, which uses two gauge stations on the same bar.

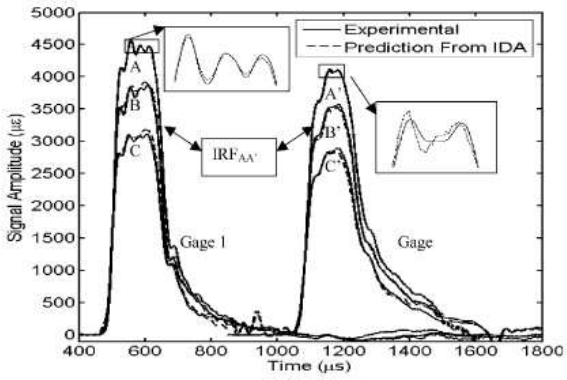

Figure 2.17: Comparison of the measured and predicted signals at the strain gauges presented by Liu *et al* [44]

2.5 Polymeric Hopkinson Bars

The following section is presented to show the different implementations of polymeric SHPB's in the literature. The approaches have been grouped according to the different bar materials used in order to contrast the different approaches taken in dealing with the viscoelastic properties of the bars.

For consistentcy, polymeric materials in this section appear under the original names given by the authors, but can be grouped into the following three categories:

- **NYLON**
- **Polymethyl methacrylate (PMMA)** also known as acrylic or perspex
- **Polycarbonate (PC)** also known under the trade name LEXAN®or plexiglass

2.5.1 NYLON Bars

Zhao *et al* [40] make use of a 60mm diameter NYLON bar to perform direct impact tests on aluminium honeycomb at velocities up to 50 m/s. Using the longer duration pulse length achieved by implementing the polymeric bars it was possible for Zhao *et al* to present data for over **1.8**ms. This allowed them to capture the crushing and densification of the aluminium specimens. Merle and Zhao [45] note that non-uniformities exist in the stress field accross the diameter when using large diameter Hopkinson bars such as those previously used by Zhao [37, 39, 40]. Merle and Zhao propose a correction method for dealing with these non-uniformities allowing more accurate results to be attained.

Bouix *et al* [46] performed a comprehensive set of tests on polypropylene involving dynamic tests on a 40 mm diameter NYLON SHPB setup. Bouix states that PMMA bars were considered for the experimental setup but not used due to the higher yield stress of NYLON which would allow a higher maximum stress level in the bars. Data reduction is performed using the method set out by Bacon in Section 2.4.4.

Kiernan [47] uses 50 mm diameter 30% glass filled NYLON input and output bars to test the functionally graded foam ALPORAS ®. Low projectile velocities were used by the author in an attempt to reduce wave dispersion in the bars. This was not successful and a FFT was used to shift the captured strain data into the frequency domain where Zhao and Gary's data reduction technique was used to correct for dispersion.

Shim [7] tested polyurea at low intermediate and high strain rates. A modified Hopkinson bar setup using NYLON bars and an hydraulic actuator in place of a striker is used, seen in Figure 2.18. The data analysis is carried out using the methods described by Zhao and Gary [6], note the three gauge stations used on both the input and output bars.

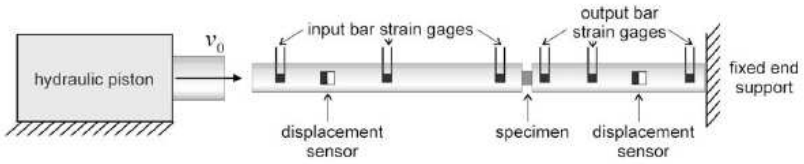

Figure 2.18: The modified Split Hopkinson Bar setup by Shim [7] using NYLON bars.

2.5.2 Polycarbonate Bars

Shim [8] tested three polyurethane elastomers in sheet form using a polycarbonate bar setup comprising 10.5 mm diameter input and output bars.

Two separate gauge stations separated by 510 mm seen in Figure 2.19 were used on the input bar to evaluate the viscoelastic effects of the bars. The reported strain signals can be seen in Figure 2.20, notice how similar the wave form looks at location 1 and location 2.

Using this signal, together with dynamic compression tests performed on LEXAN 141 showing an initial elastic response, Shim motivates that the viscoelastic effects of the

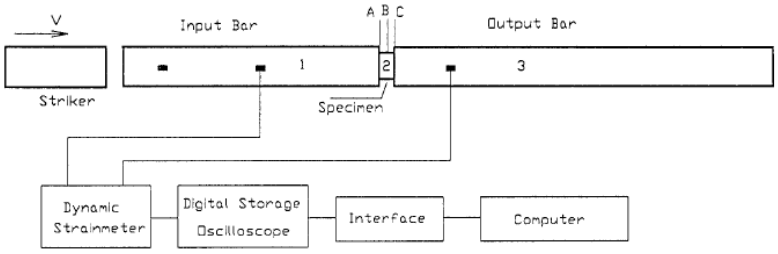

Figure 2.19: The Split Hopkinson Pressure Bar setup used by Shim [8] using PC bars.

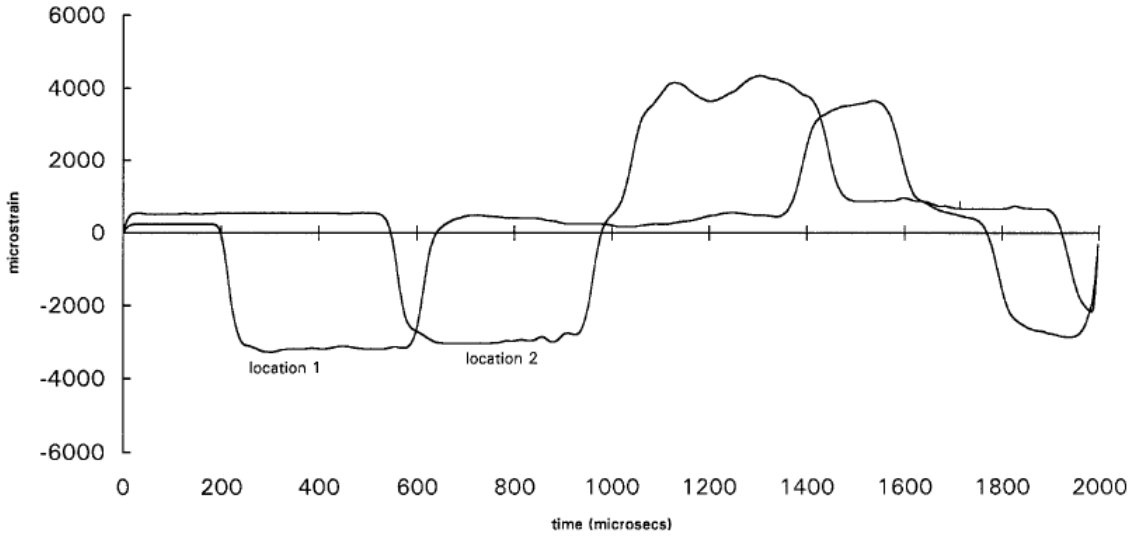

Figure 2.20: The incident wave form at the two gauge station reported by Shim [8] using PC bars.

bar material are negligible. As a result he applies elastic theory to the Hopkinson bars and uses them in the same way one would use a metallic bar to solve for forces and velocities at the specimen interfaces.

Martins *et al* [48] performed three point bend tests using a modified Hopkinson bar as an input bar seen in Figure 2.21. To do this they used a 19mm diameter LEXAN ® as both a striker and input bar. The analysis ignores the viscoelastic properties of the input bar and striker, instead assuming that elastic wave theory is applicable. The authors do not motivate why the viscoelastic properties of the input bar have been neglected.

Yang *et al* [49] used polycarbonate bars to perform impact tests on rubber samples

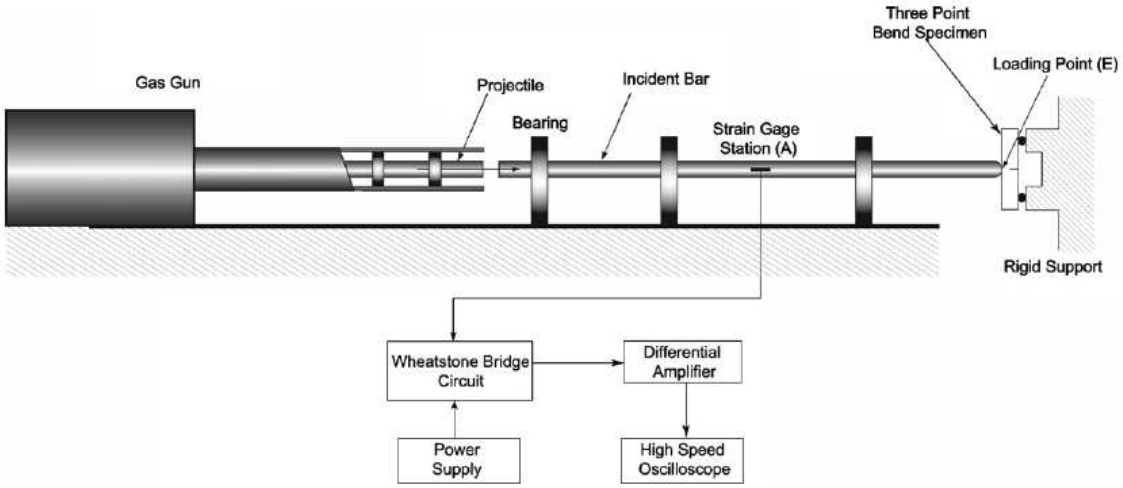

Figure 2.21: The modified Hopkinson pressure bar used by Martin *et al* [48] implementing PC bar.

to verify the hyper-viscoelastic model developed in the paper. No specifics of the experimental technique are given so no further comments can be made on the approach taken.

Yunoshev [50] uses 20mm diameter plexiglass bars to test Spheroplastic, PVC foam and Technical rubber. Spheroplastic is a quasi-isotropic composite with an epoxy matrix and dispersed inclusions in the form of glass microspheres. Single gauge stations are used on each of the bars and the standard linear solid model is used to account for the viscoelastic nature of the bars seen in Figure 2.22 in a similar approach to that followed by Wang *et al* 2.4.2.

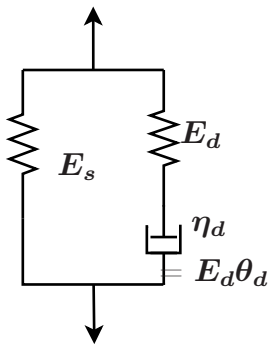

Figure 2.22: Rheological model showing the spring dashpot representation of equation 2.28.

with the following values $\boldsymbol{E_s} = \mathbf{5}$ GPa, $\boldsymbol{E_d} = \mathbf{0.7}$ GPa, $\boldsymbol{C_v} = \pm\mathbf{2200}$ m/s , $\boldsymbol{\alpha = 0.2m^{-1}}$ and $\boldsymbol{\theta_d = 141\mu sec}$ [4]

Sharma [51] tested soft materials (Clay, Sorbothane and Bologna) using a viscoelastic SHPB setup comprising 19mm diameter LEXAN ® bars. Additionally PMMA strikers were reportedly used which appears to be the first use of dissimilar polymers in the same system noted. For data reduction Bacon's method discussed in Section 2.4.4 was initially used. This was later replaced as it reportedly under predicted the specimen strains due to the fact that the technique is dependant on the sample frequency and pulse duration. It is however possible that the specimens were experiencing multiple loadings which is not discussed by the author. As a result, a 3-parameter Kelvin model developed by Fourney [5] was used for the data analysis.

2.5.3 Polymethyl Methacrylate Bars

Sawas [9] used cast acrylic bars of 25.4 mm diameter for both his incident and transmitter bars with multiple gauge stations shown in Figure 2.23 . In addition titanium anvil faces (0.6mm thick) were placed between the bars and the specimen interface to prevent damage to the bar faces.

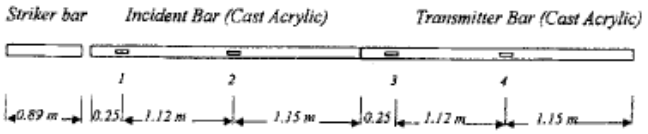

Figure 2.23: Schematic of Sawas experimental setup [9].

In order to deal with the viscoelastic effects of the bars Sawas uses a technique outlined by Kaya [52][6] using these multiple gauge stations to characterise the stress waves as they propagate down the bars. Calibration tests were first carried out on the bars using the multiple gauge stations and during testing only one gauge station on each bar was used. Sawas tests three different materials as proof of the method, namely polycarbonate, polyurethane and styrofoam. These materials cover a large range of

[4] In the paper no explanation is given by the author on how these results were derived.

[5] The only reference to this found was a reported private conversation with Fourney.

[6] Unfortunatally this paper could not be sourced and as a result no comment on the technique can be offered.

different material impedance. The results for tests performed on styrofoam can be seen in Figure 2.24

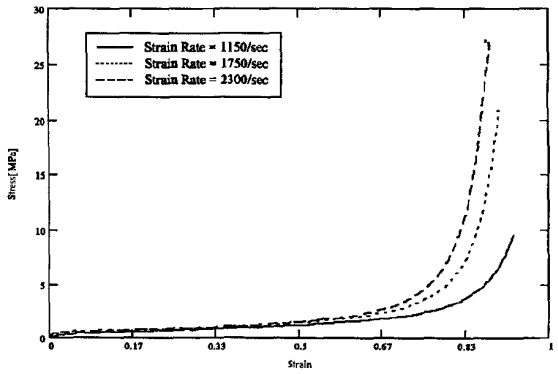

Figure 2.24: Stress Strain data for styrofoam obtained by Sawas [9].

Ouellet *et al* [43] tested polystyrene, high-density polyethylene and polyurethane at low, medium and high strain rates to show the rate dependence of polymer foams. The high strain rate tests were conducted on a split Hopkinson bar setup using 25.4mm diameter acrylic bars. $\mathbf{1000\Omega}$ semiconductor strain gauges were placed on both the incident and transmitted bars which are significantly more sensitive than conventional foil strain gauges and ensure that very small strain signals can be measured. The viscoelastic effects of the bars are dealt with using the same method outlined by Salisbury [42] and the software programmed by Salisbury is used to calculate the final results for the tests.

Subhash tests both low ($\boldsymbol{\rho < 1g/cm^3}$) and high density ($\boldsymbol{\rho > 1g/cm^3}$)epoxy based foams [53]. The low density foams were tested on an acrylic Hopkinson bar setup while the more dense foam specimens were tested using metallic bars. Later the authors [54] test only low density epoxy based foams seen in Figure 2.26 using confined and unconfined, quasi-static and dynamic tests. The unconfined Split Hopkinson bar tests were conducted using acrylic input and transmitter bars while the confined tests were conducted using metallic bars. The bars used were 19mm diameter cast acrylic bars. The data reduction on the viscoelastic bars was performed using the authors own custom deconvolution integral in the time domain outlined in Section 2.4.6 . The

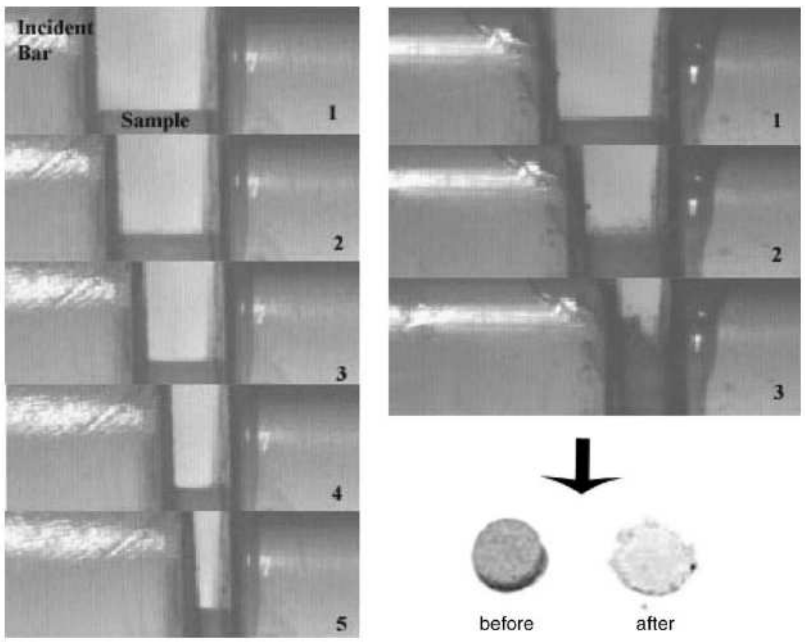

Figure 2.25: High speed images from tests performed on polystyrene and polyurethane foam [43]

confined dynamic tests were conducted on metallic bars due to the significantly higher force transmission using the confined method.

Subhash *et al* [53] use a particlarly different gauge setup on their bars. Instead of the two gauge setup seen in the work of other authors they make use of three gauges seen in Figure 2.27. This is set up in such a way that on the polymer bars the distance betwenn gauge 1 and 3 is used to characterise the viscoelastic material effects. The remaining gauges are placed this exact same distance from the bar ends so that the characterisation from gauge 1 and 3 can be used. Subhash *et al* use the iterative deconvolution technique descibed in Section 2.4.6 which it appears is unable to scale the viscoelastic effects to distances other than that which it was characterised over.

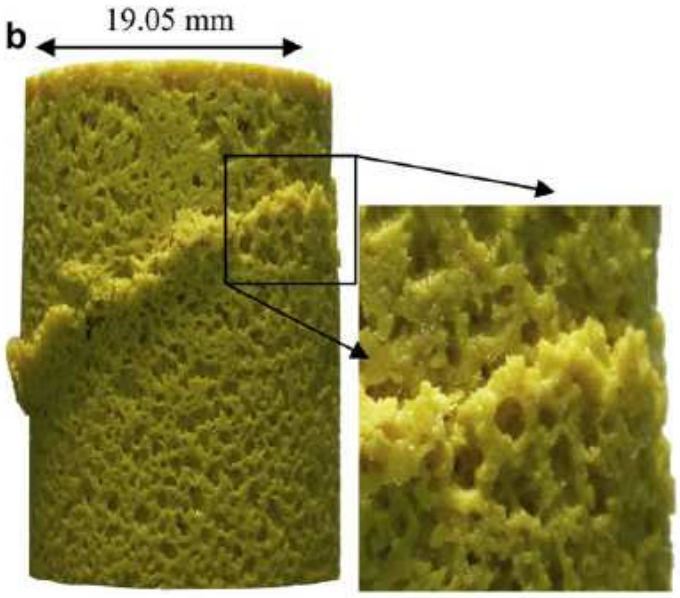

Figure 2.26: Typical fracture of polymeric foam seen by Subhash [54] when not tested in a confined configuration

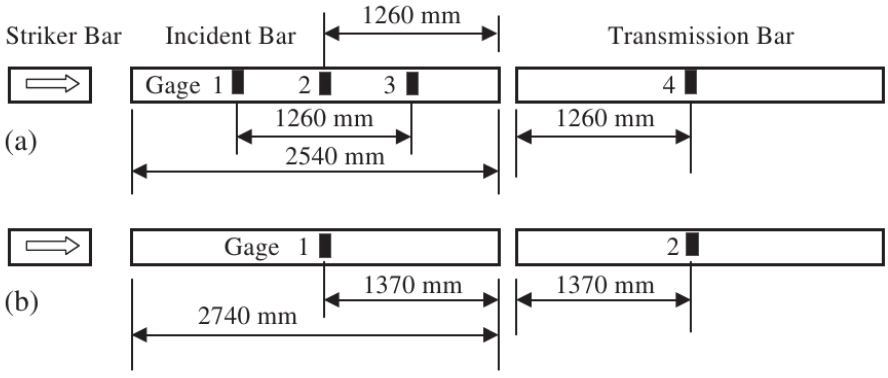

Figure 2.27: Schematic of the two SHPB systems used by Subhash *et al* . (a) Polymer SHPB, and (b) magnesium SHPB

Chapter 3

Polymeric Material Response

The purpose of this chapter is to emphasise the importance of viscoelastic material models and to highlight some of the difficulties of working with them. A background to viscoelasticity is presented and followed by some of the different models used to understand their behaviour. Finally one model is implemented and the results of this are presented.

The response of most materials to mechanical, electrical, optical and other fields is time-dependent. The study of the responses to these force fields allows one to determine the rheological, dielectric and birefringence properties of materials. According to the second law of thermodynamics, part of the input energy involved in the perturbation must invariably be dissipated, and part of it is stored. It should be pointed out that dissipation of energy does not occur instantaneously as it may take place in an infinitely short, infinitely long, or finite time depending on the thermodynamic state and nature of the material. In rheology, the perturbation is a mechanical force, and the response is a deformation that in certain cases becomes flow.

Part of the energy involved in the deformation is stored elastically, and part is dissipated through viscous mechanisms. Because some of the energy is dissipated, the response always lags behind the perturbation. The duration of the perturbation directly effects the amount of lag. This is a consequence of the fact that in a short perturbation the molecules comprising the material cannot rearrange sufficiently fast to accommodate to it, whereas in a perturbation of large duration there is plenty of time for molecular rearrangements. The response also depends on the intensity of the perturbation.

Perfectly elastic deformation and perfectly viscous flow are idealisations under very specific conditions. In general, condensed matter has a fading "structural memory", and

the velocity with which a system that has been perturbed "forgets" the configuration that it had in the past roughly defines its solid or liquid nature. In ordinary liquids, molecular reorganisation occurs very rapidly and structural memory at the molecular level is short. The response is essentially viscous unless frequency of the the testing experiment is very high. Consequently the mean relaxation time, roughly defined as the time necessary for the system to "forget" the configuration it had previous to the perturbation, is very small. In solids, on the other hand, the relaxation of structure at the molecular level is extremely low. The response is essentially elastic. However, the distinction between solid (or elastic) and liquid (or viscous), is not an absolute distinction between different classes of materials.

Polymers are arguably the most important viscoelastic systems. Above the glass transition temperature $\boldsymbol{T_g}$ where polymers would would be considered solid, the response of these materials to a mechanical perturbation involves several types of molecular motion of the polymer chains which make up the material. It is this interaction of polymeric chains on a molecular level which gives rise to the viscoelastic effects seen in the response of polymers.

3.1 Determination of Viscoelastic Properties

There are a great number of techniques for the experimental determination of viscoelastic functions. The techniques most frequently found in the literature are devoted to measuring the relaxation modulus, the creep compliance function, and the components of the complex modulus in either shear, elongational, or flexural modes. Although the relaxation modulus and creep compliance functions are defined in the time domain, where as the complex viscoelastic functions are given in the frequency domain. It is possible using a Fourier transform, to pass from the time domain to the frequency domain or vice versa.

The mechanical response of viscoelastic materials to mechanical excitation has traditionally been modelled in terms of elastic and viscous components such as springs and dashpots. The corresponding theory is analogous to electric circuit theory, which is extensively described in engineering textbooks [55]. In many respects the use of mechanical models plays an important role in interpreting the viscoelasticity of materials in the simplest cases. However the representation of the viscoelastic behaviour in

terms of springs and dashpots does not imply that these elements reflect the molecular mechanisms causing the actual relaxation behaviour of complex materials.

All the methods presented below are easily implemented numerically and can be used to approximate the behaviour of polymers. The greatest difficulty in using these models is finding the correct values to use for the different parameters.

3.1.1 The Maxwell Model

The Maxwell model seen in Figure 3.1 has a spring in series with a dashpot. The important relation between these two is the fact that the stress or force will be the same across each component.

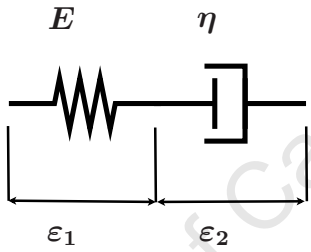

Figure 3.1: The Maxwell model

When this element is exposed to a step displacement, the strain in the element is given by

$$\varepsilon = \varepsilon_1 + \varepsilon_2 \tag{3.1}$$

where ε_1 and ε_2 are the strains of the spring and dashpot respectively. Since the stresses in the spring and dashpot are the same

$$\varepsilon_1 = \frac{\sigma}{E} \tag{3.2}$$

$$\dot{\varepsilon_2} = \frac{\sigma}{\eta} \tag{3.3}$$

combining these together

$$\dot{\varepsilon} = \frac{\dot{\sigma}}{E} + \frac{\sigma}{\eta} \tag{3.4}$$

3.1.2 Kelvin-Voigt model

The Kelvin-Voigt model seen in Figure 3.2 comprises a spring in parallel with a dashpot. The important relation in this instance is the fact that the displacement or strain of

each component will be the same.

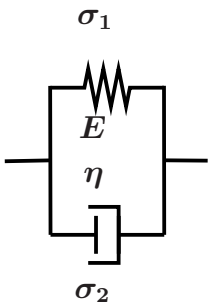

Figure 3.2: The Kelvin-Voigt model

When this element is exposed to a step displacement, the stress in the element is given by

$$\begin{aligned} \sigma &= \sigma_1 + \sigma_2 \\ &= E\varepsilon + \eta\dot{\varepsilon} \end{aligned} \tag{3.5}$$

3.1.3 Standard Linear Solid model

The Standard Linear Solid model comprises a Maxwell element in parallel with a spring seen in Figure 3.3.

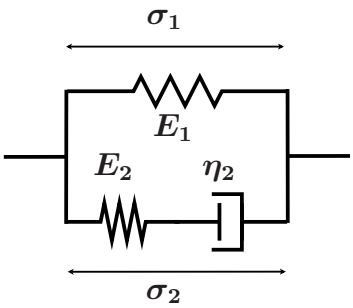

Figure 3.3: The Standard Linear Solid model

In this model the stress is split between the two legs such that

$$\sigma = \sigma_1 + \sigma_2 \tag{3.6}$$

where $\sigma_1 = E_1\varepsilon$ and

$$\dot{\varepsilon} = \frac{\dot{\sigma}_1}{E_1} + \frac{\sigma_2}{\eta_2} \tag{3.7}$$

which leads to the generalised form

$$\dot{\boldsymbol{\sigma}}\frac{\boldsymbol{\eta_2}}{\boldsymbol{E_2}} + \boldsymbol{\sigma} = \frac{\boldsymbol{\eta_2}}{\boldsymbol{E_2}}(\boldsymbol{E_1} + \boldsymbol{E_2})\dot{\boldsymbol{\varepsilon}} + \boldsymbol{E_1}\boldsymbol{\varepsilon} \tag{3.8}$$

3.1.4 Shim model

The Shim model seen in Figure 3.4 puts a Maxwell element in parallel with a Kelvin-Voigt element. In this instance the strains of each element will be the same and the stresses will be additive.

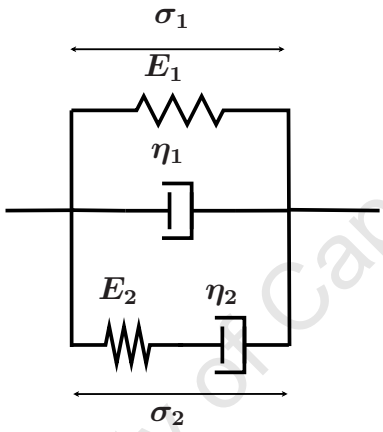

Figure 3.4: The Shim model

$$\boldsymbol{\sigma} = \boldsymbol{\sigma_1} + \boldsymbol{\sigma_2} \tag{3.9}$$

Now for the Kelvin-Voigt branch we have

$$\boldsymbol{\sigma_1} = \boldsymbol{E_1}\boldsymbol{\varepsilon} + \boldsymbol{\eta_1}\dot{\boldsymbol{\varepsilon}} \tag{3.10}$$

and for the Maxwell branch we have

$$\dot{\boldsymbol{\varepsilon}} = \frac{\dot{\boldsymbol{\sigma}}_{\boldsymbol{2}}}{\boldsymbol{E_2}} + \frac{\boldsymbol{\sigma_2}}{\boldsymbol{\eta_2}} \tag{3.11}$$

equating these terms

$$\begin{aligned} \dot{\boldsymbol{\sigma}} &= \boldsymbol{E_1}\dot{\boldsymbol{\varepsilon}} + \boldsymbol{\eta_1}\ddot{\boldsymbol{\varepsilon}} + \boldsymbol{E_2}\dot{\boldsymbol{\varepsilon}} - \frac{\boldsymbol{E_2}}{\boldsymbol{\eta_2}}\boldsymbol{\sigma_2} \\ &= \boldsymbol{\eta_1}\ddot{\boldsymbol{\varepsilon}} + (\boldsymbol{E_1} + \boldsymbol{E_2})\dot{\boldsymbol{\varepsilon}} - \frac{\boldsymbol{E_2}}{\boldsymbol{\eta_2}}\boldsymbol{\sigma_2} \end{aligned} \tag{3.12}$$

Finally by eliminating the remaining $\boldsymbol{\sigma_2}$ term

$$\boldsymbol{\sigma}\frac{\boldsymbol{E_2}}{\boldsymbol{\eta_2}} + \dot{\boldsymbol{\sigma}} = \boldsymbol{\eta_1}\ddot{\boldsymbol{\varepsilon}} + \left[\boldsymbol{E_1} + \left(\mathbf{1} + \frac{\boldsymbol{\eta_1}}{\boldsymbol{\eta_2}}\right)\boldsymbol{E_2}\right]\dot{\boldsymbol{\varepsilon}} + \frac{\boldsymbol{E_1}\boldsymbol{E_2}}{\boldsymbol{\eta_2}}\boldsymbol{\varepsilon} \tag{3.13}$$

3.2 Quasistatic Material Tests

A set of quasistatic tests were performed on samples of the material from the three intended bar materials. The purpose of performing these test were to have a starting point from which it is possible to attempt to calibrate an analytical model. The quasistatic tests were performed on a Zwick 1484 test machine with a maximum load of 200 kN with a Zwick/Roell control system. The specimens were tested under compression loading in accordance with the ASTM testing standards for rigid plastics in compression [56]. Specimens were cut from the same material used for the bars mentioned later in Chapter 4 to ensure that any material properties derived could be used to calibrate the response of the bars.

Figures 3.5 , 3.6 and 3.7 show the response of the different materials. The results of the test can be summarised in Table 3.1

Material	Yield Strength (MPa)	Young's Modulus (GPa)
PC	85.6	1.58
NYLON	65.3	1.69
PMMA	130	2.03

Table 3.1: The results of the quasistatic compression tests.

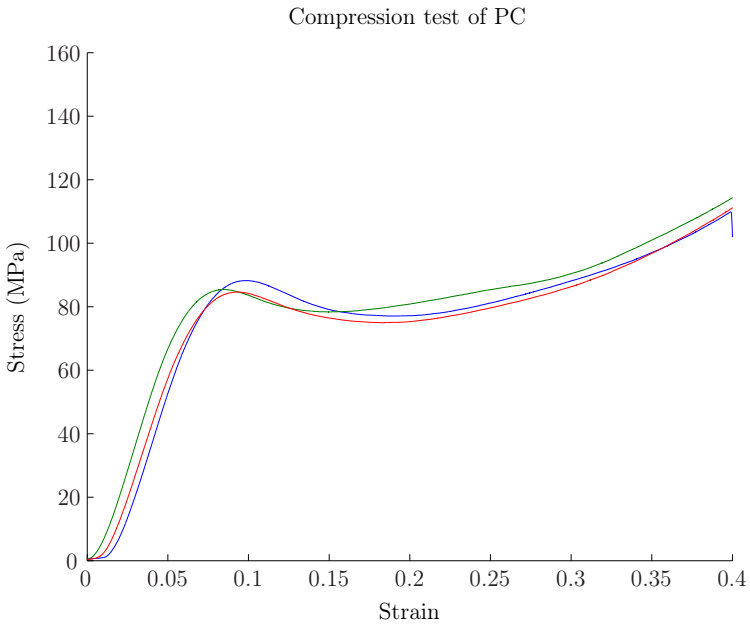

Figure 3.5: Quasistatic testing of PC

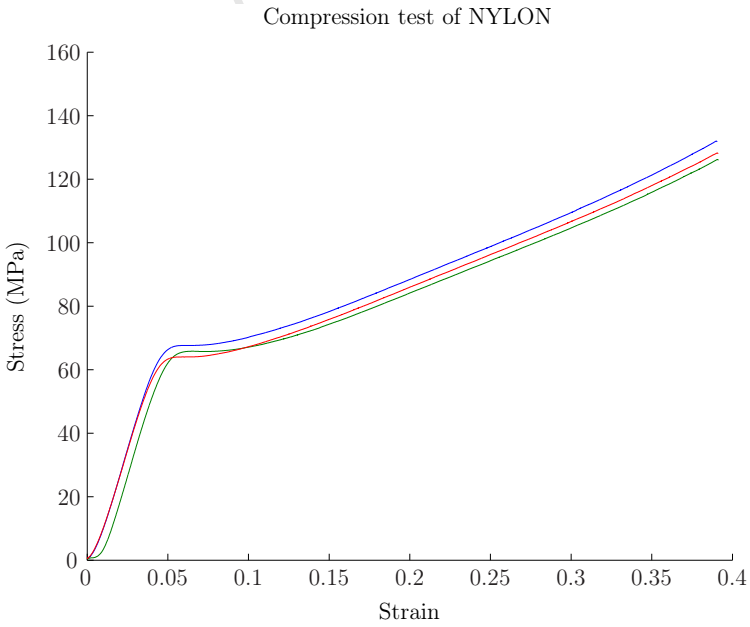

Figure 3.6: Quasistatic testing of NYLON

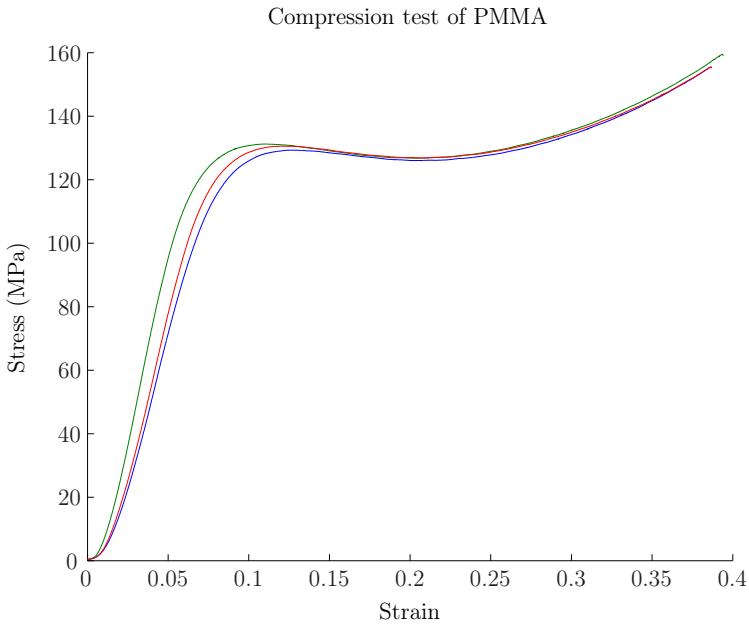

Figure 3.7: Quasistatic testing of PMMA

3.3 Implementation

The Maxwell and Kelvin-Voigt models have been frequently used in literature and their response has been well documented. The expected response from the Maxwell and Kelvin-Voigt models to a step pulse can be seen in Figure 2.7 and 2.8.

The decision was taken that the Shim model from Section 3.1.4 would be implemented in an attempt to replicate the behaviour of the polymeric materials. The tap tests in Section 4.2 give an idea of the expected response for each material that was being replicated using the numerical model.

The model is implemented in MATLAB and the code used can be seen in Appendix B. To start with the main spring in the model $\boldsymbol{E_1}$ was set to the quasistatic Young's Modulus of the material and then the other three variables were changed until the response of the model came close to matching the observed response of the bar material. The model mimics the actual geometry of the bars being 2 m in length and having a diameter of 20 mm. The bar was discretized into 1000 elements with a time step applied being smaller than the critical time step taken for a stress wave to propagate the length of a single element.

The model was excited with a unit step displacement which acts on the bar end for

a limited period of time and the other end of the bar was left as an unconstrained free end.

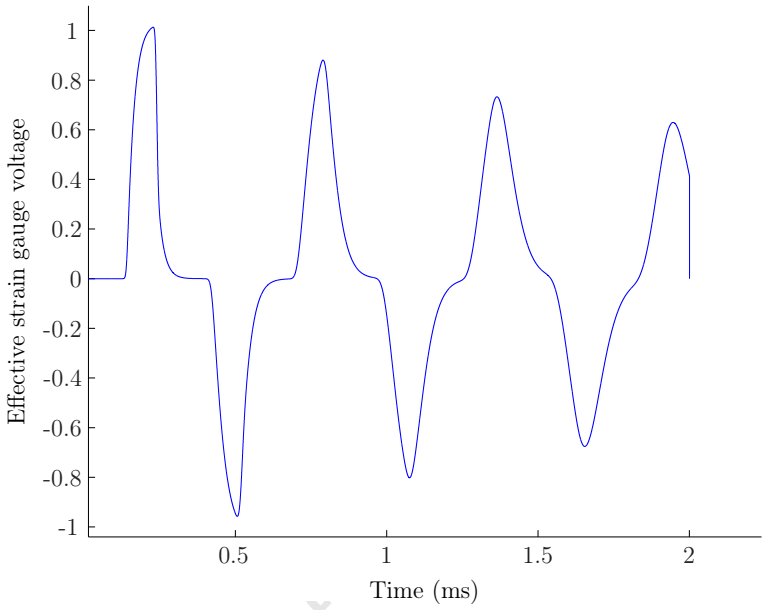

Figure 3.8: Shim model replicating PMMA behaviour.

It was found however that the model was unable to replicate all three of the materials closely. By changing the parameters it was possible to achieve a response that appears to closely match the initial pulses seen in the tap tests. However as the system is allowed to vibrate the reflection produced by the model deviates from the test data. The material that was most closely matched was the PMMA seen in Figure 3.8, as both the initial pulse and the subsequent reflections were much closer to the actual test data. This observation alludes to the possibility that PMMA is a material that can be very closely modelled by a linear viscoelastic model. This would have important implications to its use by authors in the literature who make use of PMMA bars together with analytical models based on a linear viscoelastic material model.

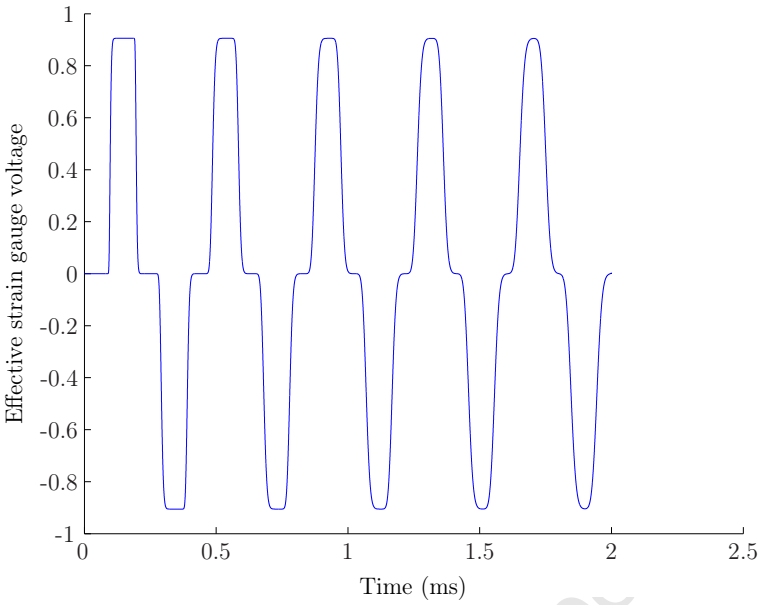

Figure 3.9: Shim model replicating PC behaviour.

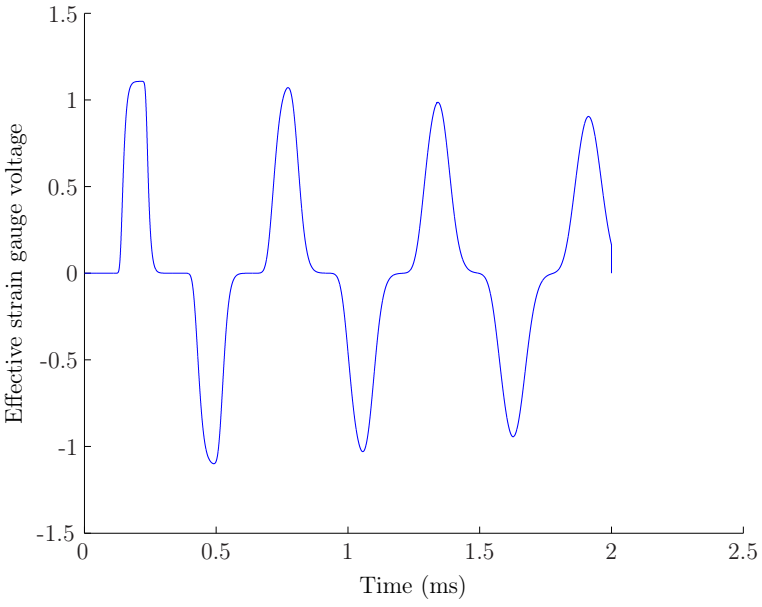

Figure 3.10: Shim model replicating NYLON behaviour.

Chapter 4

Experimental Methodology

The Purpose of this chapter is to outline the different methods and procedures used while performing tests on the Hopkinson bars.

The choice of bar materials used was largely driven by the information found in the literature. Three main materials are used in the literature, namely NYLON, Polycarbonate (PC) and Polymethyl methacrylate (PMMA). No comparison of these materials could be found and authors often did not state any reason for a specific material choice. It was therefore decided to use all three of the materials and attempt to contrast any difference that can be seen in the use of the different materials in Hopkinson bars.

A round extruded bar, 3m in length, of each of the materials was purchased from Maizey Plastics in Cape Town. Each of the bars was sold nominally as 20mm diameter, however this measurement was not exact due to die swell of the material during the extrusion process as is reflected in Table 4.1.

To start with each of the bars was gauged using KYOWA foil gauges in a diametrically opposed gauge station to cancel any bending effects in the bars. Each of the bars had tap tests performed on them to generally assess the material response. Following this calibration tests were performed on each of the bars to determine the material properties and finally tests were performed using the each of the bars together with a magnesium bar.

4.1 Strain Gauging and Data Capture

Each of the Hopkinson bars used were gauged with diametrically opposed gauges to cancel bending effects in the bars. Dummy gauges were used for both temperature

	Nylon	PC	PMMA	Magnesium
Bar diameter (mm)	21.1	20.7	20.5	20.0
Density (kg/m^3)	1155	1202	1204	1791
Wave speed [1](m/s)	1710	1436	2180	4968
Length (m)	2.000	1.999	2.000	2.000

Table 4.1: The properties of the Hopkinson bars used

compensation in the bars and balancing the bridge resistance.The dummy gauges together with the active gauges form a gauge station. Figure 4.1 shows the layout of the gauges where Rg1 and Rg3 measure the strain while Rg2 and Rg4 are the dummy gauges. The dummy gauges were specifically placed on the same polymeric material as the bar with which they were used to accuratley account for thermal changes.

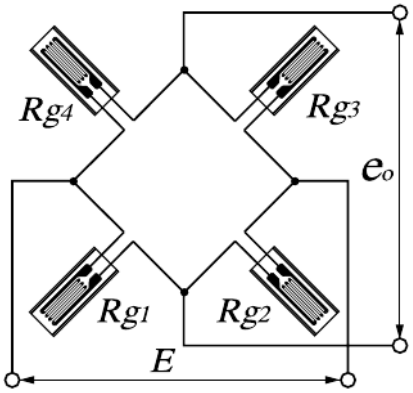

Figure 4.1: The schematic of the strain gauge stations [10]

KYOWA 350Ω foil strain gauges [2] were used on all the polymeric bars, while KYOWA 120Ω foil strain gauges[3] were used on the magnesium bars. Because it was intended to use each of the bars as both an input and transmitter bars all the gauge stations were placed roughly in the centre of the bars. This did mean that if a long duration transmitted pulse occurred there was a chance of reducing the duration of the

[1]The wave speeds presented here are the final calibrated values using viscoelastic correction on all the polymer bars

[2]Product code KFP-2-350-C1-65L1M2R

[3]Product code KFG-2-120-C1-23L1M2R

pulse due to the reflected pulse overlapping at the gauge station.

In addition to the middle gauge station, it was decided that an additional gauge station would be placed 250mm from the front of the Polycarbonate bar. This decision was made in order to investigate the work reported by Martins [48] and Shim [8] who reported that the viscoelastic effects in polycarbonate bars were negligible allowing regular elastic theory to be used to calculate the specimen response.

The gauge stations were amplified through an amplifier designed and built in BISRU labs[4] with a gain of 1000. The signals from these gauge stations were then captured by an ADLINK 9826H data capture card capable of capturing 4 channels of data at 20 MHz.

4.2 Tap tests

Tap tests were performed on each of the polymeric bars to initially establish the general behaviour of each bar and to evaluate the response of each bar to different strikers. The different strikers used were a stainless steel ball bearing, a 10mm diameter 250mm length of nylon, a 10mm diameter 500mm length of nylon and a 16mm diameter 200mm length of magnesium. The ball bearing produced a very short sharp pulse in all the bars which proved difficult to repeat and was therefore discontinued. The most repeatable striker was the 250mm length of nylon which one would expect to produce an almost rectangular pulse. Figures 4.3a 4.3b and 4.3c show the typical results of the tap tests on the different bars at roughly the same striker velocity. The number of different peaks seen in the figures realtes to the different wave speed in the materials which comes form the difference in Young's Modulus and density.

When looking at the results presented, Figure 4.2 explains the different regions of the pulses discussed.

[4]The Circuit diagrams for the amp can be found in the Appendix A

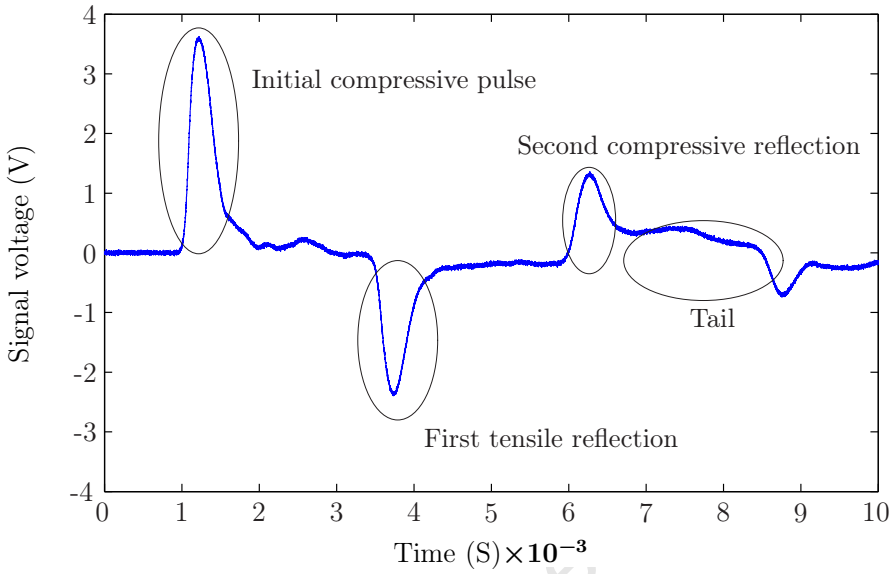

Figure 4.2: A typical Polymeric Hopkinson bar signal from a gauge station

Nylon

The nylon bar shows definite rounding after the initial rise at the top of the initial compressive pulse where one would expect to find a flat plateau seen in Figure 4.3a. The first tensile reflection has definitely decreased in magnitude and dispersion discussed in Section 2.1.1 can be seen influencing the width of the pulse slightly. The top or plateau of the pulse has also changed shape and has no longer got a flat top but rather a defined peak. By the second compressive reflection the change in magnitude and dispersing effects are very marked with a distinct tail developing on the end of the pulse.

The material shows a response expected in a polymeric material with a noticeable dissipation of energy by the material as a pulse propagates down the length of the bar. The noticeable difference in pulse change observed between the initial compressive and first tensile reflection illustrates the material effects on a pressure pulse. It is the correction for this effect that needs to be taken into account in order to accurately make use of this material as a Hopkinson bar.

Polycarbonate

The PC test seen in Figure 4.3b shows very different results to the previous nylon test. Unlike the nylon test the initial compressive pulse has a very rectangular shape with high frequency oscillations on the plateau similar to those seen in metallic Hopkinson bar tests. A tail seems to develop initially but disappears by the first reflection. The tensile reflection seems to show a small change in magnitude but much smaller than that seen in the nylon test which supports the work presented by Shim [8] stating that polycarbonate can be treated as an elastic material when using it in Hopkinson bars. As the pulse propagates down the length of the bar a change in the gross shape can be seen which does bring the linear elastic assumption of Shim into question in Section 2.5.2 .

Polymethyl methacrylate

The PMMA test seen in Figure 4.3c again has a different shape to the other two tests. Instead of the almost rectangular initial PC pulse or the slightly rounded Nylon, the PMMA initial compressive pulse is almost trapezoidal in shape. Keeping in mind that all three tests were performed with the same striker which should nominally produce the same shaped initial pulse, it becomes clear how differently these materials respond. A small amount of high frequency oscillations can be seem at the top of the initial pulse but die down by the time the reflected pulse returns. The gross shape of the pulse changes faster in the PMMA bar becoming almost saw tooth like by the third reflection. It would appear that on first inspection the PMMA has the most marked effect on a pressure pulse which has the most visible changes as the pulse propagates through the material. It should be noted that the general shape of the pulse is the most like that seen in Section 3.3. This in an important point as the model implemented there is a linear viscoelastic one, meaning that the PMMA bar appears to behave in the same fashion.

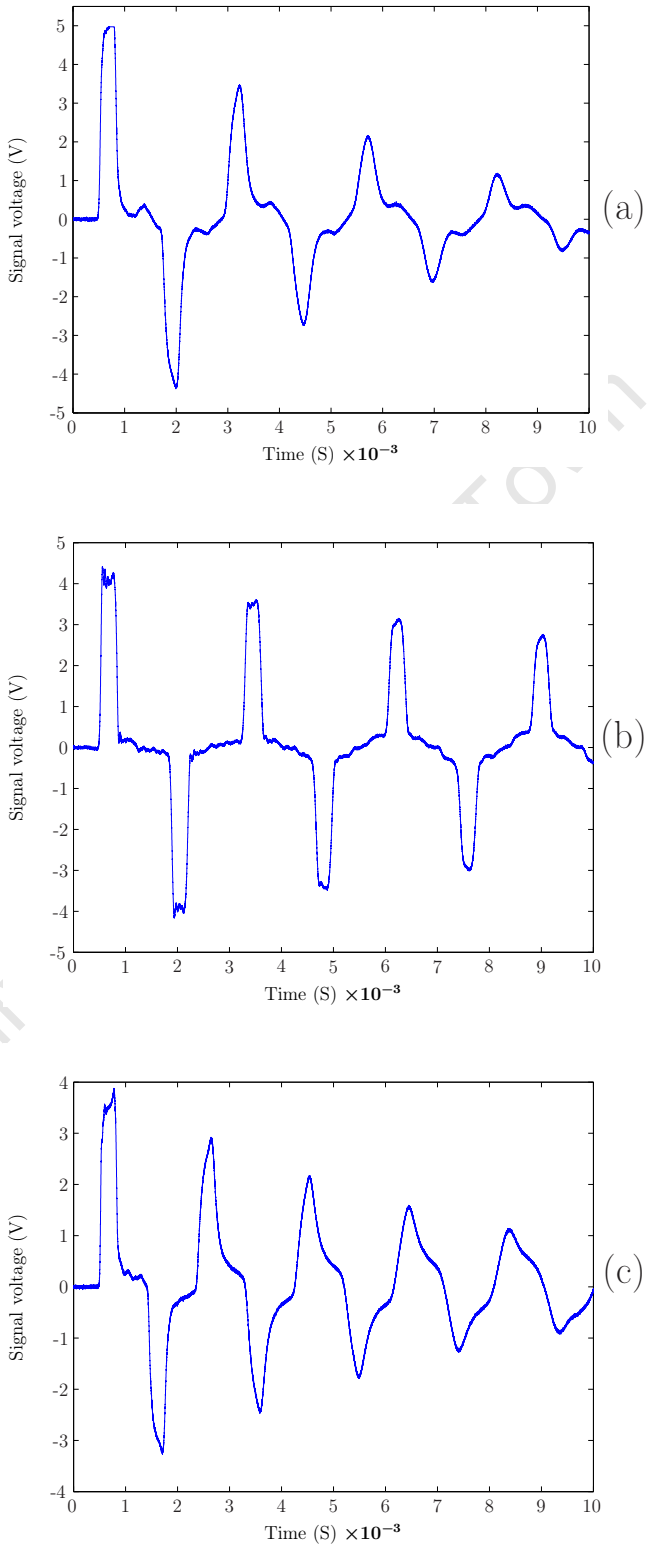

Figure 4.3: The tap tests on the different materials: (a) NYLON (b) PC (c) PMMA.

4.3 Experimental Bar Layout

The bars were set up on BISRU's large gas gun bed in the three basic configurations shown in Figure 4.4. In each of the configurations all three of the polymeric bars were tested. In the work presented by Bacon [2] striker velocities between 0.5 - 5 m/s were used. The lowest striker velocities possible with the current configuration of gas gun and strikers in this work was 3 m/s. As a result the decision was made that tests would be performed with striker velocities in the region of 3 - 15 m/s.

The strikers used are laid out in Table 4.2.

Striker	**Material**	**Diameter (mm)**	**Length (mm)**
Ali 250	Aluminium	16	250
PC 150	Polycarbonate	16	150
PC 300	Polycarbonate	16	300
PC 400	Polycarbonate	16	400

Table 4.2: The different strikers used during the tests

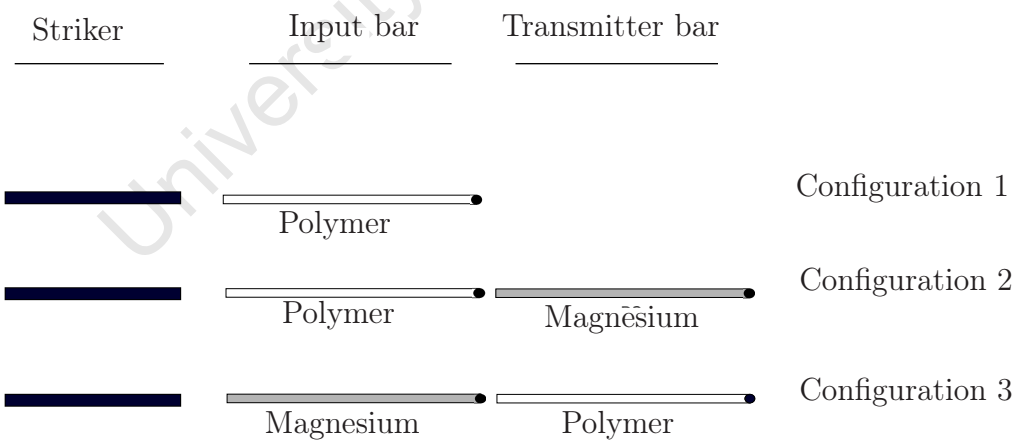

Figure 4.4: The different experimental configurations

The test matrix in Table 4.3 was set up to cover the different configurations for the polymer bars with different strikers in Configuration 1 while trying to figure out how stress waves propagate through the different materials. In each configuration six tests at different velocities are performed.

The test matrix for Configuration 2 can be seen in Table 4.4 where only the PC 150

	Polymer Material		
Striker	NYLON	PC	PMMA
Ali 250 mm	✓	✓	✓
PC 150 mm	✓	✓	✓
PC 300 mm	✓	✓	✓
PC 400 mm	✓	✓	✓

Table 4.3: Test Matrix for Configuration 1.

striker was used as the longer polymer strikers produced a stress wave too long to be captured in the magnesium bar due to the change in wave speed. In each configuration four tests at different striker velocities were performed.

	Polymer Material		
Striker	NYLON	PC	PMMA
PC 150 mm	✓	✓	✓

Table 4.4: Test matrix for Configuration 2.

The test matrix for Configuration 3 can be seen in Table 4.5 where only the MAG 250 striker was used as it produced to most rectanugular pulse in the magnesium bar. In each configuration 4 tests at different striker velocities were performed.

	Polymer Material		
Striker	NYLON	PC	PMMA
MAG 250 mm	✓	✓	✓

Table 4.5: Test matrix for Configuration 3

4.4 Calibration tests

Two different types of calibration were carried out on each of the bars, namely wave speed characterisation and strain gauge calibration. The wave speed calibration allows for accurate prediction of the response of the bars to a pressure pulse. The strain gauge calibration on the other hand allows for the accurate measurement of the response. The bar wave speed is measured first as it is not necessary to have an accurate gauge calibration in order to measure this property which is a time dependent measurement.

4.4.1 Wave speed calibration

Other than the static properties such as density, the wave speed of each bar was first property to be calculated. Each bar was impacted with a striker to produce a pressure pulse which propagates down the bar and through the gauge station, which then reflects off the free end of the bar and passes through the gauge station as a tensile wave. The full signal captured from the calibration of the magnesium bar can be seen in Figure 4.5. This signal is then split into two separate components, namely the incident and reflected pulse. By knowing the distance between the gauge station and the free bar end it is possible to shift each of the two pulses to the interface where they should coincide due to the superposition of waves. [5] This is done using a time shift equal to the time taken in theory for the pulse to travel some distance shown in Equation 4.1

$$\text{Time shift} = \frac{\text{Distance}}{\text{Wavespeed}} \tag{4.1}$$

As an example the results of the shift performed on the magnesium bar can be seen in Figure 4.6 where the two different pulses have been shifted assuming a wave speed of 4968 $\boldsymbol{m/s^{-1}}$ a distance of 0.998 $\boldsymbol{m}$. This is a typical result one would expect for magnesium with the theoretical value from literature being in the region of 4940 $\boldsymbol{m/s^{-1}}$. It is interesting to note that very little dispersion can be seen in this test. This is due to the fact that a small amount of plasticine putty was used to pulse shape the initial compressive pulse. As a result the inital rise time is slightly increased reducing the frequency content and reducing the dispersion effects noted in Section 2.1.1.

When this method is used on polymer bars it is not possible to get a meaningful reading from the material due to the fact that the viscous material effects change the shape of the pressure pulse as it propagates down the bar. This can be clearly seen in

[5] See Section 2.1.1 for an explanation of wave speed and the theory of wave propagation.

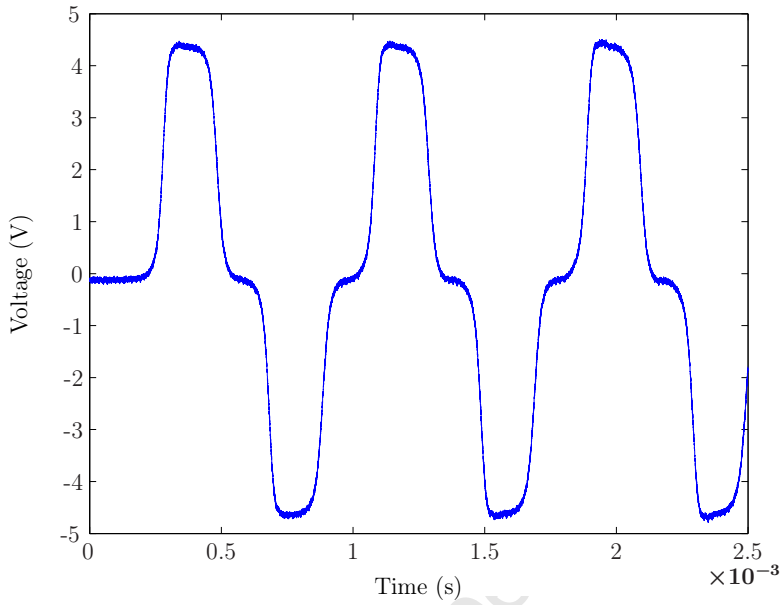

Figure 4.5: The strain gauge signal captured while doing wave speed calibration on the magnesium bar

Figure 4.7 where the conventional approach from the magnesium bar is used without success on a Nylon bar. As can be seen in the figure, the rise on the pulse has changed shape enough to make it very hard to line up and calculate the wave speed. The only way to perform these calculations on polymers would be to first correct for viscoelastic effects of the material. This is covered later on in Chapter 5 where the experimental calibration technique is explained in detail.

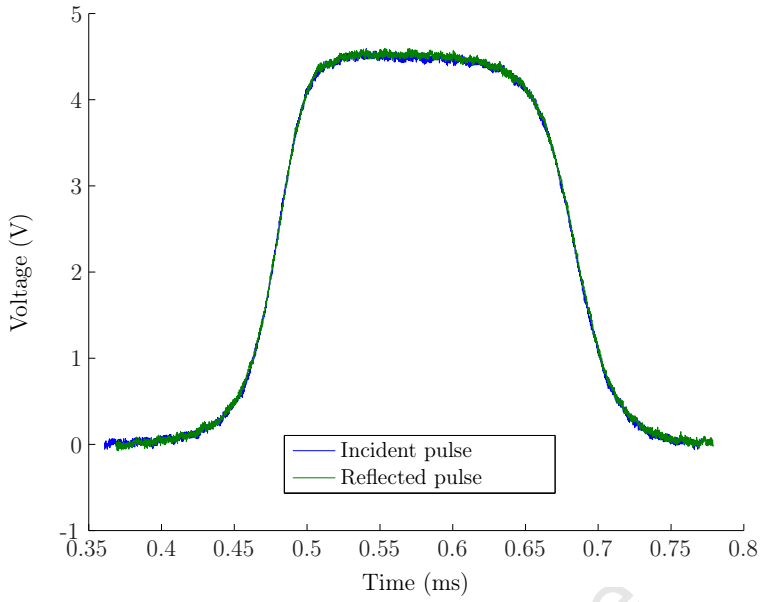

Figure 4.6: The shifted incident and reflected pulses coinciding once the reflected pulse has been inverted and shifted.

4.4.2 Gauge station calibration

There are three main ways to calibrate a strain gauge station. These are

- Theoretical calibration using the amplifier information together with strain gauge theory
- Momentum calibration where the momentum of the striker and the initial pulse are compared
- Maximum stress calibration where the maximum stress in the striker is compared to the initial pulse

It should be noted that the momentum method is not affected by dispersion but is affected by the accuracy of the striker rebound velocity calculation. The maximum stress calculation on the other hand can be affected by dispersion effects.

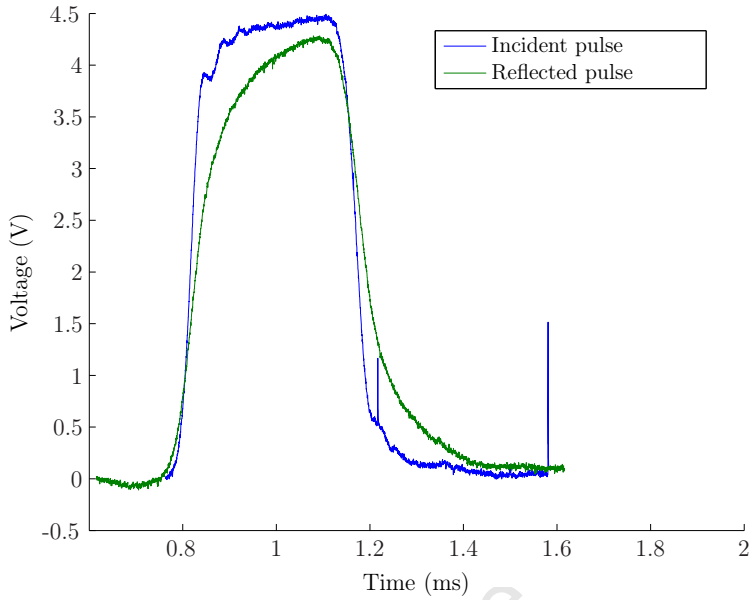

Figure 4.7: Attempted wave speed calculation of nylon using conventional approach

Theoretical Calibration

The output from a strain gauge based on strain gauge theory [57] is

$$\boldsymbol{V_{out}} = \frac{\boldsymbol{K_{gf} N \varepsilon V_{in}}}{\boldsymbol{4}} \tag{4.2}$$

where $\boldsymbol{K_{gf}}$ is the gauge factor, $\boldsymbol{V_{in}}$ is the bridge voltage, $\boldsymbol{\varepsilon}$ is the strain and $\boldsymbol{N}$ is the number of active gauges in the wheatstone bridge.
The input to the amplifier $\boldsymbol{V_{read}}$ is multiplied by the gain in the amp $\boldsymbol{G_{amp}}$ so we can substitute $\boldsymbol{V_{out}} = \frac{\boldsymbol{V_{read}}}{\boldsymbol{G_{amp}}}$. And the strain is related to the stress through the Young's Modulus $\boldsymbol{\varepsilon} = \frac{\boldsymbol{\sigma}}{\boldsymbol{E}}$ resulting in

$$\boldsymbol{\sigma} = \frac{\boldsymbol{4E}}{\boldsymbol{G_{amp} K_{gf} N V_{in}}} \boldsymbol{V_{read}} \tag{4.3}$$

By making the correct substitutions for the values the calibration factor $\boldsymbol{K}$ can then be multiplied by the voltage from the gauge station $\boldsymbol{V_{read}}$ such that

$$\boldsymbol{\sigma} = \boldsymbol{K} \times \boldsymbol{V_{read}} \tag{4.4}$$

Momentum Calibration

Momentum By knowing the momentum of the striker before and after impact with a Hopkinson bar, it is possible to calculate the impulse imparted on the bar. Knowing this impulse it can be compared to the impulse captured by the gauge station and a calibration factor can be calculated.

Firstly in order to calculate the striker's momentum one needs to measure the velocity before and after impact. The initial velocity of the striker is measured using a simple light trap consisting of two beams. The beams are placed 40mm apart in the path of the striker such that when the striker passes through them the beams are broken. The light trap is connected to an oscilloscope which captures the time when each light beam is broken. Knowing the time taken for the striker to travel the 40mm it is possible to calculate the velocity of the striker.

The velocity of the striker after impact can be calculated from the equations in Section 2.1.1. Assuming the areas of the striker and bar are respectively $\boldsymbol{A_s}$ and $\boldsymbol{A_b}$ made from the same material and knowing the measured initial velocity $\boldsymbol{V_0}$, the rebound velocity of the striker $\boldsymbol{V_{reb}}$ becomes

$$\boldsymbol{V_{reb}} = \frac{\boldsymbol{V_0}\left(\frac{\boldsymbol{A_s}}{\boldsymbol{A_b}} - \mathbf{1}\right)}{\left(\mathbf{1} + \frac{\boldsymbol{A_s}}{\boldsymbol{A_b}}\right)} \tag{4.5}$$

Therefore using the difference in velocity before and after impact and knowing the mass of the striker $\boldsymbol{m_{striker}}$, the impulse transferred to the bar during impact $\boldsymbol{I}$ becomes

$$\boldsymbol{I} = \boldsymbol{m_{striker}} \times (\boldsymbol{V_0} - \boldsymbol{V_{reb}}) \tag{4.6}$$

The impulse at any cross-section in the bar is defined as

$$\begin{aligned} \boldsymbol{dI} &= \boldsymbol{F dt} \\ &= \boldsymbol{A_b \sigma dt} \end{aligned} \tag{4.7}$$

Therefore

$$\begin{aligned} \boldsymbol{I} &= \int_{\mathbf{0}}^{\boldsymbol{T}} \boldsymbol{A_b \sigma(t) dt} \\ &= \boldsymbol{A_b} \int_{\mathbf{0}}^{\boldsymbol{T}} \boldsymbol{\sigma dt} \\ &= \boldsymbol{A_b} \int_{\mathbf{0}}^{\boldsymbol{T}} \boldsymbol{K V_{read} dt} \\ &= \boldsymbol{A_b K} \int_{\mathbf{0}}^{\boldsymbol{T}} \boldsymbol{V_{read} dt} \end{aligned} \tag{4.8}$$

So by numerically integrating the voltage from the gauge station to obtain impulse which must be the same as that of the striker yields:

$$K = \frac{I}{A_b \int_0^T V_{read} dt} \tag{4.9}$$

Maximum stress

From Section 2.1.1 we know that the stress in the bar can be found from

$$\sigma_b = \rho C V_b \tag{4.10}$$

From the elementary theory in the same section the velocity of the bar can be calculated similar to Equation 4.5 knowing the initial velocity of the striker V_0 and the areas of the striker and bar respectivley A_s and A_b

$$V_b = \frac{V_0 \left(\frac{A_s}{A_b}\right)}{\left(1 + \frac{A_s}{A_b}\right)} \tag{4.11}$$

Substituting Equation 4.11 into Equation 4.10 yields

$$\sigma_b = \frac{\rho C V_0 \left(\frac{A_s}{A_b}\right)}{\left(1 + \frac{A_s}{A_b}\right)} \tag{4.12}$$

This method is dependant on the pulse produced being almost trapazoidal in shape with a defined plateau which defines an average maximum stress. Now by simply assuming that the average maximum stress in the bar $\sigma_{\text{max b}}$ corresponds to the average maximum voltage reading from the gauge station $V_{\text{max read}}$ the calibration factor becomes

$$K = \frac{\sigma_{\text{max b}}}{V_{\text{max read}}} \tag{4.13}$$

Bar Calibration Results

The Bar calibration results for the Magnesium bar are:

When calibrating the PC, Nylon and PMMA bars only the theoretical calibration can be done without first correcting for the viscoelastic material effects. A complication arose when deciding what Young's Modulus to use to define the materials by as by the nature of viscoelastic materials the Young's Modulus is dependant on the rate of deformation. The decision was taken to use the results of the quasistatic tests performed in Section

	Theoretical (MPa/V)	Momentum (MPa/V)	Max Stress (MPa/V)
Magnesium	5.35	5.11	5.02

Table 4.6: The clibration results for the magnesium bar gauge station

3.2, although this may not be particularly true for the dynamic state the bars will be in during an actual test, it will illustrate very clearly the large difference in calibration factor that will be achieved using an incorrect theoretical value, in comparison to the values achieved using corrected signals later in Chapter 6. For clarity the Gain value is 1000, the gauge factor is 2.05, and the input voltage was kept constant throughout the testing on the polymer bars at 1.4 V.
The theoretical calibration results are:

	Theoretical (MPa/V)	Momentum (MPa/V)	Max Stress (MPa/V)
PC	1.10	NA	NA
Nylon	1.17	NA	NA
PMMA	1.42	NA	NA

Table 4.7: The uncorrected calibration results for the gauge stations on the polymer bars

Once the method for correcting the viscoelastic material effects is presented in Chapter 5, the calibration of the polymeric bars is checked again.

Multiple gauge station calibration

As mentioned previously the PC bar was gauged with two gauge stations seen in Figure 4.8.

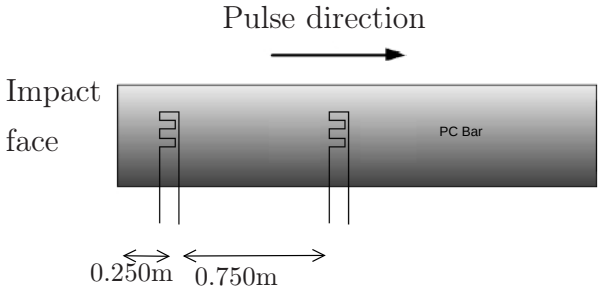

Figure 4.8: The gauge station layout on the PC bar

When the first data from the two gauge stations were plotted together a significant difference between the two stations can be seen in Figure 4.9. As the initial compressive pulse passes the first gauge station the signal is noticeably bigger than when it passes the second gauge station. However as the reflected tensile signal passes the second gauge station for the second time its magnitude remains almost unchanged yet when it reaches the first gauge station it is again larger than the second.

Because no energy was added after the striker impacted the bar it is not possible for a pulse to increase in magnitude when the bar area and material have remained unchanged. This difference observed is due to the slight differences in individual strain gauges resistance. These slight differences cause a visible difference in the output voltage from each of the gauge stations. It is clear that this discrepancy needs to be calibrated in order to correct for the difference. The difficulty in this situation comes in how the calibration factor $\boldsymbol{K_{multi}}$ can be achieved. If the bars were normal metallic bars then a safe assumption would be that dispersion effects between the two stations are minimal and a simple calibration factor could be calculated based on the maximum peaks of each gauge station being the same:

$$\boldsymbol{K_{multi}} = \frac{\text{Gauge station 1 max}}{\text{Gauge station 2 max}}$$

Martins [48] and Shim [8] state that the PC bar can be treated the same way as a metallic bar. However that neglects any effect the viscoelastic material might have had on the pulse, and the purpose of this investigation, and so this assertion will not

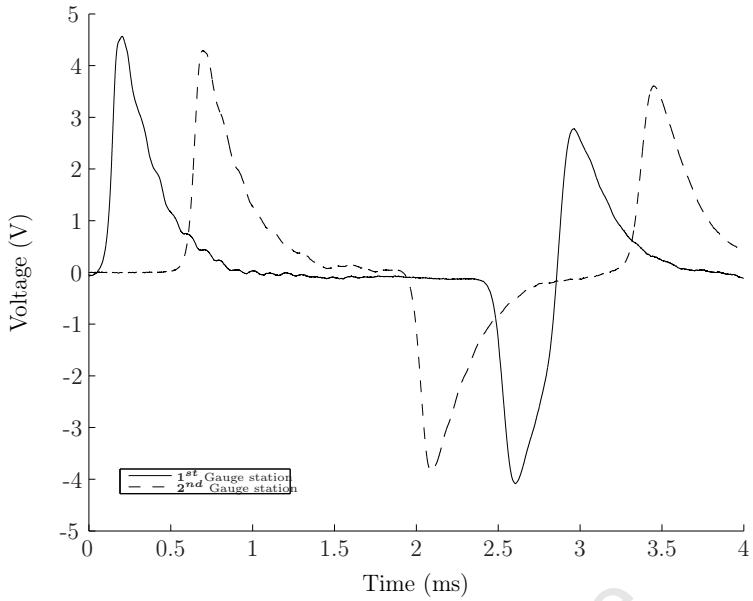

Figure 4.9: The raw data from the double gauge stations on the PC bar

be made. Instead a method of calibration needed to found that did not excite the bars' viscoelastic material response. It was decided to put the entire bar in quasistatic compression. This would mean that because there was no pressure pulse propagation the same uniform compressive strain should be experienced through the length of the bar and at each gauge station. To put the bar in compression it was set up and aligned on the test bed in the bar mounts with rigid stopper on one end and a hydraulic jack on the other. By activating the hydraulic jack the bar could be put in compression. A step loading was used to compress the bar allowing time for the bar to settle between loading increments. Both gauge stations were captured simultaneously and can be seen in Figure 4.10. From the difference in readings of the gauge stations under this quasistatic loading the calibration factor between the gauge stations can be found.

Once the calibration factor achieved from the quasistatic calibration is applied to the signals from the two gauge stations, the magnitudes of the signals become almost the same seen in Figure 4.11. Although these signals appear to be almost the same magnitude a small difference exists when the exact magnitudes are closely interrogated.

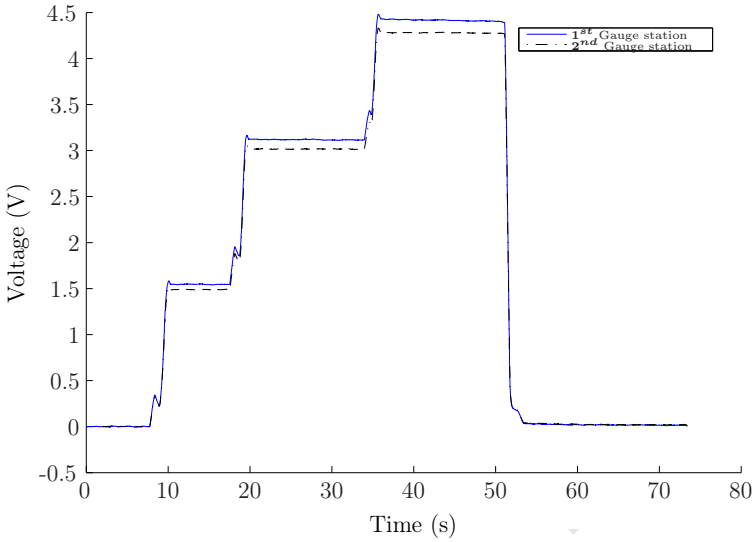

Figure 4.10: Quasistatic calibration of PC bar gauge stations

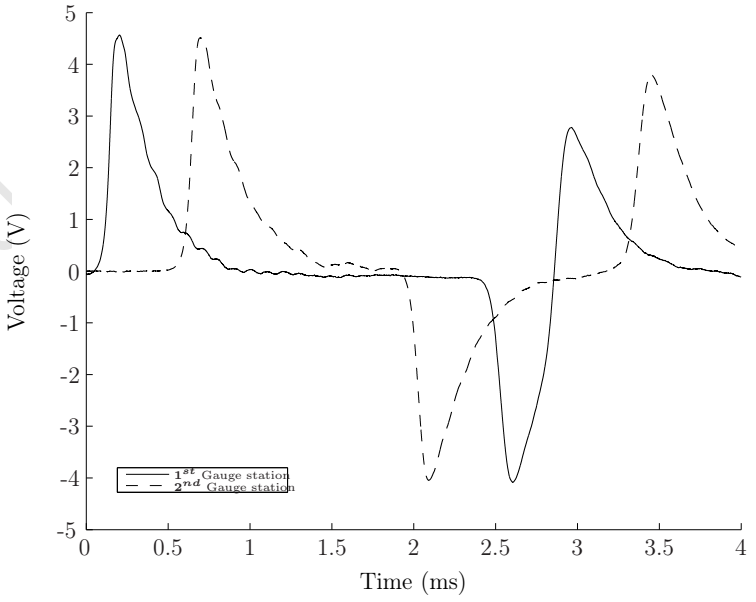

Figure 4.11: The corrected data from the double gauge stations on the PC bar

Chapter 5

Data Processing

The purpose of this chapter is to describe the techniques used to interpret the experimental data acquired in testing the different bar materials. The requirement to characterise the viscoelastic material behaviour of a polymeric Hopkinson bar has previously been established in Chapter 4.This is required in order to use the polymeric split Hopkinson bar technique to characterise low impedance specimens. This chapter firstly deals with the theory of the technique and then moves on to discuss the transfer function $\gamma(\omega)$ which characterises how stress pulses move through viscoelastic Hopkinson bars. The results of using this method are presented later in Chapter 6.

5.1 Theory

The method chosen to characterise the viscoelastic wave propagation in this dissertation is Bacon's method as discussed in Section 2.4.4. This specific method was chosen due to the fact that the material is characterised experimentally in a very straight forward way which lends itself to routine calibration. It is important because it means that with a few simple calibration tests, before testing specimens, a transfer function for the bars under almost the same conditions as those to be expected during testing can be derived. In contrast, some of the other methods require at least one analytical component to be used, some requiring significant computational effort to derive a property that is assumed to remain constant. Changes in temperature, for instance, have an effect on these properties which is difficult to characterise in an absolute sense.

As mentioned in Section 2.4.4, this method describes viscoelastic material response

with a complex modulus $\boldsymbol{E^*(\omega)}$ which relates the stress and strain at any point.

$$\tilde{\boldsymbol{\sigma}}(\boldsymbol{x},\boldsymbol{\omega}) = \boldsymbol{E^*(\omega)}\tilde{\boldsymbol{\varepsilon}}(\boldsymbol{x},\boldsymbol{\omega}) \tag{5.1}$$

The central feature of this method is the propagation coefficient $\boldsymbol{\gamma = \gamma(\omega)}$ which is defined by

$$\boldsymbol{\gamma^2(\omega)} = -\frac{\boldsymbol{\rho\omega^2}}{\boldsymbol{E^*(\omega)}} \tag{5.2}$$

The general solution to the one dimensional equation of motion becomes:

$$\tilde{\boldsymbol{\varepsilon}}(\boldsymbol{x},\boldsymbol{\omega}) = \tilde{\boldsymbol{P}}(\boldsymbol{\omega})\boldsymbol{e}^{-\boldsymbol{\gamma x}} + \tilde{\boldsymbol{N}}(\boldsymbol{\omega})\boldsymbol{e}^{\boldsymbol{\gamma x}} \tag{5.3}$$

where the functions $\tilde{\boldsymbol{P}}(\boldsymbol{\omega})$ and $\tilde{\boldsymbol{N}}(\boldsymbol{\omega})$ define the strains at $\boldsymbol{x = 0}$ to waves travelling in directions of increasing and decreasing $\boldsymbol{x}$ respectively. From these it is possible to find the Fourier transform of the particle velocity $\tilde{\boldsymbol{v}}(\boldsymbol{x},\boldsymbol{\omega})$ and the normal force $\tilde{\boldsymbol{F}}(\boldsymbol{x},\boldsymbol{\omega})$ at any cross section $\boldsymbol{x}$.

$$\begin{aligned}
\tilde{\boldsymbol{v}}(\boldsymbol{x},\boldsymbol{\omega}) &= -\frac{\boldsymbol{i\omega}}{\boldsymbol{\gamma}}\left[\tilde{\boldsymbol{P}}(\boldsymbol{\omega})\boldsymbol{e}^{\boldsymbol{\gamma x}} - \tilde{\boldsymbol{N}}(\boldsymbol{\omega})\boldsymbol{e}^{\boldsymbol{\gamma x}}\right] \\
\tilde{\boldsymbol{F}}(\boldsymbol{x},\boldsymbol{\omega}) &= -\frac{\boldsymbol{\rho A\omega^2}}{\boldsymbol{\gamma^2}}\left[\tilde{\boldsymbol{P}}(\boldsymbol{\omega})\boldsymbol{e}^{\boldsymbol{\gamma x}} + \tilde{\boldsymbol{N}}(\boldsymbol{\omega})\boldsymbol{e}^{\boldsymbol{\gamma x}}\right]
\end{aligned} \tag{5.4}$$

The modulus and phase angle of the complex exponential functions $\boldsymbol{e}^{-\boldsymbol{\gamma x}}$ and $\boldsymbol{e}^{\boldsymbol{\gamma x}}$ are related to attenuation and propagation respectively. Thus the propagation coefficient $\boldsymbol{\gamma(\omega)}$ is connected to the attenuation coefficient (or damping) $\boldsymbol{\alpha(\omega)}$ and to the phase velocity $\boldsymbol{c(\omega)}$ by

$$\boldsymbol{\gamma(\omega)} = \boldsymbol{\alpha(\omega)} + \boldsymbol{ik(\omega)} = \boldsymbol{\alpha(\omega)} + \boldsymbol{i}\frac{\boldsymbol{\omega}}{\boldsymbol{C(\omega)}} \tag{5.5}$$

where $\boldsymbol{k(\omega)}$ is the wave number defined by

$$\boldsymbol{k} = -\frac{\boldsymbol{(\Theta_R) - (\Theta_I)}}{\boldsymbol{d}} \tag{5.6}$$

. Where $\boldsymbol{\Theta_R}$ and $\boldsymbol{\Theta_I}$ are the unwrapped phase angles of the two complex functions $\tilde{\boldsymbol{P}}(\boldsymbol{\omega})$ and $\tilde{\boldsymbol{N}}(\boldsymbol{\omega})$. So by finding $\boldsymbol{\alpha}$ along with either $\boldsymbol{k}$ or $\boldsymbol{c}$ the propagation coefficient can be described.

The following properties of these different functions should be noted:

- The Wave number $\boldsymbol{k}$ is an odd function
- Phase velocity $\boldsymbol{C}$ is an even function

- The Modulus and attenuation coefficient are even functions

In the work presented by Bacon [2], it is noted that the frequency range of importance while characterising polymeric materials is from 0 - 20 kHz. Above this point the frequency content becomes negligible as the high frequencies get damped out in the material. This results in excessive numerically induced noise as a result of division by very small numbers in the calculation of different components. For this reason the region that is highlighted in this work and presented in the following sections is from 0 - 20 kHz, although some content above this point is shown for completeness in Section 6

5.2 Deriving the Propagation coefficient

The propagation coefficient γ describes the changes that occur to a stress pulse that travels some distance through a viscoelastic material. When a stress pulse can be measured at two different positions in a Hopkinson bar, then the changes that occur to the pulse between these two points are assumed to be attributable to γ. There are two ways of achieving this;

- Having two gauge stations separated by some distance on a Hopkinson bar seen in Figure 4.8 and capturing the data from both. By comparing the two different signals the differences can be calculated.
- Using the reflection of a stress wave off a free end of the bar as discussed in Section 2.1.1. This method requires taking the information from a single gauge station and separating the initial compressive pulse from the tensile reflection so that they can be compared in order to calculate γ.

The differences in the two gauge station setup on the PC bar discussed in Section 4.4.2 make it a more complicated approach to take. The purpose of this investigation is to illustrate the differences in the bar materials and the single gauge station will be sufficient for a comparison to be drawn.

In order to implement Bacon's method a set procedure needs to be followed. This procedure can be seen in Figure 5.1 which shows a flow chart representation of the method. In order to clarify the process the example of a signal captured on the PC bar is used. The bar was impacted with a PC striker 400mm in length with a diameter of 15.90 mm at a velocity of 11 m/s and the signal is shown in Figure 5.2.

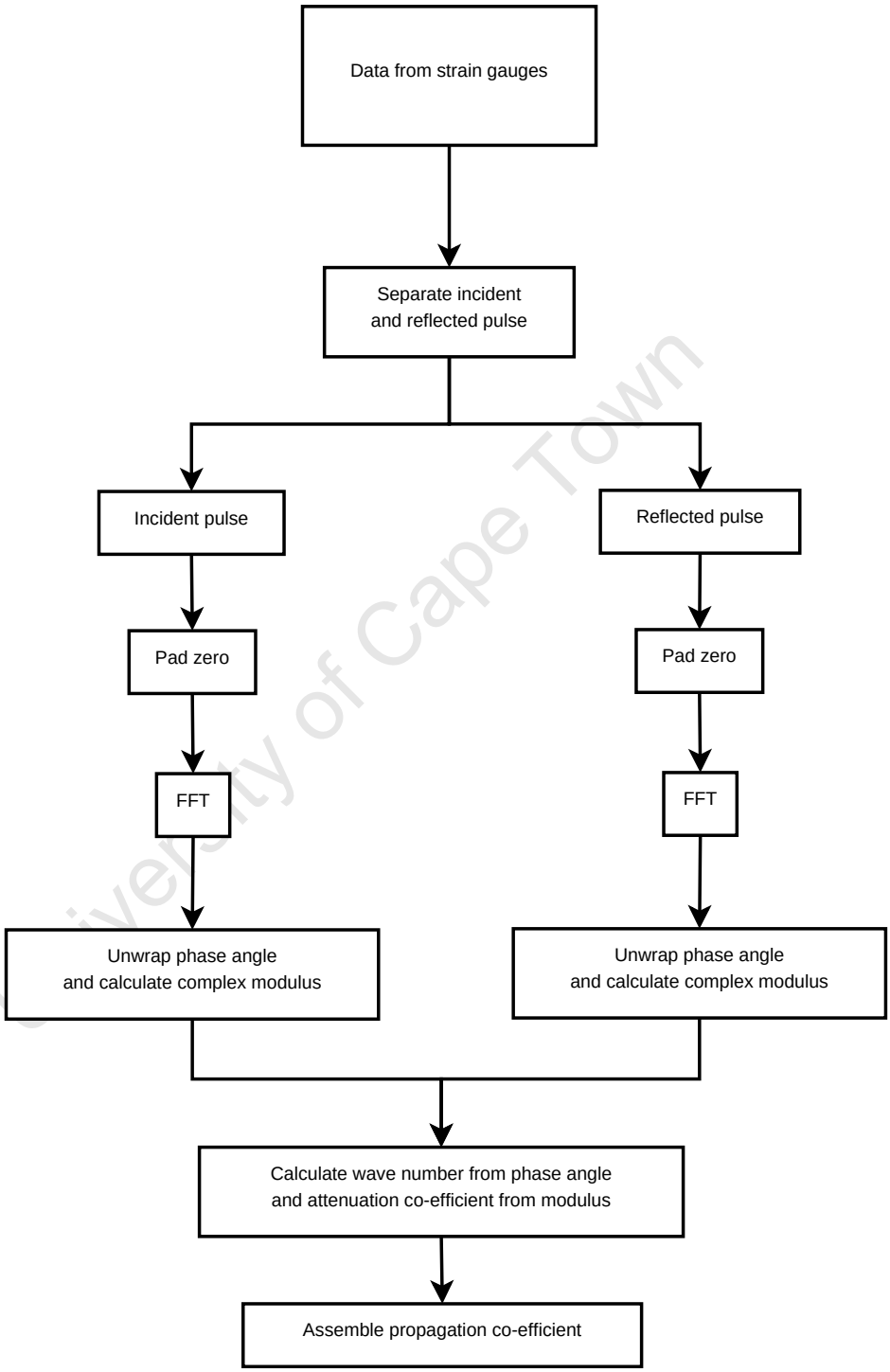

Figure 5.1: Flow chart showing the procedure followed when obtaining the propagation coefficient.

The first process is to window or separate the incident and reflected pulses. Each window must contain all the pertinent information from the instant when the pulse starts to deviate from the mean zero to the time when the pulse settles back to the mean zero. An example is shown in Figure 5.3. Note that the full length of the signal is maintained and the data outside the area of interest is simply set to zero. From this point on the incident pulse is a separate signal to the tensile reflection. Once each pulse has been separated and data set to zero where appropriate, the FFT function is used to transfer them to the frequency domain. This is used together with a variable called "NFFT" which defines the length of the FFT vector to optimise the speed of the function. When the length of the vector is a power of two , ie: $\boldsymbol{2^b}$ where $\boldsymbol{b}$ is some positive integer, then the functions speed is optimised. This is achieved by finding the next largest number to the length of the windowed vector which can be written as $\boldsymbol{NFFT = 2^b}$. The result of the FFT function is a complex number. Using Equation 2.24 from Section 2.2.1 is is possible to interrogate the magnitude and phase of this number. In Section 2.2.1 it was noted that the FFT of a signal produces both a positive and negative frequency spectrum. Because this is mirrored around a zero frequency only the positive side will be shown.

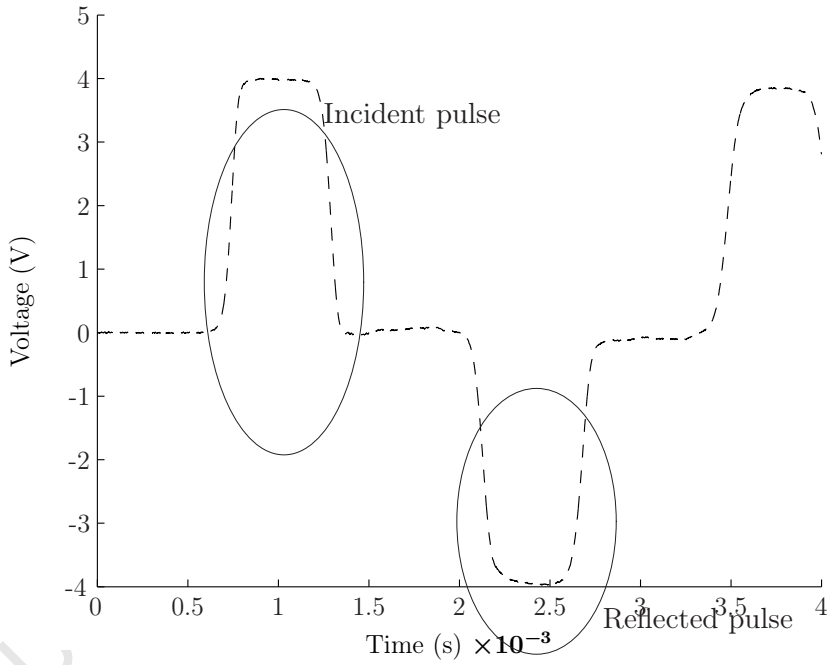

Figure 5.2: The raw signal output from PC bar impacted with 400 mm PC striker

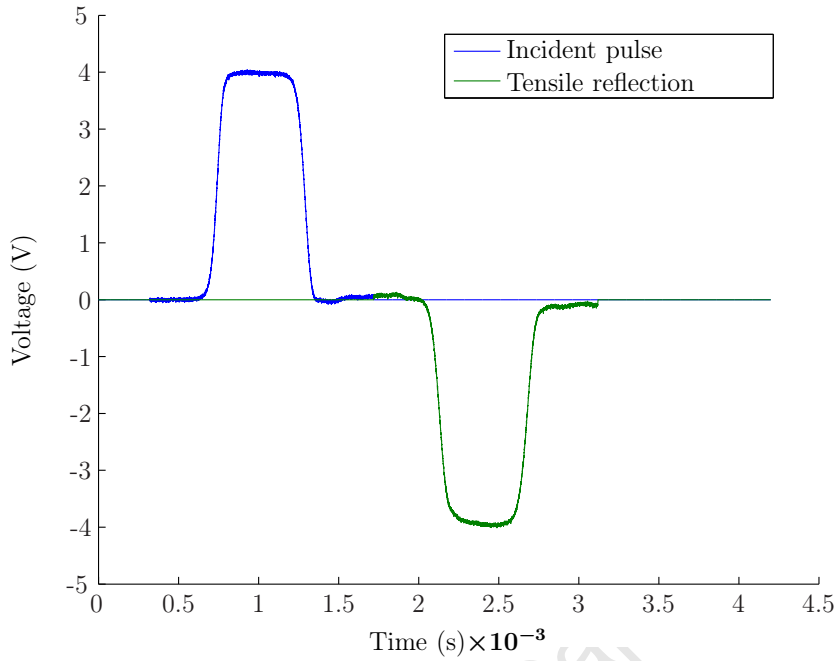

Figure 5.3: The raw signal output from PC bar impacted with 400 mm PC striker

5.2.1 Magnitude

The magnitude or modulus of the complex number that results from the FFT can be seen in Figure 5.4. A difference can be seen in the modulus of both the incident and reflected pulses. Additionally the magnitude dies down to almost zero by about 14 KHz and remains that way right up to 5 MHz at the end of the frequency spectrum. The difference between these two pulses is considered to represent the "attenuation" of the pulse. This is a result of the pulse having travelled down the bar and reflected off the free end and returned to the gauge station, travelling a total distance of 2.016 m.

The difference between the two magnitudes is defined as an attenuation ratio

$$\boldsymbol{Attenuation\ Ratio} = \frac{|\boldsymbol{FFT\ Reflected\ pulse}|}{|\boldsymbol{FFT\ Incident\ pulse}|} \tag{5.7}$$

or in the polar notation from Section 2.2.1:

$$\boldsymbol{Attenuation\ Ratio} = \frac{\boldsymbol{r_R}}{\boldsymbol{r_I}} \tag{5.8}$$

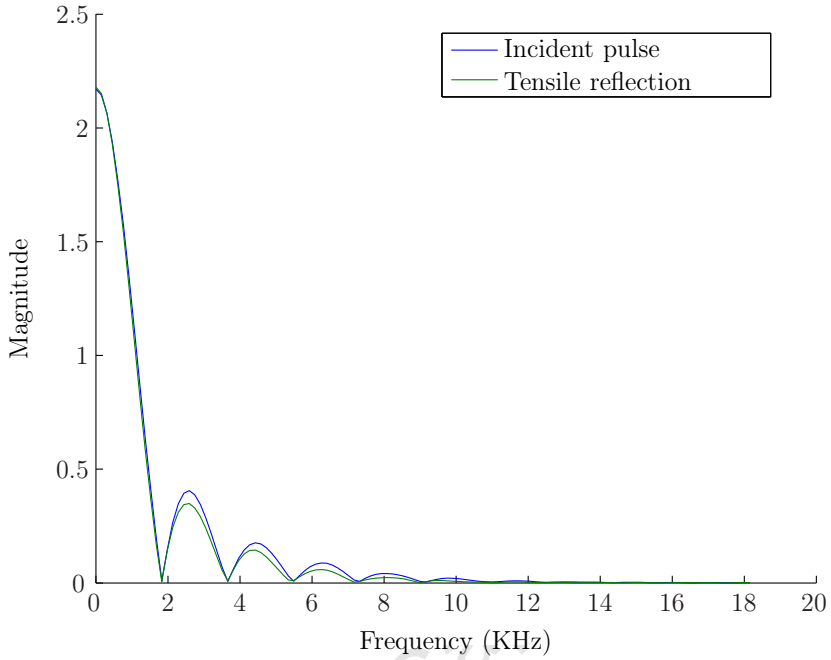

Figure 5.4: The modulus of the first compressive and tensile reflection pulses in the frequency domain.

5.2.2 Attenuation Co-efficient

The Attenuation coefficient $\boldsymbol{\alpha}$ is defined as:

$$\boldsymbol{\alpha} = -\frac{\boldsymbol{ln}\left(\frac{\boldsymbol{r_R}}{\boldsymbol{r_I}}\right)}{\boldsymbol{x}} \tag{5.9}$$

Where $\boldsymbol{r_R}$ and $\boldsymbol{r_I}$ are the modulus of the reflected and incident pulses in the frequency domain respectively, $\boldsymbol{x}$ is the distance through which the pulse has propagated. It is important to note that this is an even function in the frequency domain and defines the real part of the transfer function $\boldsymbol{\gamma}$. An example of the attenuation coefficient is shown in Figure 5.5.

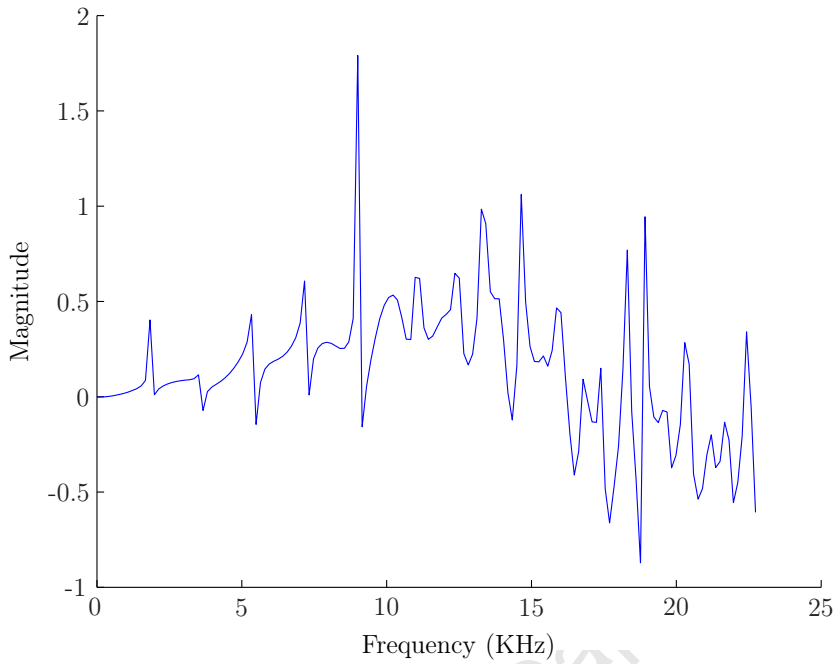

Figure 5.5: The attenuation coefficient for PC in the frequency domain.

5.2.3 Phase angle

The phase angle of the complex number that comes from the FFT it may not initially look sensible as seen in Figure 5.6. The angle oscillates between π and $-\pi$. To make sense of this an operation called "unwrapping" needs to be performed on the phase angle to account for the jumps from π to $-\pi$. This involves adding or subtracting π depending on the jump that occurs.

The unwrapped phase angle Θ can be seen in Figure 5.7. A noticeable difference can now be seen as the phase angle changes between the compressive and tensile pulses and a trend emerges. The difference between the two phase angles is defined as :

$$\text{Change in phase angle} = (\Theta_R) - (\Theta_I) \tag{5.10}$$

where Θ_I and Θ_R are the phase angle of the incident and reflected pulses respectively.

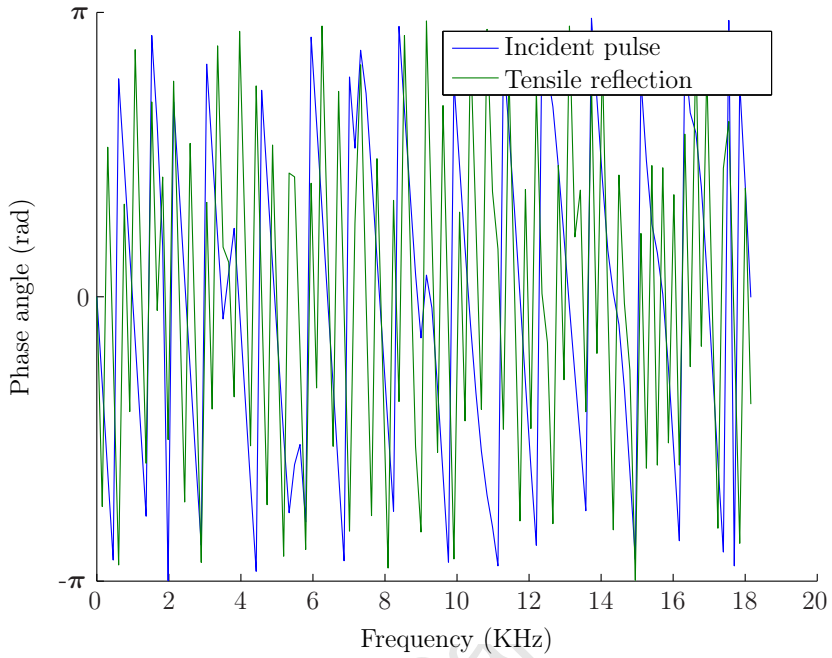

Figure 5.6: The phase angle of the first compressive and tensile reflection pulses in the frequency domain.

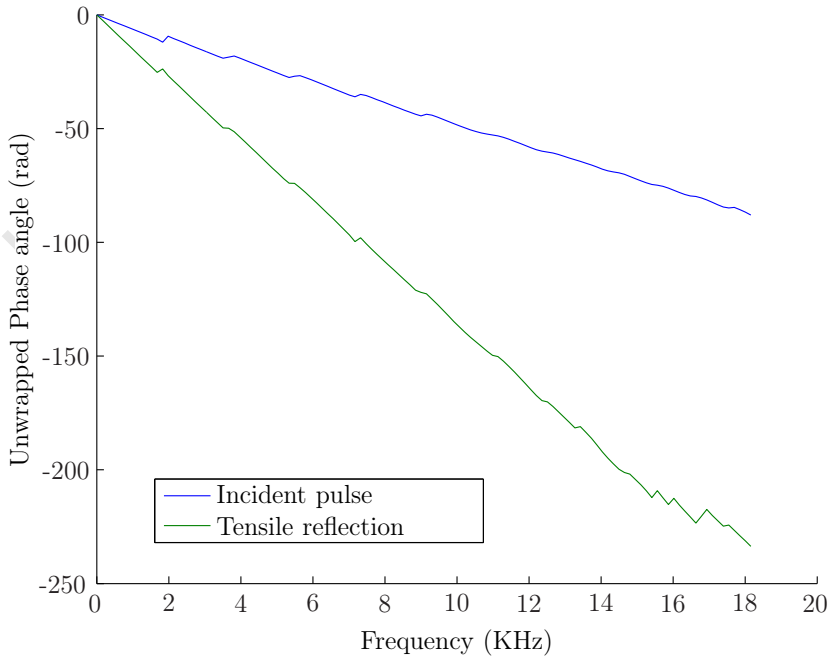

Figure 5.7: The Unwrapped phase angle of the first compressive and tensile reflection pulses in the frequency domain.

5.2.4 Wave number

The wave number $\boldsymbol{k}$ is defined as:

$$\boldsymbol{k} = -\frac{(\boldsymbol{\Theta_R}) - (\boldsymbol{\Theta_I})}{\boldsymbol{x}} \tag{5.11}$$

where $(\boldsymbol{\Theta_R}) - (\boldsymbol{\Theta_I})$ is the change in phase angle and $\boldsymbol{x}$ is the distance through which the pulse has propagated. An example of the wave number is shown in Figure 5.8.

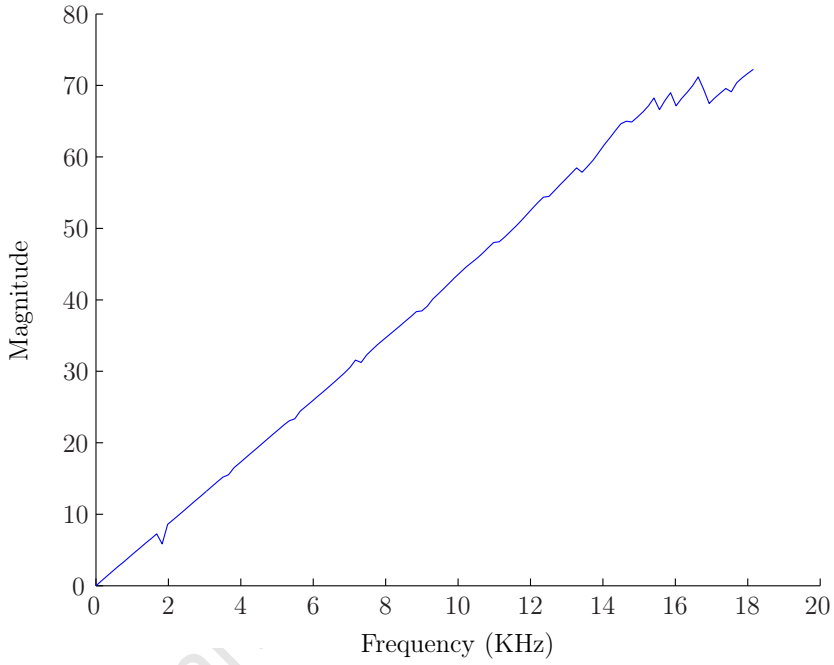

Figure 5.8: The wavenumber for PC in the frequency domain.

It is important to note that the wave number is an odd function in the frequency domain, and comprises the imaginary component of the transfer function $\boldsymbol{\gamma}$.

5.2.5 Phase velocity

The Phase velocity can be derived from the wave number $\boldsymbol{k}$ as follows:

$$\boldsymbol{C(\omega)} = \frac{\boldsymbol{\omega}}{\boldsymbol{k(\omega)}} \tag{5.12}$$

where $\boldsymbol{\omega}$ is the frequency. The phase velocity is an even function in the frequency domain and an example can be seen in Figure 5.9.

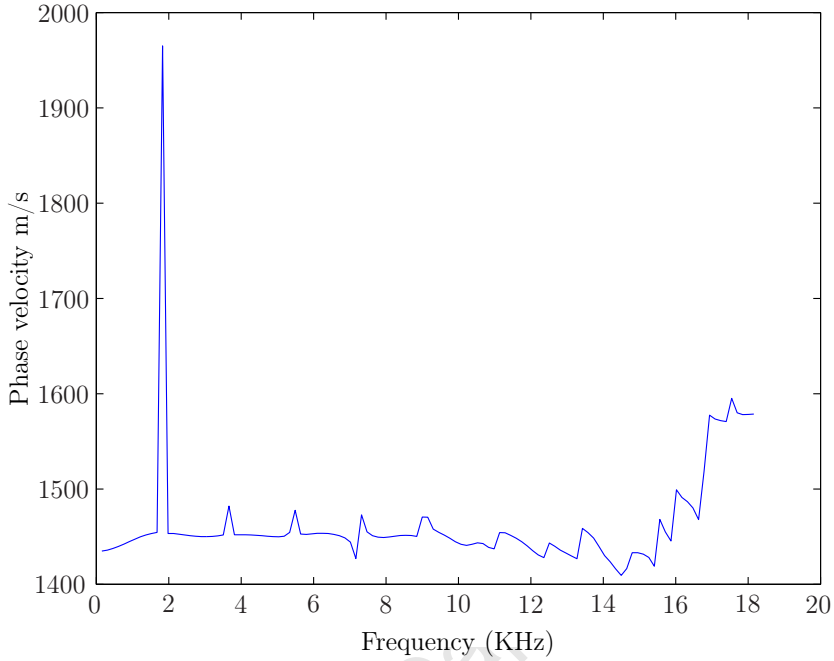

Figure 5.9: The phase velocity for PC in the frequency domain.

5.2.6 Propagation coefficient

From the attenuation coefficient $\boldsymbol{\alpha}$ and the wave number $\boldsymbol{k}$ the transfer function $\boldsymbol{\gamma}$ can be written as:

$$\boldsymbol{\gamma(\omega) = \alpha(\omega) + ik(\omega)} \tag{5.13}$$

In order to shift some arbitrary pulse $\boldsymbol{P}$ up or down a bar the transfer function is multiplied by the distance $\boldsymbol{d}$ of the shift and applied in the frequency domain as follows:

$$\boldsymbol{P_{shift} = Pe^{\gamma x}} \tag{5.14}$$

Once the shift has been applied then the pulse in the frequency domain is transferred to the time domain using the Inverse Fast Fourier Transform (IFFT). In Figure 5.10 the incident pulse and the tensile reflection have both been shifted to the free end of the bar where they should sum to the zero force boundary condition at the free surface. When shifting both these pulses in a bar to a common interface, one would expect them coincide. The fact that they do is regarded as confirmation that the method is working.

5.3 SHIFTING PULSES IN POLYMER BARS

A short description of how the propagation coefficient, derived in the previous section, is applied to shifting pulses is described here. The term "shifting" is used here to describe the process of taking a signal or pulse captured at a gauge station on a Hopkinson bar, and predicting what that pulse would be if it had been captured at some position which is either $\boldsymbol{x}$ m from the gauge station in the same direction as the wave is propagating, or $-\boldsymbol{x}$ m in the opposite direction.

The pulse of interest is firstly selected from the remainder of the data in the same fashion as described in Section 5.2. After the pulse has been separated and the remainder of the data set to zero, the signal is transformed into the frequency domain by means of the FFT function in the same manner as described in Section 5.2 where the use of the FFT is described.

$$\varepsilon(t) \Rightarrow \boldsymbol{FFT} \Rightarrow \widetilde{\varepsilon}(\omega)$$

What exists at this point is a frequency domain representation of the strain $\widetilde{\varepsilon}(\omega)$. At this point the propagation coefficient $\gamma(\omega)$ can be applied to shift the pulse through some linear distance $\boldsymbol{x}$ from the gauge station as shown in:

$$\widetilde{\varepsilon_{shift}}(\omega) = \widetilde{\varepsilon}(\omega)e^{\gamma x} \tag{5.15}$$

At this point the shifted pulse like the unshifted one is frequency dependant and the inverse Fourier transform must be used to transfer the signal back to the time domain where regular Hopkinson bar theory can be applied.

$$\widetilde{\varepsilon_{shift}}(\omega) \Rightarrow \boldsymbol{IFFT} \Rightarrow \varepsilon_{shift}(t)$$

The result of a shift performed on a PC bar signal using the propagation coefficient derived in Section 5.2.6 is used to shift two pulses in the bar. The first pulse that was shifted was the incident pulse which is shifted through a distance of 1 m to the free end of the bar. The second shift which can be seen is the shift of the tensile reflection pulse which is shifted through a distance of -1 m to the same free end of the bar as the incident pulse is. At this point, by the principle of superposition, the two strain pulses should be the same.

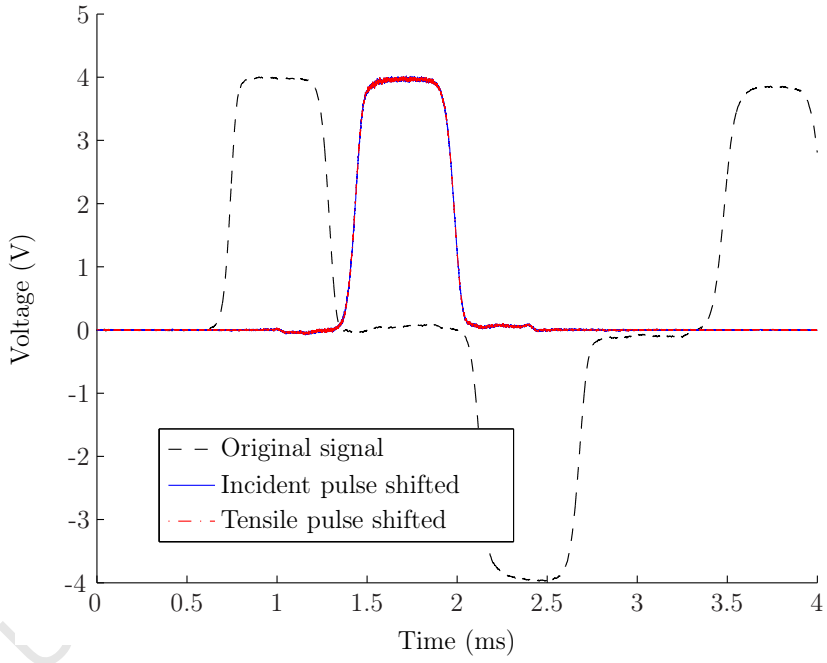

Figure 5.10: The incident and reflected pulses shifted back to the free interface.

Chapter 6

Results

The purpose of this chapter is to present the results obtained in testing each of the different bar materials. Each bar configuration is presented separately in its own section. The configurations mentioned here are the same as those set out in Section 4.3 where the proposed testing can be seen. The results for the polymer bars in configuration 1 are presented first. This section involves only the polymer bars and the purpose of these tests is to define a propagation coefficient for each bar. The properties highlighted in Section 5.2 are presented for each bar material in developing a propagation coefficient for each bar. At the end of this section the results of tests for the propagation coefficient used are presented.

In configuration 2 the magnesium bar is placed at the end of the polymer bars. This configuration confirms the use of superposition and shifting in the polymer bars as the magnesium bar provides a reliable force measurement at the interface of the two bars.

In configuration 3 the magnesium bar is placed in front of the polymer bars. This configuration tests the polymer bars as output bars in SHPB testing. The magnesium bar is again used as a reliable force measurement at the interface of the bars.

6.1 Configuration 1 - Polymer bars

The results presented here are the results of the different material calibration tests performed on the NYLON bar. These involved using the different strikers mentioned in Section 4.3 to impact the bar at velocities in the region of 3 - 15 m/s. The results are presented as a single cloud incorporating the data from all the tests.

6.1.1 NYLON

In Figure 6.1 the attenuation coefficients for all the tests are plotted together. The data in the region of 0 - 10 kHz is tightly grouped indicating a definite trend developing for the bar. In the region of 10 - 15 kHz the data becomes more scattered although a distinct trend is still discernible. From 15 kHz the data has scattered although it does remain in a loosely bounded group. There are a few data point which can be seen below the zero line indicating a negative attenuation coefficient. These data points together with the asymptotes are a result of numerical error. The attenuation coefficient involves the Log of a magnitude ratio with division of very small numbers where the numerator can be larger than the denominator, causing these discontinuities.

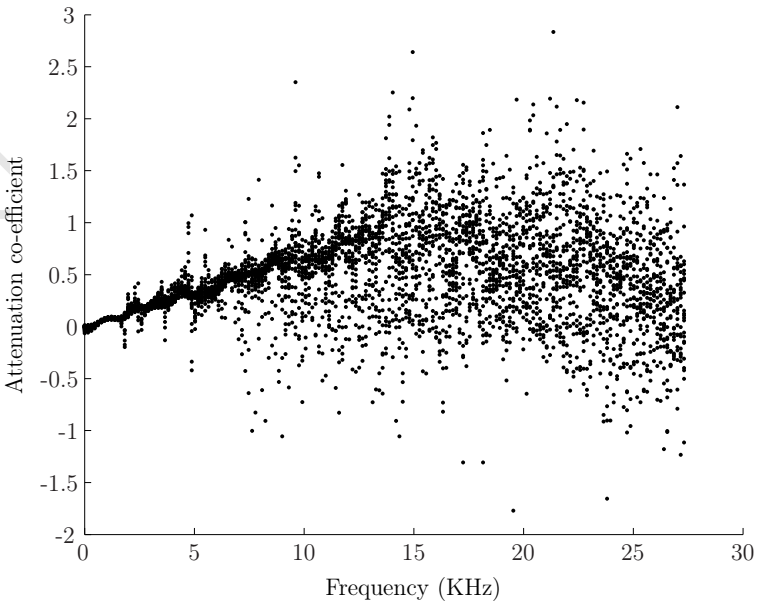

Figure 6.1: A cloud of data showing the spread in Attenuation coefficient for NYLON.

In Figure 6.2 the wave number of all the different tests is presented. From 0 - 10 kHz a very well defined linear trend can be seen. Between 10 - 15 kHz some data point start to deviate from this trend. In the region of 20 kHz the data seems to deviate from the initial linear trend, but still remains linear. A general bilinear response of the wave number is evident for this NYLON bar.

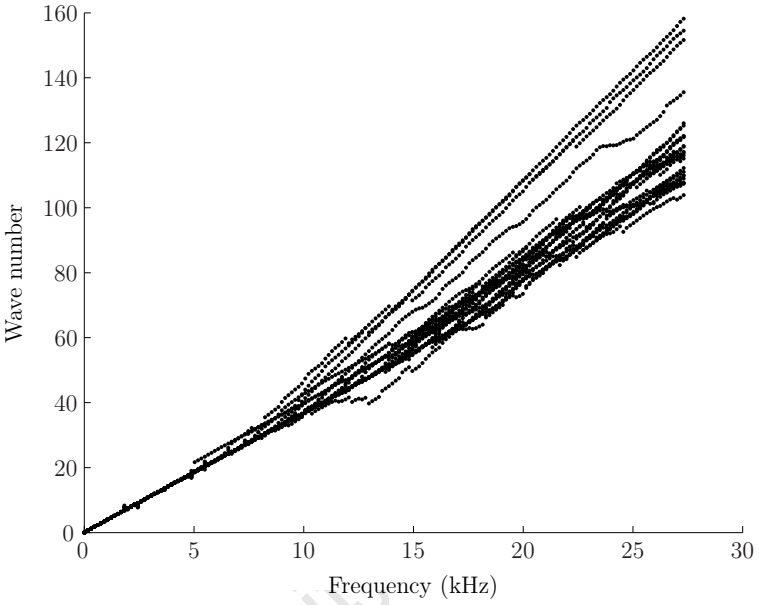

Figure 6.2: A cloud of data showing the spread in Wave number for NYLON.

In Figure 6.3 the phase velocity for the NYLON tests is presented. In this data a trend can be seen developing up to 15 kHz where the trend has formed what appears to be a plateau. Above 15 kHz the data spreads out but remains in a loosely bounded group with a downward trend.

In order to choose a suitable propagation coefficient for the bar, the attenuation coefficient and wave number functions that most closely match the trends seen in Figure 6.1 and 6.2 were used. These were combined according to Equation 5.13 to describe the propagation coefficient. This propagation coefficient is then used on a pulse from the NYLON bar that was recorded for an extended duration capturing multiple reflections in the bar. The incident pulse in Figure 6.4 is selected and the propagation coefficient is applied to it as outlined in Section 5.3. The shifting is applied in such a way that the shifted pulses should coincide with the reflected pulses in the bar. The results for the

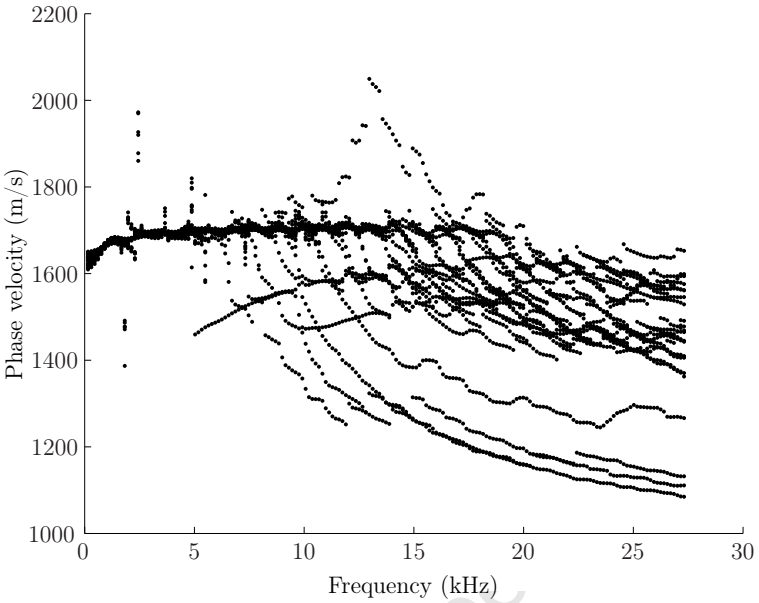

Figure 6.3: A cloud of data showing the spread in Phase velocity for NYLON.

first four reflections in the bar are presented and as can be seen they coincide well with the actual data recorded at the gauge station.

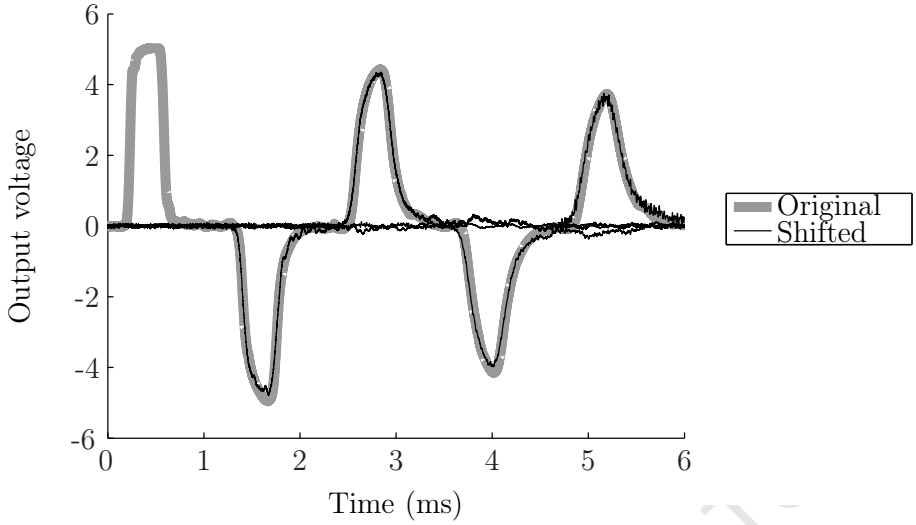

Figure 6.4: The propagation coefficient applied to a NYLON signal and shifted over different distances.

6.1.2 PMMA

In Figure 6.5 the attenuation coefficient for the tests on the the PMMA bar are presented together. A similar trend to that of the NYLON bar is observed in that up to 10 kHz the data is tightly grouped to form a trend. Between 10 - 20 kHz the data starts to spread slightly although a trend can still be seen. Above 20 kHz the data scatters although a loosely bounded trend appears to continue in the same fashion as that established in the lower frequency range. Once again there are a few data point which can be seen below the zero line indicating a negative attenuation coefficient. These data points together with the asymptotes are a result of the numerical error described previously.

In Figure 6.6 the wave number for the tests performed on the PMMA bar are presented. These results appear differently to the NYLON bar. Up to 20 kHz a very strong linear trend can be seen. Above 20 kHz the strong linear trend remains with some of the data points deviating from this.

In Figure 6.7 the phase velocity for the PMMA bar is presented. In this case the data remains tightly grouped up to a frequency of 25 kHz by which time the trend appears to have formed a plateau.

In order to choose a suitable propagation coefficient for the bar, the attenuation coefficient and wave number functions that most closely match the trends seen in Figure

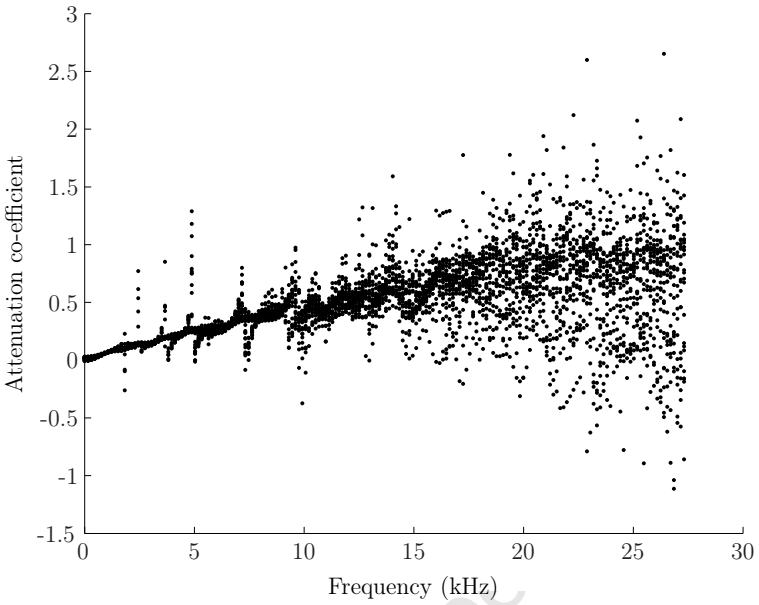

Figure 6.5: A cloud of data showing the spread in Attenuation coefficient for PMMA.

6.5 and 6.6 were used. These were combined according to Equation 5.13 to describe the propagation coefficient. This propagation coefficient is then used on a pulse from the PMMA bar that was recorded for an extended duration capturing multiple reflections in the bar. The incident pulse in Figure 6.8 is selected and the propagation coefficient is applied to it as outlined in Section 5.3. The shifting is applied in such a way that the shifted pulses should coincide with the reflected pulses in the bar. The results for the first four reflections in the bar are presented and as can be seen they coincide well with the actual data recorded at the gauge station.

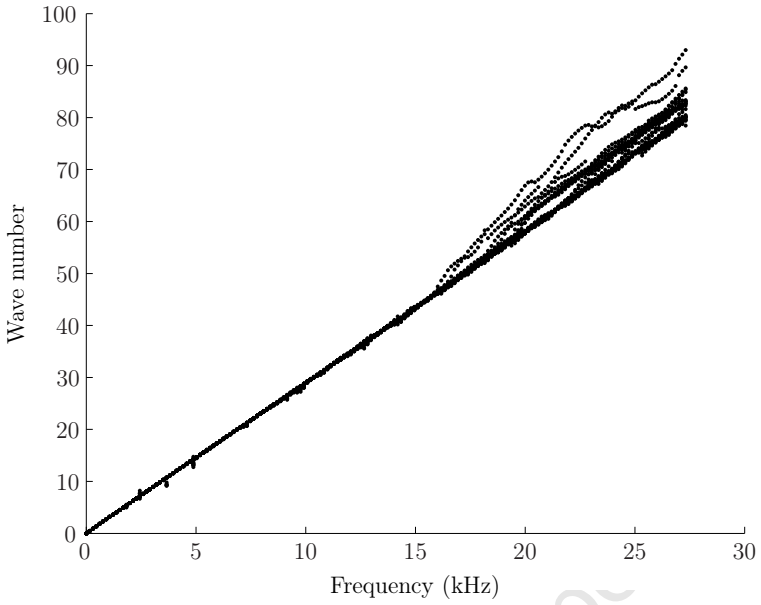

Figure 6.6: A cloud of data showing the spread in Wave number for PMMA.

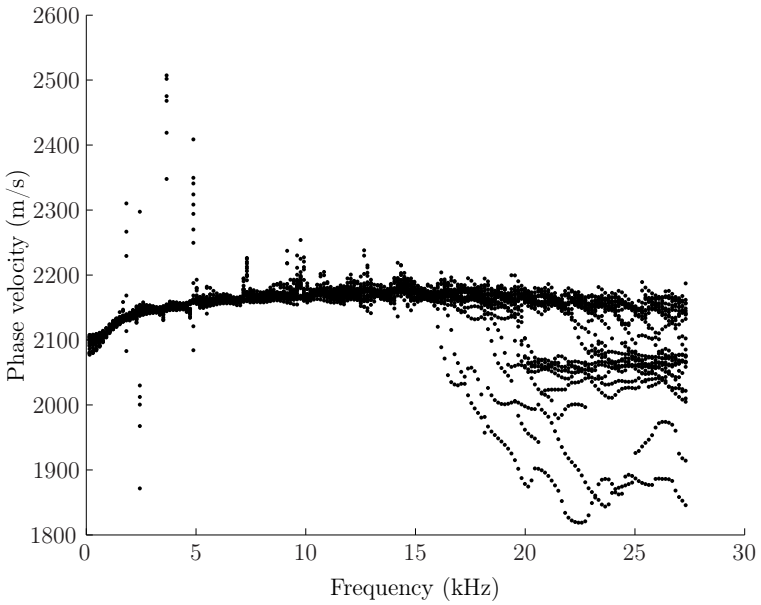

Figure 6.7: A cloud of data showing the spread in Phase velocity for PMMA.

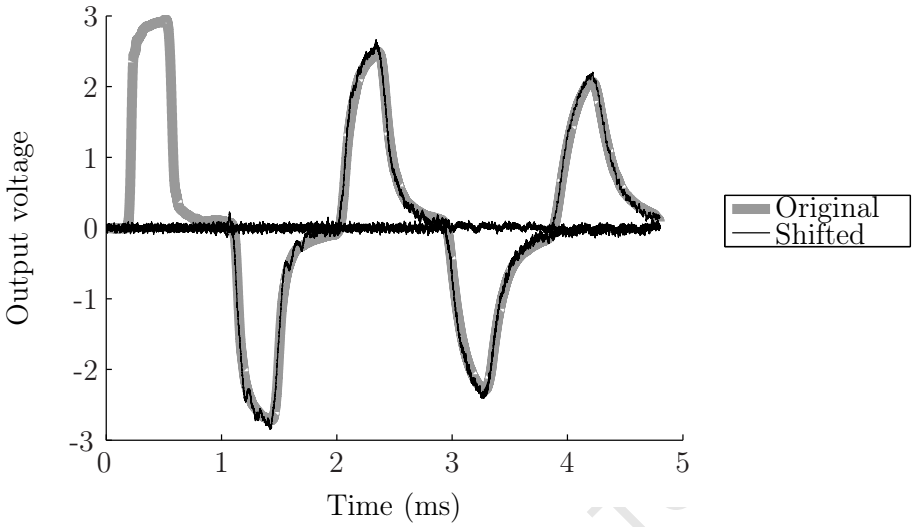

Figure 6.8: The propagation coefficient applied to a PMMA signal and shifted over different distances.

6.1.3 PC single gauge station

In Figure 6.9 the data for the attenuation coefficient for the PC bar is presented. This data is tightly grouped up to 10 kHZ. Between 10 - 15 kHz the data starts to spread and after 20 kHz it scatters and no distinct trend can be seen. In this instance a larger number of data points can be seen below the zero line indicating a negative attenuation coefficient. These data points together with the asymptotes are a result of the numerical error described previously.

In Figure 6.10 the wave number for the PC bar can be seen. In this instance the data is tightly grouped up till 15 kHz where a portion of the test deviate from the trend in a bilinear fashion as observed in the NYLON bar. However the remainder of the data continues in the same linear trend up to 25 kHz where it starts to disperse.

In Figure 6.11 the phase velocity for the PC bar is presented. In a similar fashion to the wave number the phase velocity data forms a trend up to 15 kHz where a group of data starts to deviate leaving the remainder to continue the trend up to almost 25 kHz.

In order to choose a suitable propagation coefficient for the bar, the attenuation coefficient and wave number functions that most closely match the trends seen in Figure 6.9 and 6.10 were used. These were combined according to Equation 5.13 to describe the propagation coefficient. This propagation coefficient is then used on a pulse from the

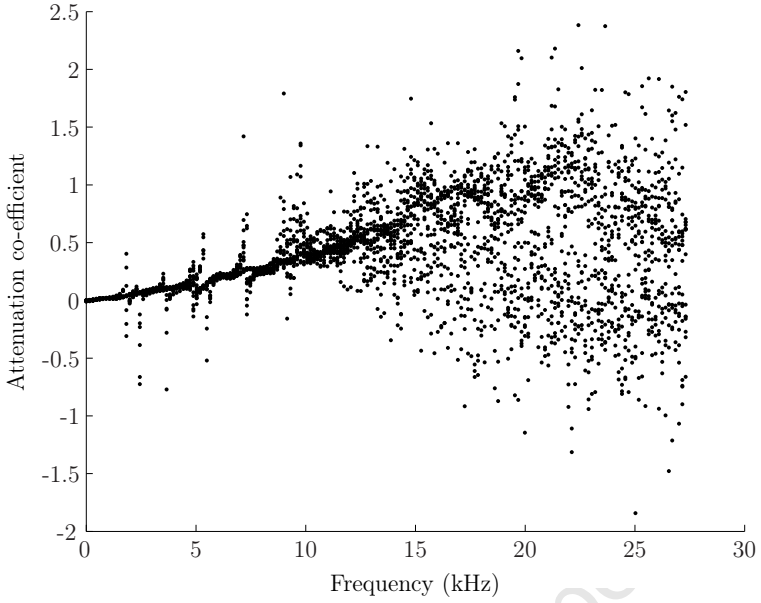

Figure 6.9: A cloud of data showing the spread in Attenuation coefficient for PC single gauge.

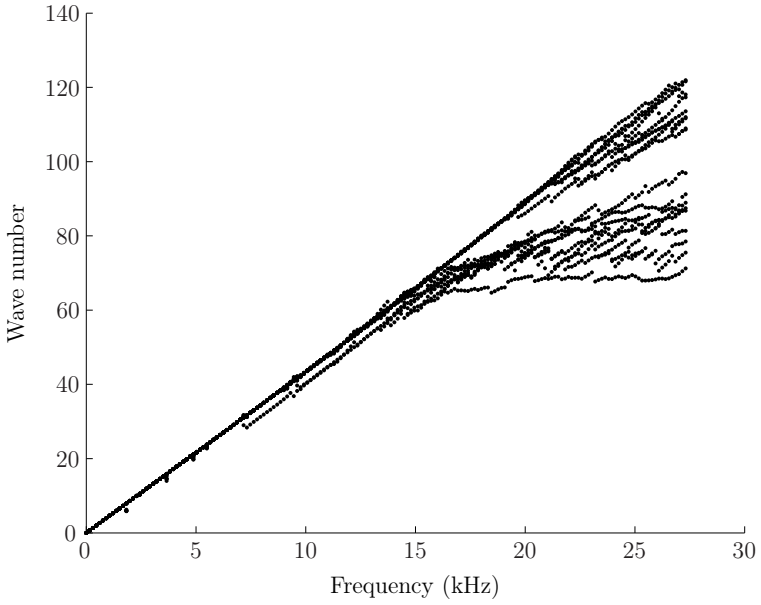

Figure 6.10: A cloud of data showing the spread in Wave number for PC single gauge.

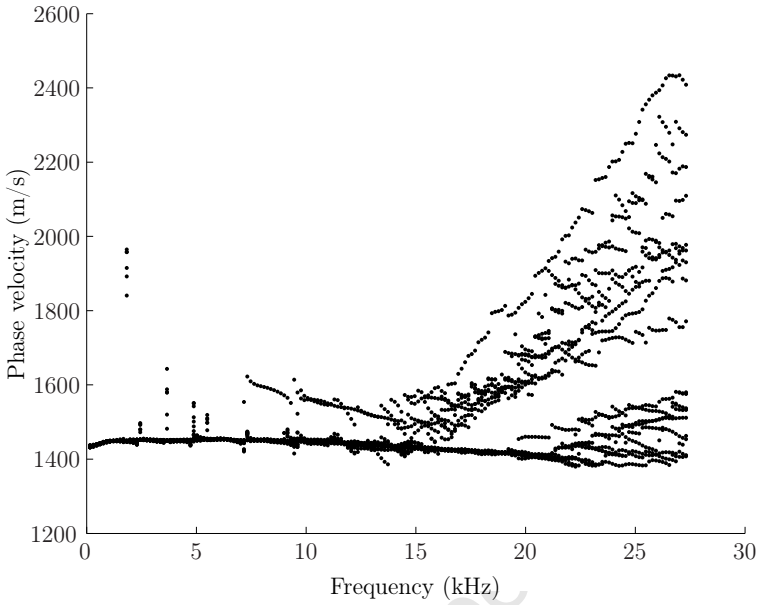

Figure 6.11: A cloud of data showing the spread in Phase velocity for PC single gauge.

PMMA bar that was recorded for an extended duration capturing multiple reflections in the bar. The incident pulse in Figure 6.12 is selected and the propagation coefficient is applied to it as outlined in Section 5.3. The shifting is applied in such a way that the shifted pulses should coincide with the reflected pulses in the bar. The results for the first four reflections in the bar are presented and as can be seen they coincide well with the actual data recorded at the gauge station.

As a final note Pochammer and Chree oscillations were detected on the PC bar. One such example is shown in Figure 6.13 where one of the reflected signals from further down the bar has been shifted back towards the initial pulse on the PC bar with two gauge stations. The Pochammer Chree oscillations can be clearly seen on the plateau of the pulse and the captured data from the two gauge stations can be seen preceding it.

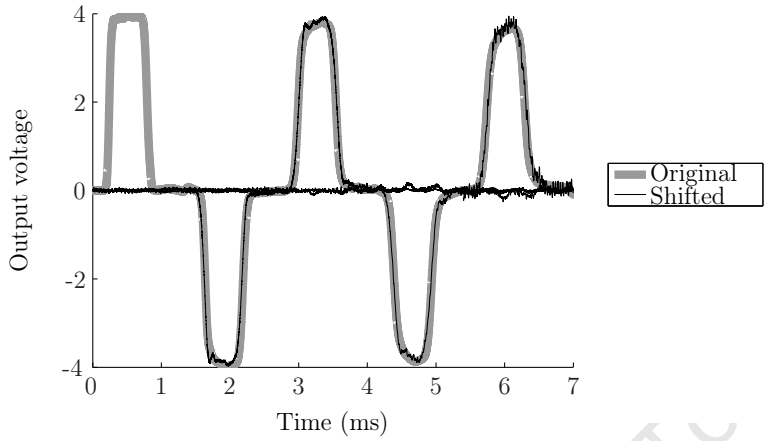

Figure 6.12: The propagation coefficient applied to a PC signal and shifted over different distances.

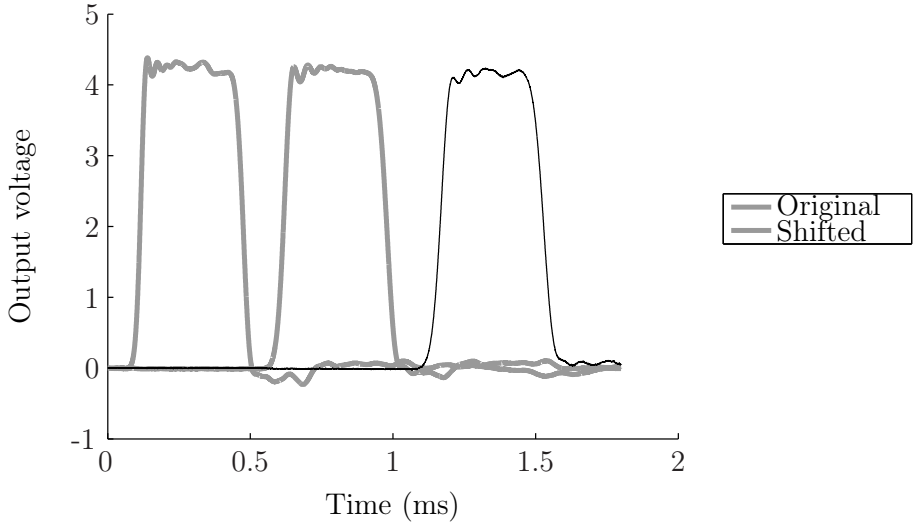

Figure 6.13: The appearance of Pochammer Chree oscillations on the PC bar.

6.1.4 PC double gauge station

The following section presents the results of using a two gauge station method for characterising the bar material of the PC bar. The method is described in Section 5.2 where the decision was made to use a single gauge station for the tests on all the bars. This section is presented here purely as a comparison to the single gauge station method. The key difference between the two methods it that the two gauge method is able to characterise the wave propagation without it reflecting off the free surface. The data used in this section is the same as that for Section 6.1.3, the only difference is that the signals from both gauge stations are used where as previously only the signal from the middle gauge station was used. By doing this a good contrast between the two methods is achieved.

In Figure 6.14 the attenuation coefficient is calculated using the two gauge method. Immediately a difference can be seen to Figure 6.9 where the data started to disperse at 10 kHz. Using the two gauge method the data remains much narrower band right up to 25 kHz. This is significant as the data is from the same tests it means the difference is only due to the difference in measuring techniques. The result is that the data between 10 - 25 kHz was either affected by the reflection off the free surface, small changes in the bar properties as the pulse propagates through a longer distance, or the effect of the incident pulse passing through the single gauge station while the reflected pulse is being measured. It is interesting to note that there are significantly fewer asymptotes in the double gauge station data indicating fewer numerical errors due to division by very small numbers.

In Figure 6.15 the wave number for the two gauge station method can be seen. With the exception of a small amount of data a very strong linear trend can be seen right up to 25 kHz. This is in contrast to the data seen in Figure 6.10 where a portion of the data appeared to deviate from the trend at 15kHz. This means that the data that deviates was clearly affected by the measurement technique.

Finally looking at the phase velocity seen in Figure 6.16 the majority of the data forms an almost linear trend right up to 25 kHz. In the single gauge station tests a portion of the data scatters from what is seen here and this too can be attributed to the different measurement.

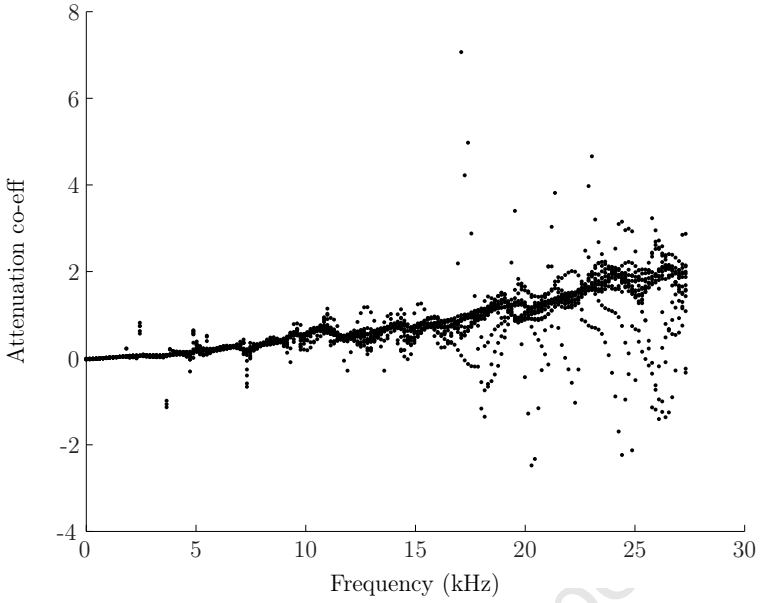

Figure 6.14: A cloud of data showing the spread in Attenuation coefficient for PC double gauge method.

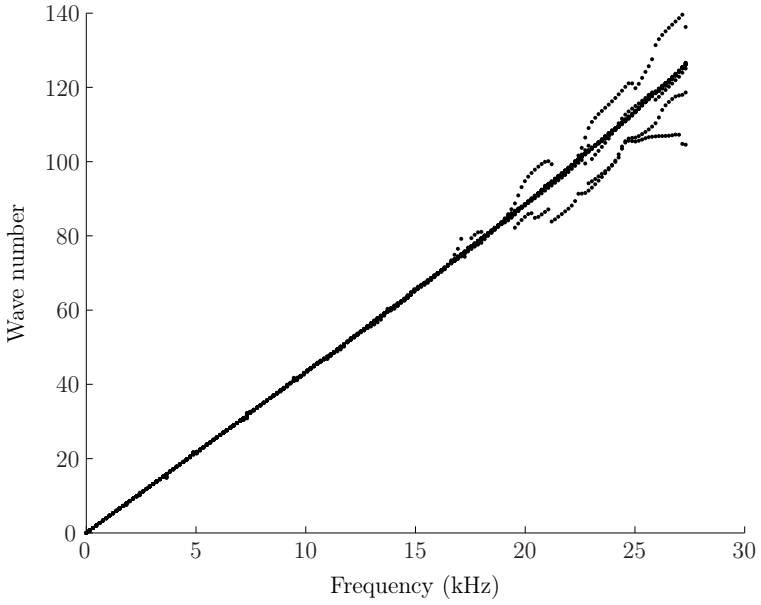

Figure 6.15: A cloud of data showing the spread in Wave number for PC double gauge.

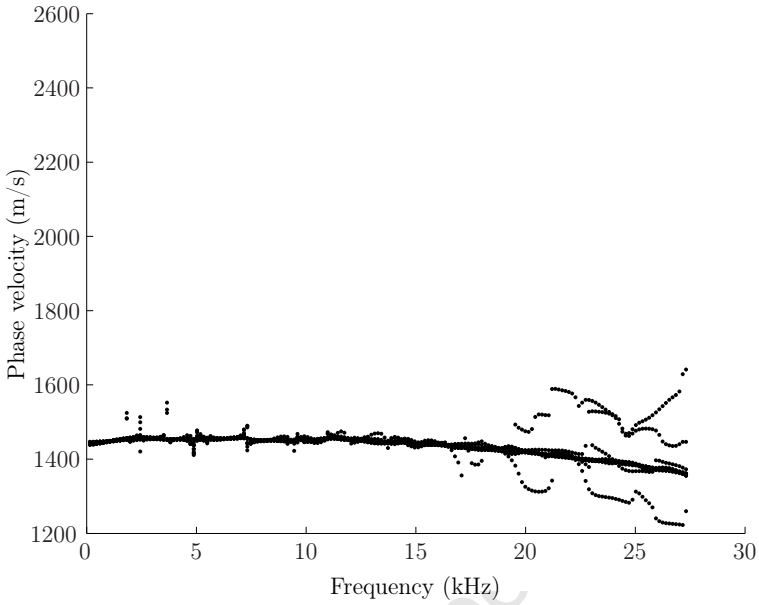

Figure 6.16: A cloud of data showing the spread in Phase velocity for PC double gauge.

6.2 Calibration factors for polymer gauge stations

Measuring the stress is important as Hopkinson bar theory uses the stress to calculate the interface force, displacement and velocity. In Section 4.4.2 the conventional approaches to calibrating the gauge stations is discussed. Due to the material effects of the bars it was only possible to get a valid theoretical calibration factor. Having successfully implemented a technique for correcting for these material effects it is now possible to comment on the calibration of the gauge stations by the other techniques. Using the same methods discussed previously but now using the pulses corrected using the derived propagation coefficient the following calibration factors were achieved:

For the theoretical value in this section the calculated wavespeed and density were used to attain a Young's Modulus which is drastically different to that used previously in Section 4.4.2. It was found that the maximum stress calculation generally gave the most accurate stress value for comparison with the magnesium bar and this was ultimatly the value that was used.

	Theoretical (MPa/V)	Momentum (MPa/V)	Max Stress (MPa/V)
PC	1.72	1.75	1.78
Nylon	2.35	2.18	2.12
PMMA	3.98	3.61	3.54

Table 6.1: The calibration factors for the strain gauges using the corrected waves.

6.3 CONFIGURATION 2 - POLYMER -> MAGNESIUM

In this section the results of placing a magnesium bar at the end of the polymer bar are presented. The previous tests performed have only involved the strain signal from the gauge stations. By using the magnesium bar the conversion from strain to stress in the polymeric bars can be validated against the stress in the magnesium bar. In these tests the polymer bar is impacted with the 150 mm PC striker. The Magnesium bar creates a force boundary condition at the end of the polymer bar. This means that the free reflection no longer takes place. Because the magnesium bars response is well understood it is used to infer the force and stress at the interface between the magnesium bar and the polymer bar. The propagation coefficient from Section 6.1 can then be applied to the signal captured on the polymer bar in a test between the two. The relevant calculations on the incident and reflected pulses in the polymer bars allows for a force at the end of the polymer bar to be inferred. The two forces of the different bars are then compared and can be used as an indication as to the effectiveness of the signal correction in the polymer bar. Figures 6.17, 6.18 and 6.19 show the plots of the force at the two bar ends. The difference between the bar ends was found to fall in the region of 1 - 2.5% for these tests.

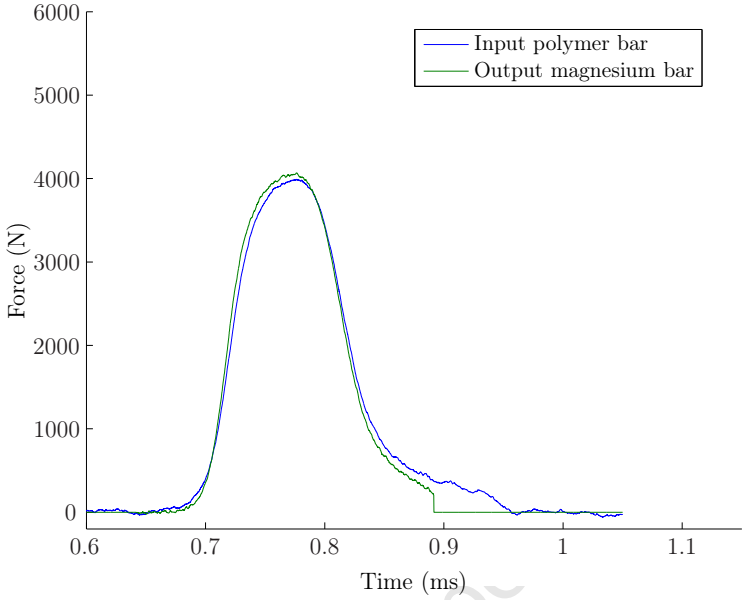

Figure 6.17: The forces at the bar interface between NYLON and magnesium.

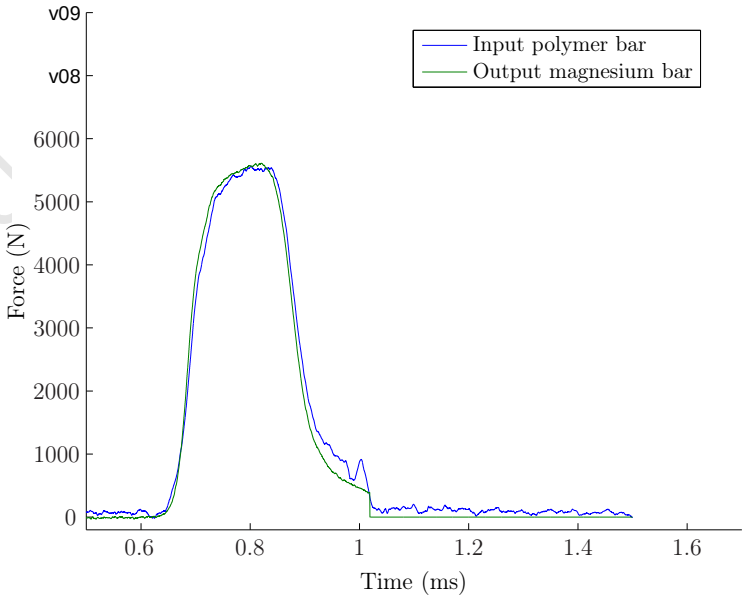

Figure 6.18: The forces at the bar interface between PMMA and magnesium.

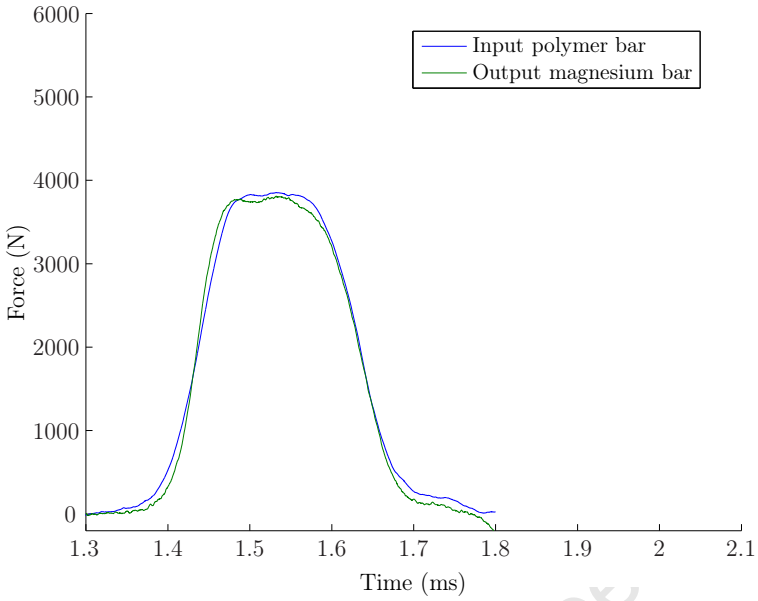

Figure 6.19: The forces at the bar interface between PC and magnesium.

6.4 Configuration 3 - Magnesium ->Polymer

In this section, similar to Section 6.3 the magnesium bar is used to infer the force at the interface of the two bars. In this configuration the magnesium bar is impacted with a 250 mm magnesium striker. The incident and reflected pulses in the magnesium bar are used to infer the force while only the transmitted pulse is used in the polymer bar. As a result of the higher wave speed in the magnesium, the pulses produced in the polymer bar are of a much shorter duration when compared to configuration 2. In this set of tests the difference in the forces at the bar ends was found to be between 1 - 2%.

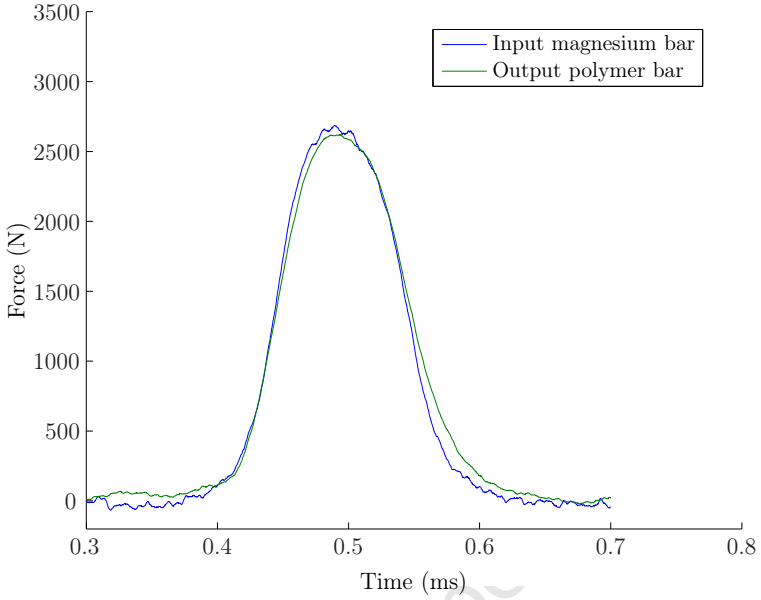

Figure 6.20: The forces at the bar interface between magnesium and NYLON.

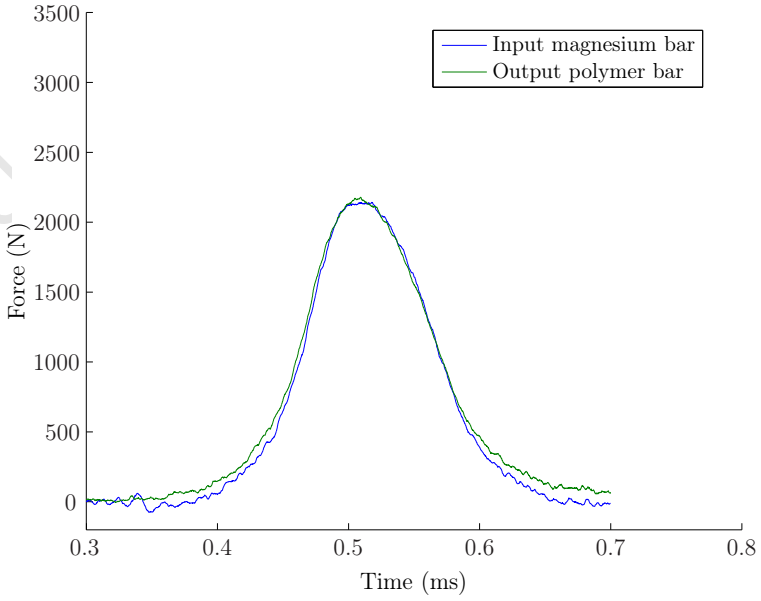

Figure 6.21: The forces at the bar interface between magnesium and PMMA.

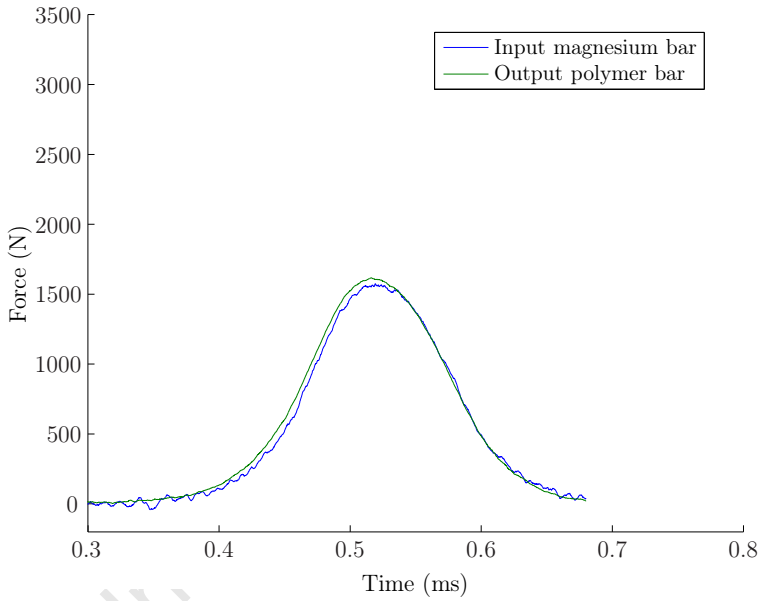

Figure 6.22: The forces at the bar interface between magnesium and PC.

Chapter 7

Discussion

The three different materials investigated in this dissertation (PC, PMMA and NYLON) all appeared in the literature being used in a form of Hopkinson bar testing, whether it be direct impact or Split Hopkinson Bar testing of materials. Many authors do not mention a specific reason for their selection of bar materials in their respective methodology. Hence it is unclear whether any material is better suited to a specific application. In the survey conducted as part of this dissertation, no comparison was found in the literature contrasting the behaviour of these materials, hence the aim of this dissertation.

One of the most pertinent issues being dealt with in this dissertation is the method by which polymeric bar materials are characterised in Hopkinson bar testing. In the literature many authors make use of analytical parameter driven models, often requiring calibration of many different parameters. One such model is the linear solid model which is very similar to Shim's model. In Section 3 the different models are discussed and one such model is implemented in Section 3.3 . While it was possible to come close to replicating the initial behaviour of different materials to an impulsive loading, when the extended response using these parameters was interrogated, the behaviour deviated from the actual material response. This indicates that the simple models are not able to fully describe the response of these polymeric materials and that ultimately the real material behaviour is more complex.

The alternative to these simple models is to use Bacons' method where the the material response is not assumed to take a parameter driven form. Once the code had been developed, this method is implemented as a matter of routine on any material by simply calibrating the propagation coefficient of the material using experimental data

shown in Section 5.2. This is in contrast to the parameter driven models which often involve an iterative process to define model parameters. To the authors knowledge no previous mention of the use of Polycarbonate bars together with Bacons' method could be found in the literature.

Authors in the literature discussing techniques for the characterisation of viscoelastic Hopkinson bars rarely show their method used on more than one bar material. However in this investigation the distinct responses of the three materials tested implies that some applications might be more suitable to certain materials. In Chapter 3 a numerical model is implemented. The shape of the responses achieved with the model most closely resembles that of PMMA. The model is linear viscoelastic, implying that a linear viscoelastic model might be the appropriate choice for PMMA and to a lesser extent NYLON. Characterising this type of response has an impact on the choice of bar material for specific applications. An example of this would be that while the PC bar behaved in an almost elastic fashion, when a pulse was shifted over a long distance it produced more high frequency noise than with the other two materials. As a result the PC bar would work well as an output bar in a SHPB setup where the gauges are typically closer to the interface of interest. On the other hand while the PMMA bar was found to attenuate a significant amount over long distances, this was most reliably predicted using Bacons' method. This would indicate that the PMMA bar would work well as an input bar in a SHPB setup where the pulses end up having to travel through a greater distance.

The Results presented in Chapter 6 show that Bacons' method of viscoelastic material characterisation works well for all three materials. Although different strikers and striker velocities were used no significant difference could be seen in the propagation coefficient produced up to 20 kHz. A distinct trend in the wave number and attenuation coefficient can be seen for each of the materials. This notion is further reinforced when looking at the data captured on the PC bar using the double gauge station. When the wave number and attenuation coefficient of the single and double gauge station are compared, the trend seen in the single gauge station setup is more clearly defined in the double gauge station data. This means that information captured by a single gauge station is still valid but a slightly more accurate characterisation can be achieved using the double gauge station method. The results obtained when the magnesium bar was used together with the polymer bars for force measurement at the bar ends were satisfactory. They validate the use of Bacons' method for predicting the propagation

of waves in polymeric Hopkinson bars works well. If this were not the case then there would be a large force mismatch between the two bars. By using the magnesium bars it is also proved that the conversion from strain to stress is correct

Zhao and Gary present data using their method for 3D material characterisation clearly showing high frequency Pochammer Chree oscillations due to the geometric effects of the bar. One of the main arguments for the implementation of this method was that it was able to capture these geometric effects and reliably reproduce these effects. It was found however, that Bacons' method was just as capable in reproducing the effects of this 3D behaviour. Other authors found this effect to be significant while using large diameter bars where geometric dispersion is significant.

Chapter 8

Conclusions and Recommendations

In this dissertation, a viscoelastic split Hopkinson bar setup which can be used for the testing of materials with low impedance has been implemented. Three different materials (PC, PMMA and NYLON) have been used in the literature as Hopkinson bars and all three were considered here. The different methods for characterising the viscoelastic properties of the bar materials were investigated and Bacons' method was chosen and implemented. The method has been implemented computationally using MATLAB® and validated through force balance tests using magnesium bars together with each of the polymer bars.

The following conclusions can be drawn from this work:

- The polymeric materials used here were not well characterised by a simple linear viscoelastic model.
- Bacons' method for viscoelastic material characterisation was found to be appropriate on PC, PMMA and NYLON Hopkinson bars.
- Bacons' method has been implemented on a PC bar which, to the authors knowledge, has not been presented in the literature. The same method has been successfully implemented on three different bar materials with exactly the same experimental setup which was not found in the literature.
- Both single and double gauge station methods were successfully implemented in characterising the material showing they can be used interchangeably, although a slightly more accurate calibration was achieved using the double gauge station setup.

As a recommendation from this investigation a PC bar will work well as an output bar in a SHPB setup due to the small amount of dispersion and attenuation in the material.

A PMMA bar would however work well as as input bar due to the reliability with which the stress waves can be shifted back to the bar interfaces over longer distances.

This dissertation enables further testing on softer materials such as polymeric foams and biological tissues which can now be conducted using the apparatus and methods implemented.

Bibliography

[1] G. T. Gray(III). *ASM Handbook, Volume 08 - Mechanical Testing and Evaluation*, chapter 43 Classic Split-Hopkinson Pressure Bar testing. ASM International, 2000.

[2] C. Bacon. An experimental method for considering dispersion and attenuation in a viscoelastic hopkinson bars. *Experimental mechanics*, 38(4):242–249, 1998.

[3] S. T. Marais. Development and proving of a split hopkinson pressure bar used for high strain rate materials testing. Master's thesis, Department of Mechanical Engineering, University of Cape Town,, 2001.

[4] Findley W. N. Lai J. S. Onaran K. *Creep And Relaxation Of Nonlinear Viscoelastic Materials*. Dover Publications, 1989.

[5] R. H. Blanc B. Lundburg. Determination of mechanical material properties fromt eh two-point response of an impacted linerarly viscoelastic rod specimen. *Journal of sound and vibration*, 126:97–108, 1988.

[6] H. Zhao G. Gary. A three dimentional analytical solution of the longitudinal wave propagation in an infinite linear viscoelastic cylindrical bar. *Journal of mechanics physics and solids*, 43:1335–1348, 1995.

[7] J. Shim D. Mohr. Using split hopkinson pressure bars to perform large strain compression tests on polyurea at low, intermediate and high strain rates. *International journal of impact engineering*, 36(9):1116–1127, 2009.

[8] S. Rao V. P. W. Shim S. E. Quah. Dynamic mechanical properties of polyurethane using nonmetallic hopkinson bars. *Journal of applied polymer science*, 66:619–631, 1997.

[9] O. Sawas N. S. Brar R. A. brockman. Dynamic characterisation of compliant materials using an all-polymeric split hopkinson bars. *Experimental mechanics*, 38(3):204–210, 1998.

[10] Kyowa technical document - strain gauge bridges, http://www.kyowa-ei.co.jp/english/products/gages/pdf/bridge.pdf. accessed 26/03/2010.

[11] Astm e8 / e8m - 09 standard test methods for tension testing of metallic materials, 2010.

[12] Astm e9 - 09 standard test methods of compression testing of metallic materials at room temperature, 2010.

[13] B. Hopkinson. A method of measuring the pressure produced in the detonation of high explosives or by the impact of bullets. *Philosophical transactions of the royal society A*, 213:437–456, 1914.

[14] R. M. Davies. A critical study of the hopkinson pressure bar. *Philosophical transactions of the royal society A*, 240:375–457, 1948.

[15] R. M. Davies. A simple modification of the hopkinson pressure bar. *Proceedings of the 7th international congress on applied mechanics*, 1:404, 1948.

[16] H. Kolsky. An investigation of the mechanical properties of materials at very high rates of loading,. *Proceedings of the physical society B*, 62:676–700, 1949.

[17] M. F. Spotts. *Mechanical Design Analysis*, chapter 18, pages 345–366. Prentice Hall, 1964.

[18] L. Wang L. Yang. A class of nonlinear viscoelastic constitutive relation of solid polymer materials. *Progress in impact dynamics*, 1:88, 1992.

[19] W. Chen F. Lu B. Zhou. A quartz-crystal-embedded split hopkinson bar for soft materials. *Experimental mechanics*, 40(1):1–6, 2000.

[20] B. Song W. Chen. Dynamic stress equilibration in split hopkinson pressure bar tests on soft materials. *Society for experimental mechanics*, 44(3):300–312, 2004.

[21] Chen W. Lu F. Frew D. J. Forrestal M. J. Dynamic meterial testing of soft materials. *ASME Journal of Applied Mechanics*, 42:65 – 73, 2002.

[22] Song B. Chen W. Split hopkinson pressure bar techniques for characterising soft materials. *Latin American Journal fo Solids and Structures*, 2:113 – 152, 2005.

[23] L. Pochammer. On the propagation velocities of small oscillations in an unlimited isotropic circular cylinder. *J. f. Math. (Crelle)*, 81:324–326, 1876.

[24] C. Chree. The equations of an isotropic elastic solid in polar and cylindrical coordinate, their solutions and applications. *Cambridge Philosophical Society Transactions,*, 14:250–369, 1889.

[25] D. Bancroft. The velocity of longitudinal waves in cylindrical bars. *Physical Review*, 59:588–593, 1941.

[26] R. A. Govender. Numerical investigations of dispersion in hopkinson pressure bars. Master's thesis, University of Cape Town, 2005.

[27] D. A. Gorham. A numerical method for the corection od dispersion in pressure bar signals. *Apparatus and techniques*, 16:477–479, 1983.

[28] Follansbee P. S. Frantz C. Wave propagation in the split hopkinson pressure bar. *Journal of Engineering Materials and Technology*, 105:61–66, 1983.

[29] University of Cape Town N. Morrison. *Introduction To Fourier Analysis*. John Wiley & Sons, 1994.

[30] Frigo Matteo Johnson S. G. The design and implementation of fftw. *Proceedings of the IEEE*, 93(2):216–231, 2005. Special issue on "Program Generation, Optimization, and Platform Adaptation".

[31] http://www.fftw.org/.

[32] Matlab, http://www.mathworks.com/help/techdoc/.

[33] R. H. Blanc. Transient wave propagation methods for determining the viscoelastic properties of solids. *Journal of applied mechanics*, 60:763–768, 1993.

[34] S. R. Brodner H. Kolsky. Stress wave propagation in lead. *Proceedings of hte third U.S. National congress of applied mechanics, ASME*, pages 495–501, 1958.

[35] R. H. Blanc F. P. Champomier. A wave front method for determining the dynamic properties of high damping materials. *Journal of sound and vibration*, 49(1):37–44, 1976.

[36] Lili Wang K. Labibes Z. Azari G. Pluvinage. Generalization of split hopkinson bar technique to use viscoelastic bars. *International journal of impact engineering*, 15-5:669–686, 1994.

[37] H. Zhao G. Gary. On the use of shpb techniques to determine the dynamic behaviour of materials int eh range of small strains. *International journal of solids and structures*, 33:3363–3375, 1995.

[38] G. Gary J. R. Klepaczko H. Zhao. Letter to the editor. *International journal of impact engineering*, 16(3):529–531, 1995.

[39] H. Zhao G. Gary. On the use of a viscoelastic split hopkinson pressure bars. *International journal of impact engineering*, 19:319–330, 1997.

[40] H. Zhao I. Elnasri S. Abdennadher. An experimental study on teh behaviour under impact loading of metallic cellular materials. *International journal of mechanical sciences*, 47:757–774, 2005.

[41] G. A. Coquin. Attenuation of guided waves in isotropic viscoelastic materials. *Journal of the acoustical society of america*, 36:1074–1080, 1964.

[42] C. Salisbury. *Spectral analysis of wave propagation through a polymeric hopkinson bar*. PhD thesis, University of Waterloo, 2001.

[43] S. Ouellet D. Cronin M. Worswick. Compressive response of polymeric foams under quasi-static, medium and high strain rate conditions. *Polymer testing*, 25:731–743, 2006.

[44] Q. Liu G. Subhash. Characterisation of viscoelastic properties of polymer bar using iterative deconvolution in the time domain. *Mechanics of materials*, 38:1105–1117, 2006.

[45] R. Merle H. Zhao. On the errors associated with the use of large diameter shpb correction for radially non-uniform distribution of stress and particle velocity in shpb testing. *International journal of impact engineering*, 32:1964–1980, 2006.

[46] R. Bouix P. Viot J. lataillade. Polypropylene foam behaviour under dynamic loadings: Strain rate, density and microstructure effects. *International journal of impact engineering*, 36:329–342, 2009.

[47] S. Kiernan L. Cui M. D. Gilchrist. Propagation of a stress wave through a virtual functionally graded foam. *International journal of non-linear mechanics*, 44:456–468, 2009.

[48] C.F. Martins M. A. Irfan V. Prakash. Dynamic fracture of linear medium density polyethylene under impact loading conditions. *Materials science and engineering A*, 465:211–222, 2007.

[49] L. M. Yang V. P. W. Shim C. T. Lim. A visco-hyperelastic approach to medelling the constitutive behaviour of rubber. *International journal of impact engineering*, 24:545–560, 2000.

[50] A. S. Yunoshev V. V. Silvestrov. Development of the polymeric split hopkinson bar technique. *Journal of applied mechanics and technical physics*, 42(3):558–564, 2001.

[51] A. Sharma A. Shukla R. A. Prosser. Mechanical characterisation of soft materials using high speed photography and split hopkinson bar technique. *Journal of materials science*, 37:1005–1017, 2002.

[52] I. Kaya. *Very early time characterisation of linear viscoelastic material*. PhD thesis, University of california, Berkly, 1997.

[53] G. Subhash Q. Liu X. Gao. Quasistatic and high strain rate uniaxial compressive response of polymeric structural foams. *International journal of impact engineering*, 32:1113–1126, 2006.

[54] G. Subhash Q. Liu. Quasistatic and dynamic crushability of polymeric foams in rigid confinement. *International journal of impact engineering*, 36:1303–1311, 2009.

[55] Riande E. Diaz-Calleia R. Prolongo M. Salom C. *Polymer Viscoelasticity*. Marcel Dekker Inc., 2000.

[56] Standard test method for compressive properties of ridgid plastics.

[57] Window A. L. Holister G. S. *Strain Gauge Technology.* Applied Science Publishers Ltd., Barking Essex England, 1982.

Appendix A

Strain gauge amp design

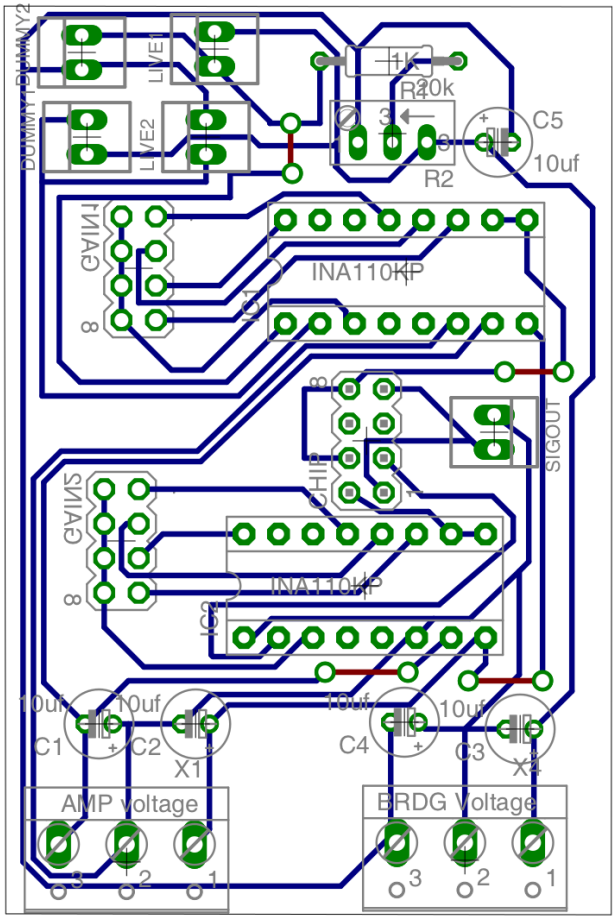

Appendix B

MATLAB code for SHIM model


```
close all
clear all
clc
%%%%%%%%%%%%%%%%%%%%%%%%%%%%%%%%%%%%%%%%

E1 = 2.2e9;
E2 = 200e6;
c1 = 550;
c2 = 800;
d = 20e-3;
L = 2;
rho = 1180;

n = 1001;  % Number of elements in the bar
tSteps = 20000;  % Number of time steps
dT = 5e-7; % Size of time step

load_length = 1000; % length of loading pulse
load_intensity = 800e6; % Magnitude of loading pulse
%%%%%%%%%%%%%%%%%%%%%%%%%%%%%%%%%%%%%%%%



A = d^2*pi/4; % Area of bar
```

```
k1 = E1*A/(L/(n-1)); % Spring 1
k2 = E2*A/(L/(n-1)); % spring 2
m = A*L*rho/(2*n-1); % mass of each node

S = sparse(n);          %create stencil
for ii = 2:n-1
    S(ii,ii) = 2;
    S(ii,ii+1) = -1;
    S(ii+1,ii) = -1;
end

S(1,1) = 1;
S(end,end) = 1;
S(1,2) = -1;
S(2,1) = -1;

M = 2*m*speye(n);    %create mass matrix
M(1,1) = m;
M(end,end) = m;

u = zeros(n,tSteps+2); % create displacment vector

f = zeros(n,tSteps+2); % create force vector
f(1,1:load_length) = load_intensity;


% set the values of different terms
A1 = (1/dT+c2/(k2*dT^2))*M;
A2 = (dT+c2/k2)*f(:,2:end) - (c2/k2)*f(:,1:end-1);
A3 = (2/dT+3*c2/(dT^2*k2))*M-dT*k1*S-(c1+(1+k1/k2)*c2)*S-1/dT*(c1*c2)/k2*S;
A4 = (-1/dT-3*c2/(dT^2*k2))*M + (c1+(1+k1/k2)*c2)*S+2/(dT)*(c1*c2/k2)*S;
A5 = (1/dT^2*c2/k2)*M - 1/dT*(c1*c2/k2)*S;
```

```
%%%% Start loop
for jj = 3:tSteps
    u(:,jj+1) =A1\(A2(:,jj)+A3*u(:,jj)+A4*u(:,jj-1)+A5*u(:,jj-2));
end
%%%% End loop

%% Plot the response of the bar in time
figure
plot(abs(u(round(end/2)+1,:)-u(round(end/2),:)))
title('title')
xlabel('Xlabel')
ylabel('Ylabel')
```

Appendix C

MATLAB code for deriving a propagation co-efficient


```
function input  = ImportData(file_name, Sample_frequency, inputBar, header)

% Created By Richard Curry 2010 as part of MSc reasearch into viscoelastic
% SHPB use


% Read in data capture text file
[ignore, incident1] = textread(strcat('./raw_data/',file_name,'.txt'),'%f %f %*f','heade
'endofline', '\r\n');


Fs = Sample_frequency;                  % Sample frequency from input data
time_inc = (Fs)^-1;                     % Time increment between data points
duration = length(incident1)*time_inc;  % Duration of the captured signal in seconds
pre = 200e-6;                           % Pre trigger in micro sec
pretrig = pre/time_inc - 30;            % Pre trigger in number of data points

%%% Zero the signal
incidentZero1    =  mean( incident1(1:floor(pretrig)) );
input.incident1.raw = (incident1-incidentZero1) ;
```

```
%%% Create a time vector for the origional signal
input.time = (0:time_inc:duration-time_inc)';

%%% Smooth pulse to remove noise using convolution
smoothSpan = 50;
window = ones(smoothSpan,1)/smoothSpan;
input.incident1.smooth = convn(input.incident1.raw,window,'same');


%%% Window the signal into individual pulses
%%%%%%%%%%%%%%%%%%%%%%%%%%%%%%%%%%%%%%%%%%%%%%%%%%%%%%%%%%%%%%%%%%%%%%%%%%%%%%%%
%%% Rough period of the signal in data points used to window the signal for FFT
%period = 11000;   % pc
period = 9400;    % pmma
%period = 10800;   % nylon

%%% Window the signal into discrete waves

tail = 50;                              % tail to use when windowing the signal to
       %  it back to zero without a sharp step

start = 1400;
%% First compressive wave
window1 = test_window(input.incident1.raw, start, start+period, tail);
%% First reflected tensile wave
window2 = test_window((input.incident1.raw), start+period, start+2*period, tail);

%%%%%%%%%%%%%%%%%%%%%%%%%%%%%%%%%%%%%%%%%%%%%%%%%%%%%%%%%%%%%%%%%%%%%%%%%%%%%%%%

% Calculate the Fourier Transforms of the different windows which have been
% defined

NFFT = 2^(nextpow2(length(window1)));           % Number of points to use in the
```

```
%% Create time vector to match NFFT length
input.time2 = (0:time_inc:NFFT*time_inc-time_inc);

trans1 = fft(window1, NFFT);                % FFT of the first window
p1 = unwrap(angle(trans1));                 % Phase angle of the first window

trans2 = -fft(window2, NFFT); % FFT of the second window
p2 = unwrap(angle(trans2)); % Phase angle of the first window


freq(1:(NFFT/2)) = Fs * (0:(NFFT/2-1)) / (NFFT);                    % Frequency vector
frequency domain as a result of the FFT
freq(NFFT/2+1:NFFT) = Fs*(-(NFFT/2):-1)/(NFFT);


%%% Magnitude ratio for the calculation of Attenuation co-eff
trans_diff1 = abs(trans2)./abs(trans1);     % First compressive with first tensile

%%% Difference between phase angles for calculation of dispersion co-eff
angle1 = p2-p1;                             % First compressive with first tensile


%%%%%%%%%%%%%%%%%%%%%%%%%%%%%%%%%%%%%%%%%%%%%%%%%%%%%%%%%%%%%%%%%%%%%%%%%%%%%%%%
%%% SHIFTING METHOD
%%%%%%%%%%%%%%%%%%%%%%%%%%%%%%%%%%%%%%%%%%%%%%%%%%%%%%%%%%%%%%%%%%%%%%%%%%%%%%%%
%%% Method used by Sailsbury

 len = 2;                                   % length over which the signal has propogate
 cut_off = 128;
%% Attenuation co-efficient
 alf = -log((trans_diff1))/(len);             % Attenuation Co-eff
 %alf(cut_off:length(alf)-cut_off) = 0;      % Elimination of high frequency noise
%% Wave number
 k = -angle1/len;                             % Wave number
```

```
 k((NFFT/2 +1 ):NFFT) = -flipud(k(2:NFFT/2+1)); % Flip and mirror the wave number
 c = 2*pi*freq’./k;                             % Phase velocity

%%%% Propagation co-eff
 gamma = alf+ i*k;

%%%% Save the propagation co-efficient
 save([’./calibration/’ file_name], ’alf’, ’k’, ’c’, ’gamma’)

%%%%%%%%%%%%%%%%%%%%%%%%%%%%%%%%%%%%%%%%%%%%%%%%%%%%%%%%%%%%%%%%%%%%%%%%%%%%%%%%%%
%%%%%%%%%%%%%%%%%%%%%%%%%%%%%%%%%%%%%%%%%%%%%%%%%%%%%%%%%%%%%%%%%%%%%%%%%%%%%%%%%%
%%%%%%%%%%%%%%%%%%%%%%%%%%%%%%%%%%%%%%%PLOTTING%%%%%%%%%%%%%%%%%%%%%%%%%%%%%%%%%%%
domain = 400;                   % Variable to define the frequency bandwidth of i
freq = freq/1000;      % Frequency vector for plotting

%break
%%%%%%%%%%%%%%%%%%%%%%%%%%%%%%%%%%%%%%%%%%%%%%%%%%%%%%%%%%%%%%%%%%%%%%%%%%%%%%%%%%
%%% Figure showing origional waves and the selected windows
figure(counter)
axes_handle = gca;
hold all
%grid on
plot(input.time(1:40000)*1000, (input.incident1.smooth(1:40000)), ’k--’)
plot(input.time(1:40000)*1000, (window1))
plot(input.time(1:40000)*1000, (-window2))

title (’Raw voltage from strain gauges for PMMA bar single station’)
xlabel (’Time (ms)’)
ylabel (’Voltage (V)’)
legend(’Raw signal’, ’Window 1’, ’Window 2’, ’location’, ’SE’)

%%%%%%%%%%%%%%%%% Save the figures in different formats
%set(gcf, ’PaperUnits’, ’inches’);
%set(gcf, ’PaperSize’, [8 10]);
```

```
set(gcf, 'PaperPosition', [0 0 8 6])

filename = ['./calibration/' file_name];
    handle = ['-f' num2str(counter)];
    laprint(counter, filename, 'options', 'laprint.mat')
    %print(handle, '-r800', '-dpdf', filename)
    print(handle, '-r800', '-dpng', filename)
    %print(handle,'-r1800', '-depsc', filename)

%%%%%%%%%%%%%%%%%%%%%%%%%%%%%%%%%%%%%%%%%%%%%%%%%%%%%%%%%%%%%%%%%%%%%%%%%%%%%%%%%%%%%%%%

%%% Figure to show the difference in absolute magnitudes between different
%%% signals
figure(2)
hold all
plot(freq(1:120), abs(trans1(1:120)))
plot(freq(1:120), abs(trans2(1:120)))
title('Modulus of pC pulses in the frequency domain')
xlabel('Frequency (KHz)')
ylabel('Magnitude')
set(legend('First Compressive pulse', 'First tensile reflection', 'location', 'NE'),'Fon

%%%%%%%%%%%%%%%%%%%%%%%%%%%%%%%%%%%%%%%%%%%%%%%%%%%%%%%%%%%%%%%%%%%%%%%%%%%%%%%%%%%%%%%%

figure(3)
plot(freq(1:120), c(1:120))
title('Phase velocity for PMMA bar')
xlabel('Frequency (KHz)')
ylabel('Phase velocity m/s')

%%%%%%%%%%%%%%%%%%%%%%%%%%%%%%%%%%%%%%%%%%%%%%%%%%%%%%%%%%%%%%%%%%%%%%%%%%%%%%%%%%%%%%%%
%%% Figure to show the unwrapped phase angle

figure(4)
```

```
hold all
plot(freq(1:120), unwrap(angle(trans1(1:120))))
plot(freq(1:120), unwrap(angle(trans2(1:120))))
title('Unwrapped Phase angle of PMMA pulses in the frequency domain')
xlabel('Frequency (KHz)')
ylabel('Unwrapped Phase angle (rad)')
set(legend('First Compressive pulse', 'First tensile reflection', 'location', 'SW

%%%%%%%%%%%%%%%%%%%%%%%%%%%%%%%%%%%%%%%%%%%%%%%%%%%%%%%%%%%%%%%%%%%%%%%%%%%%%%%%
%%% Figure to show the attenuation co-efficient

figure(5)
plot(freq(1:150),alf(1:150))
title('Attenuation Co-efficient for PMMA bar')
xlabel('Frequency (KHz)')
ylabel('Magnitude')

%%%%%%%%%%%%%%%%%%%%%%%%%%%%%%%%%%%%%%%%%%%%%%%%%%%%%%%%%%%%%%%%%%%%%%%%%%%%%%%%
%%% Figure to show the wave number

figure(6)
hold all
plot(freq(1:120),k(1:120))
title('Wave number for PMMA bar')
xlabel('Frequency (KHz)')
ylabel('Magnitude')

%%%%%%%%%%%%%%%%%%%%%%%%%%%%%%%%%%%%%%%%%%%%%%%%%%%%%%%%%%%%%%%%%%%%%%%%%%%%%%%%

 %%% Saving the figures as PDF
%%%%%%%%%%%%%%%%%%%%%%%%%%%%%%%%%%%%%%%%%%%%%%%%%%%%%%%%%%%%%%%%%%%%%%%%%%%%%%%%

    %
%     filename = ['MARP compressive wave_mag'];
```

```
%     handle = ['-f2'];
%     print(handle, '-r800', '-dpdf', filename)
% %
%     filename = ['MARP compressive wave_mag_diff'];
%     handle = ['-f3'];
%     print(handle, '-r800', '-dpdf', filename)
%
%     filename = ['PC bar predited compressive wave_angle'];
%     handle = ['-f4'];
%     print(handle, '-r800', '-dpdf', filename)
%
%     filename = ['PC bar predited compressive wave_zoomed'];
%     handle = ['-f6'];
%     print(handle, '-r800', '-dpdf', filename)


function cut = test_window(origional, start_window, end_window, tail)

%%%%%%%%%%%%%%%%%%%%%%%%%%%%%%%%%%%%%%%%%%%%%%%%%%%%%%%%%%%%%%%%%%%%%%%%%%%%%%%%%%%%%%%
%% Function for windowing a pulse

len = int32(length(origional));

raw_cut =zeros(len, 1);

raw_cut(start_window:end_window) = 1;

temp1 = linspace(-pi/2,pi/2,tail);
temp2 = linspace(pi/2,3*pi/2 ,tail);

raw_cut(start_window:start_window+(tail-1)) = (sin(temp1)+1)/2;
raw_cut(end_window-(tail-1):end_window) = (sin(temp2)+1)/2;

cut = origional.*raw_cut;
```

Appendix D

MATLAB code for shifting signals


```
clear all
close all
clc

%-------------------------------------------------------------------------
% USER INPUTS
path = './PC/Double/raw_data/'; % Path where the file resides
file_name = 'richard_double_pc_2'; % File name
header = 13; % Number of lines in the header

input.rate = 5e6; % Sample frequency
input.increment = 1/input.rate;
input.pre_trig = 200e-6; % Pretrigger interval


% Time between samples
time_inc = input.increment;


%-------------------------------------------------------------------------
% Import the data file obtained from strain gauges

[incident] = textread(strcat(path,file_name,'.txt'),'%f %*f','headerlines'
```

```
,header, 'endofline', '\r\n');

% Calculate the zero offset for the data
incidentZero    =  mean( incident(1:50) );
% Calulate the duration of the data file
input.duration = length(incident)*time_inc;
% Create a time vector for the input file
input.time = (0:time_inc:input.duration-time_inc)';
% Zero the data
input.incident.raw = (incident-incidentZero) ;

% Smooth pulse to remove noise using convolution
smoothSpan = 100;
window = ones(smoothSpan,1)/smoothSpan;
input.incident.smooth = convn(input.incident.raw, window,'same');
input.incident2.smooth = convn(input.incident2.raw, window,'same');
%--------------------------------------------------------------------------
% CALCULATIONS

% Approximate number of data points to capture the pulse
window1 = 4000;

% Load the calibration file containing the different maps for the polymer bar

 load('./PC/Double/calibration/richard_double_pc_1.mat');
Set the transfer function as the propagation coefficient
 transfer = gamma;

% Shift the signal by inputting the windowed pulse, the transfer function and the
Shifted_signal = ShiftPolymer(input.incident2.smooth(1:5500), transfer , 0.8);

%%%%%%%%%%%%%%%%%%%%%%%%%%%%%%%%%%%%%%%%%%%%%%%%%%%%%%%%%%%%%%%%%%%%%%%%%%%%%%%
%%%%%%%%%%%%%%%%%%%%%%%%%%%%%%%%%%%%%%%%%%%%%%%%%%%%%%%%%%%%%%%%%%%%%%%%%%%%%%%
ShiftPolymer function file
```

```
%%%%%%%%%%%%%%%%%%%%%%%%%%%%%%%%%%%%%%%%%%%%%%%%%%%%%%%%%%%%%%%%%%%%%%%%%%%%
% This function file takes in the original signal, the transfer function and the distanc

function shifted = ShiftPolymer(raw_signal, transfer, distance)


% Number of points to use in the DFT
NFFT = length(transfer);
% Use the FFT to transfer the signal to the frequency domain
trans1 = fft(raw_signal, NFFT);                 % FFT of the window

% Shift the signal in the frequency domain
shift = (trans1) .* exp((-transfer).*distance);    % Apply the prop co-eff to a signal.

% Use the IFFT to bring the shifted signal back to the time domain
shifted =real(ifft( shift, NFFT));     % Back to time domain
```